

January 01, 2010

## Dark matter and collider phenomenology of non-universal gaugino masses

Michael Holmes  
*Northeastern University*

---

### Recommended Citation

Holmes, Michael, "Dark matter and collider phenomenology of non-universal gaugino masses" (2010). *Physics Dissertations*. Paper 17.  
<http://hdl.handle.net/2047/d20000139>

This work is available open access, hosted by Northeastern University.

# Dark Matter and Collider Phenomenology of Non-Universal Gaugino Masses

A dissertation presented

by

Michael Holmes

to

The Department of Physics

In partial fulfillment of the requirements for the degree of  
Doctor of Philosophy

in the field of

Physics

Northeastern University  
Boston, Massachusetts  
April, 2010

©Michael Holmes, 2010  
ALL RIGHTS RESERVED

# Dark Matter and Collider Phenomenology of Non-Universal Gaugino Masses

by

Michael Holmes

## ABSTRACT OF DISSERTATION

Submitted in partial fulfillment of the requirement  
for the degree of Doctor of Philosophy in Physics  
in the Graduate School of Arts and Sciences of  
Northeastern University, April, 2010

# Abstract

Signals of minimal supersymmetric models with non-universalities in the gaugino sector of the theory are analyzed at the CERN Large Hadron Collider (LHC) and in experiments searching for dark matter. Signals of dark matter including direct and indirect detection are investigated at depth in various supersymmetric frameworks. The parameter space of deflected mirage mediation, in which the soft terms receive contributions from the three main supersymmetry breaking mediation mechanisms, is investigated with emphasis on the neutralino sector and dark matter signals. The potential for non-universal gaugino masses to explain the recent CDMS II data is studied and possible implications for indirect dark matter detection experiments and LHC signatures are considered. Collider implications of non-universalities in the gaugino sector are examined with attention paid to specific signatures which are targeted to track the non-universalities. Further, the complementarity of dark matter and collider measurements is discussed with emphasis on breaking model degeneracies which may arise in LHC data.

# Acknowledgements

The work presented here was carried out with my Advisor, Professor Brent Nelson (Northeastern University), and with collaborators Dr. Ismet Altunkaynak (Northeastern University), Professor Gordon Kane (University of Michigan) and Dr. Phillip Grajek (University of Michigan and currently at KEK).

- I would like to thank my Thesis Committee: Professors Brent Nelson, Pran Nath and Emanuela Barberis for all the help and guidance over the years.
- I would also like to thank the Northeastern University Physics department and its members for support and help during my graduate career and in particular Professors Haim Goldberg and George Alverson.
- I offer many thanks to my colleague Dr. Ismet Altunkaynak for all the help and useful discussions over the years.
- I offer the sincerest thanks and appreciation to Professor Brent Nelson. I have been privileged to have you as my Advisor over the years and I truly appreciate all your guidance and support during my time at Northeastern.
- Finally, I would like to thank my family.

# Contents

<b>Abstract</b>	<b>4</b>
<b>Acknowledgements</b>	<b>5</b>
<b>1 Introduction and Overview</b>	<b>9</b>
<b>2 The MSSM</b>	<b>13</b>
2.1 The MSSM framework . . . . .	13
2.1.1 Particle content . . . . .	14
2.1.2 Review of global and local SUSY . . . . .	16
2.1.3 $W_{\text{MSSM}}$ and $\mathcal{L}_{\text{soft}}^{\text{MSSM}}$ . . . . .	19
2.2 High scale models . . . . .	22
2.3 Higgs potential and EWSB . . . . .	23
2.4 Superpartner masses . . . . .	25
2.5 Gaugino sector . . . . .	29
2.6 Signals of SUSY . . . . .	31
2.6.1 Dark matter . . . . .	31
2.6.2 Colliders . . . . .	32
<b>3 Dark matter and the LSP</b>	<b>33</b>
3.1 Relic density . . . . .	34
3.2 Direct detection . . . . .	36
3.3 Indirect detection . . . . .	40
<b>4 Dark matter signals in deflected mirage mediation</b>	<b>45</b>
4.1 DMM parameter space . . . . .	45

4.2	Survey of DM signatures . . . . .	55
4.2.1	Relic density . . . . .	55
4.2.2	Direct detection . . . . .	58
4.2.3	Gamma rays . . . . .	61
4.2.4	Muons . . . . .	65
4.2.5	Anti-Matter from cosmic rays . . . . .	66
4.2.6	Benchmarks . . . . .	68
4.3	Summary . . . . .	71
<b>5</b>	<b>Dark matter signals of non-universal gaugino masses?</b>	<b>72</b>
5.1	Benchmark models for CDMS II signal . . . . .	73
5.2	Other DM signals . . . . .	78
5.3	LHC signatures . . . . .	82
5.4	Summary . . . . .	84
<b>6</b>	<b>LHC phenomenology of non-universal gaugino masses</b>	<b>86</b>
6.1	Background . . . . .	87
6.2	Benchmarks . . . . .	89
6.3	Signature lists and distinguishing models . . . . .	90
6.4	Benchmark model LHC analysis . . . . .	93
6.5	Summary . . . . .	101
<b>7</b>	<b>Lifting model degeneracies in LHC data using dark matter observations</b>	<b>102</b>
7.1	LHC inverse problem . . . . .	102
7.2	Classifying degenerate pairs . . . . .	105
7.3	Direct detection . . . . .	108
7.4	Gamma rays . . . . .	117
7.5	Summary . . . . .	123

<b>8</b>	<b>Conclusions</b>	<b>127</b>
<b>9</b>	<b>Appendix</b>	<b>130</b>
	<b>Bibliography</b>	<b>133</b>

# Chapter 1

## Introduction and Overview

At the time of this writing the high energy community is entering a very exciting era. Up until now the Standard Model (SM) has been our best understanding of Nature which has been rigorously backed up by experimental observations. The SM is not complete however as it does not include neutrino masses (for example) and hence there must be some Beyond-the-Standard Model (BSM) physics. With data taking at the Large Hadron Collider (LHC) on the brink of occurring soon there may be new exciting evidence for BSM physics [1]. There are an array of possibilities for what the BSM physics may be and many are motivated from a high scale theory. Among the possible theories of BSM physics supersymmetry (SUSY) is highly-motivated for reasons such as gauge coupling unification and the existence of a solution to the hierarchy problem. Another intriguing property of SUSY is that the minimal extension of the SM includes a possible explanation for the dark matter (DM) problem, which was discovered after the model was proposed.

The general SUSY framework is described in terms of the Minimal Supersymmetric Standard Model (MSSM) and the parameter space is large, of dimension 124. Many possible experimental outcomes may result within the MSSM framework, and in particular the gaugino sector of the theory is very compelling as it is relevant for the DM properties as well as signatures which may arise at the LHC. By signatures we refer to distinct final state topologies which arise from decays of supersymmetric particles such as trilepton final states, for example. The gaugino sector of SUSY also offers clues as to the nature of SUSY breaking which is very important to understand. It gives insight to the type of string-inspired model or Grand Unified Theory (GUT) which may govern the nature of the SUSY breaking. The

gaugino sector of the MSSM is intimately related to the dark matter particle within the MSSM, as well as to understanding the nature of SUSY breaking in general, it is therefore very interesting. In this thesis the work focuses on non-universal gaugino masses (NUGM), which result in a rich low scale gaugino sector of the MSSM and therefore of possible dark matter observables along with corresponding LHC signatures which soon may be discovered.

From a high scale perspective SUSY is the low scale effective theory of string theory. There are many possible string theories which currently exist and if SUSY is discovered it may offer support in the direction of string theory. String theories generally suffer from a stabilization problem associated with the scalar fields in the theory resulting in unstable vacua. Recent work suggests methods for stabilizing the vacuum in a string theory require the existence of multiple sources of SUSY breaking to contribute to the soft SUSY terms which results in non-universal gaugino masses. One such scenario has recently been introduced called deflected mirage mediation (DMM) in which gravity, anomaly and gauge mediated SUSY breaking mechanisms may be simultaneously present. An analysis is given here on the prospects of neutralino dark matter within the DMM model framework and what possible observations are possible. It is shown that there exist regions of the parameter space where all three mediation mechanisms are present and give a thermal relic abundance of neutralinos in line with the Wilkinson Microwave Anisotropy Probe (WMAP). Direct detection, and indirect detection including gamma ray, muon and anti-matter experiments are considered, and the investigated parameter space is shown to be in line with current experimental bounds. Discovery prospects are discussed for relevant upcoming experiments.

Recently a possible signal of dark matter may have been observed by the CDMS II direct detection experimental group. An explanation for the observed dark matter scattering events can be explained quite readily within the context of Minimal Supergravity (mSUGRA) with non-universal gaugino masses. An analysis is given which can explain the possible dark matter signal using the mSUGRA + NUGM. Furthermore various other dark matter signals are given along with a basic survey of LHC signatures expected for such models.

There exists a string motivated framework, called mirage mediation, in which the gaugino masses can be parametrized by a single non-universality parameter. This scenario is a simplified version of the DMM model in which no gauge mediation contributes. This offers a convenient way to study the effects of such non-universal gaugino masses, specifically the resulting LHC signatures. Two possible string scenarios are parametrized in such a way and the resulting LHC properties are given. The integrated luminosity necessary to differentiate the values of the non-universality parameter are given for the models along with further analysis of LHC signatures and model properties.

An important issue is also the so-called LHC inverse problem. This arises when more than one set of model parameters can fit the LHC data, thus resulting in degenerate theory models which describe the data. A analysis is given by which degenerate SUSY models at the LHC are used to investigate the utility of dark matter observables to untangle the model degeneracies. The degenerate pairs can have gaugino sectors which involve non-universalities and hence interesting dark matter signals. Specifically direct detection and indirect gamma ray detection experiments are investigated and it is shown that they can be quite helpful at resolving the inverse problem. Theoretical and experimental errors are taken into account. The analysis is compared to a study which used the same points to investigate whether the proposed International Linear Collider can help alleviate the degeneracies.

The organization of this thesis is as follows: in Chapter 2 the basics of SUSY and the MSSM are briefly reviewed. Chapter 3 discusses the role of the lightest supersymmetric particle (LSP) in dark matter observables relevant for various experiments. Chapter 4 introduces the Deflected Mirage Mediation (DMM) scenario and gives an overview of the possible dark matter signals within the DMM framework. Chapter 5 discusses the relevance of NUGM to the recent possible signal of direct detection of dark matter at CDMS II along with a look at some resulting LHC signatures. Chapter 6 analyzes a few string motivated benchmarks at the LHC with varying gaugino masses via a single parameter and discusses important signatures which shed light on the non-universality parameter. In Chapter 7 the

utility of using dark matter observations to lift possible MSSM model degeneracies at the LHC is discussed.

# Chapter 2

## The MSSM

### 2.1 The MSSM framework

The Standard Model (SM) [2, 3, 4],[5, 6, 7],[8, 9, 10, 11, 12] is a well established effective theory of particle physics, but many drawbacks are inherent. Among these one might include the lack of an understanding for neutrino masses, the absence of a cold dark matter candidate, and no comprehensive explanation of electroweak symmetry breaking. Furthermore the Higgs mass in the Standard Model is quadratically divergent at the quantum level. It is quite clear that these problems need to be addressed and just how to do that brings us to the subject of supersymmetry.

Supersymmetry [13] can resolve the problems with the Standard Model just discussed. The Higgs mass no longer suffers from quadratic divergences as new fields enter the theory which solve this problem. In the minimal supersymmetric Standard Model electroweak symmetry breaking is triggered by renormalization group effects which drive the Higgs mass-squared to negative values. A dark matter candidate is present in the MSSM if one assumes  $R$ -parity is conserved. Neutrino masses can be included in the theory and actually fit quite nicely when one embeds the model in a grand unified group such as  $SO(10)$ . The three gauge couplings unify in the MSSM at a high scale of  $Q_{\text{GUT}} \simeq 2 \times 10^{16}$  GeV which is a strong hint in favor of such a grand unified theory. From a high scale perspective such as string-theory, supersymmetry is a necessary ingredient. These and many other reasons offer a strong hint that SUSY may turn out to be the theory which describes physics beyond the Standard Model.

Many excellent reviews and books exist for the minimal supersymmetric standard model (MSSM). A partial list of resources for general SUSY and the MSSM can be found in [14, 15, 16, 17, 18, 19, 20, 21]. The review of the MSSM given here is by no means complete, but rather serves a simple reminder of the important properties of the model relevant to the later analyses.

### 2.1.1 Particle content

Supersymmetry is an extension of the Poincarè group and is a space-time symmetry which relates bosons and fermions. The action of the supersymmetry generator  $Q$  transforms bosons into fermions and fermions into bosons via

$$Q|\text{boson}\rangle = |\text{fermion}\rangle, \quad Q|\text{fermion}\rangle = |\text{boson}\rangle. \quad (2.1)$$

The global supersymmetry algebra is built using anti-commuting fermionic generators  $Q$  and  $Q^\dagger$  (here written in 2-component Weyl notation) which satisfy the following commutation and anti-commutation relations:

$$\{Q, Q^\dagger\} = 2\sigma_\mu p^\mu, \quad \{Q, Q\} = \{Q^\dagger, Q^\dagger\} = [Q, p^\mu] = [Q^\dagger, p^\mu] = 0, \quad (2.2)$$

where  $p^\mu$  is the four momentum generator of space-time translations and  $\sigma_\mu = (\mathbf{1}_{2\times 2}, \vec{\sigma})$  with  $\vec{\sigma}$  the Pauli matrices.

Supermultiplets are the irreducible representations of the single particle states containing both the fermionic and bosonic superpartners. Particles in the same supermultiplet have the same mass and same gauge charges. Furthermore the particles in a supermultiplet have the same number of bosonic and fermionic degrees of freedom.

The supersymmetric extension of the Standard Model requires an additional particle for each SM particle but with spin differing by  $\hbar/2$ . The SM fermions have scalar superpartners called sfermions and the SM gauge fields have fermionic superpartners called gauginos. The

supermultiplet	boson	fermion	$SU(3)_C$	$SU(2)_L$	$U(1)_Y$
$\hat{Q}$	$(\tilde{u}_L, \tilde{d}_L)$	$(u_L, d_L)$	<b>3</b>	<b>2</b>	$\frac{1}{6}$
$\hat{u}$	$\tilde{u}_R^*$	$u_R^\dagger$	$\bar{\mathbf{3}}$	<b>1</b>	$-\frac{2}{3}$
$\hat{d}$	$\tilde{d}_R^*$	$d_R^\dagger$	$\bar{\mathbf{3}}$	<b>1</b>	$\frac{1}{3}$
$\hat{L}$	$(\tilde{\nu}, \tilde{e}_L)$	$(\nu, e_L)$	<b>1</b>	<b>2</b>	$-\frac{1}{2}$
$\hat{e}$	$\tilde{e}_R^*$	$e_R^\dagger$	<b>1</b>	<b>1</b>	<b>1</b>
$\hat{H}_u$	$(H_u^+, H_u^0)$	$(\tilde{H}_u^+, \tilde{H}_u^0)$	<b>1</b>	<b>2</b>	$\frac{1}{2}$
$\hat{H}_d$	$(H_d^0, H_d^-)$	$(\tilde{H}_d^0, \tilde{H}_d^-)$	<b>1</b>	<b>2</b>	$-\frac{1}{2}$
$\hat{g}$	$g_\mu^a$	$\tilde{g}^a$	<b>8</b>	<b>1</b>	<b>0</b>
$\hat{W}$	$W_\mu^\pm, W_\mu^3$	$\tilde{W}^\pm, \tilde{W}^3$	<b>1</b>	<b>3</b>	<b>0</b>
$\hat{B}$	$B_\mu$	$\tilde{B}$	<b>1</b>	<b>1</b>	<b>0</b>

Table 2.1: **MSSM particle content.** Chiral and gauge supermultiplets of the MSSM along with the gauge charges. Supermultiplets are denoted with a hat and the EM charge is  $Q_{\text{EM}} = T_3 + Y$ .

SM fields and superpartner fields reside in either a chiral or gauge supermultiplet and since the superpartners have the same gauge charges they couple to other fields as the SM fields do. The minimal case of the SUSY extension to the SM (MSSM) also needs to contain two Higgs isospin doublets rather than the single Higgs doublet in the SM. That this is necessary stems from the necessity of the theory to remain anomaly free and two Higgs are also needed to give masses to up and down type fermion fields. So the MSSM is made of the usual SM quarks and leptons along with their superpartner squarks and sleptons, the SM gauge fields and the superpartner gauginos and also two Higgs scalar doublets and their fermionic Higgsino superpartners. The minimal field content of the MSSM is given in Table 2.1 where the supermultiplets are denoted with a hat, e.g.  $\hat{Q}$  contains the left handed quark and squark fields. The convention of the electric charge is  $Q_{\text{EM}} = T_3 + Y$  with  $T_3$  the weak isospin generator and  $Y$  the hypercharge.

As briefly mentioned the fields within a supermultiplet have the same mass. This is only true if SUSY is unbroken, and since no superpartners have been discovered as of yet it means that supersymmetry is broken and just how it is broken remains a mystery. A consequence of SUSY being broken means that the Lagrangian for the MSSM can be written in terms of

the SUSY invariant piece plus a piece which parametrizes the breaking of SUSY, or

$$\mathcal{L} = \mathcal{L}_{\text{SUSY}} + \mathcal{L}_{\text{soft}}. \quad (2.3)$$

The first term contains the usual gauge and Yukawa interactions and is invariant under super-Poincarè transformations, while the second term contains terms which are not invariant under the SUSY transformations. The second piece contains the “soft” terms with masses and couplings of positive mass dimension less than 4 which parametrize the effects of SUSY breaking. The most general form of  $\mathcal{L}_{\text{soft}}$  was found by Girardello and Grisaru [22].

### 2.1.2 Review of global and local SUSY

It is worth writing down the Lagrangian in a global supersymmetric theory which contains chiral and gauge fields invariant under SUSY and gauge transformations. To do this we consider a theory with  $i = 1, 2, \dots, n$  scalar fields  $\phi_i$  and their fermionic superpartners  $\psi_i$  along with gauge fields  $A_\mu^a$  and their corresponding spin half partner gauginos  $\lambda^a$  where  $a$  labels the gauge group  $\mathcal{G}_a$  with gauge couplings  $g_a$ . The fermionic fields are written using two component Weyl notation for both the chiral fields and gauginos. The Lagrangian for this theory is written as

$$\begin{aligned} \mathcal{L}_{\text{SUSY}} &= |D_\mu \phi_i|^2 + i\psi_i^\dagger \bar{\sigma}^\mu D_\mu \psi_i - \frac{1}{2} (W^{ij} \psi_i \psi_j + \text{h.c.}) - |W_i|^2 \\ &- \frac{1}{4} F_{\mu\nu}^a F^{\mu\nu a} + i\lambda^{a\dagger} \bar{\sigma}^\mu D_\mu \lambda^a + \frac{1}{2} (D^a)^2 \\ &- \sqrt{2}g_a ((\phi_i^* T^a \psi_i) \lambda^a + \text{h.c.}) + g_a (\phi_i^* T^a \psi_i) D^a, \end{aligned} \quad (2.4)$$

where  $W^{ij} = \partial^2 W / \partial \phi_i \partial \phi_j$ ,  $W^i = \partial W / \partial \phi_i$  and  $W = W(\phi)$  is a renormalizable holomorphic function of the scalar fields called the superpotential. The covariant derivatives for the scalar

and fermionic fields are

$$\begin{aligned}
D_\mu \phi_i &= \partial_\mu \phi_i + ig_a T^a A_\mu^a \phi_i \\
D_\mu \psi_i &= \partial_\mu \psi_i + ig_a T^a A_\mu^a \psi_i,
\end{aligned}
\tag{2.5}$$

where  $T^a$  are the generators of the gauge group  $\mathcal{G}_a$ . The gauge and gaugino fields have the following covariant derivatives

$$\begin{aligned}
F_{\mu\nu}^a &= \partial_\mu A_\nu^a - \partial_\nu A_\mu^a - g_a f^{abc} A_\mu^b A_\nu^c \\
D_\mu \lambda^a &= \partial_\mu \lambda^a - ig_a f^{abc} A_\mu^b \lambda^c,
\end{aligned}
\tag{2.6}$$

with  $f^{abc}$  the anti-symmetric structure constants of  $\mathcal{G}_a$ .

The results for the interacting global SUSY theory written in equation (2.4) can be somewhat simplified by working in superspace. In superspace one has spacetime coordinates  $x^\mu$  along with two component anti-commuting spinor coordinates  $\theta, \bar{\theta}$  (Grassmann spinors) which satisfy  $\{\theta_\alpha, \bar{\theta}_{\dot{\alpha}}\} = 0$  where  $\alpha, \dot{\alpha}$  are spinor indices. The fermionic and bosonic fields in a supermultiplet are then combined into a single superfield  $\Phi$ . Introducing a superspace coordinate  $y^\mu = x^\mu - i\theta\sigma^\mu\bar{\theta}$  the chiral fields are written in terms of a chiral superfield as

$$\Phi(y) = \phi(y) + \sqrt{2}\theta\psi(y) + \theta^2 F(y),
\tag{2.7}$$

with  $F$  an auxiliary field which is eliminated using the equations of motion to give  $W^i = F^i = \partial F / \partial \phi_i$ . The vector superfield contains the gauge, gaugino and auxiliary field  $D^a$

$$V^a(y) = \theta\sigma^\mu\bar{\theta}A_\mu^a(y) + \theta^2\bar{\theta}\lambda^{a\dot{1}}(y) + \theta\bar{\theta}^2\lambda^a(y) + \frac{1}{2}\theta^2\bar{\theta}^2 D^a(y),
\tag{2.8}$$

where  $D^a$  can be eliminated using the equations of motion to give  $D^a = -g_a (\phi_i^* T^a \phi_i)$ . It is

also convenient to introduce the field strength superfield  $W_\alpha^a$

$$W_\alpha^a(y) = -i\lambda_\alpha^a(y) + \theta_\alpha D^a(y) - (\sigma^{\mu\nu}\theta)_\alpha F_{\mu\nu}^a(y) - \theta^2 \sigma^\mu D_\mu \lambda^{a\dagger}(y), \quad (2.9)$$

with  $\alpha$  a spinor index. Using the superfields in equations (2.7) and (2.9) along with the superpotential,  $W(\Phi)$  (now a function of the chiral superfields), the SUSY Lagrangian in equation (2.4) becomes

$$\mathcal{L}_{\text{SUSY}} = \int d^4\theta [\Phi^\dagger e^{g_a T^a V^a} \Phi + \text{h.c.}] + \int d^2\theta \left[ \frac{1}{4} W^{a\alpha} W_\alpha^a + W(\Phi) + \text{h.c.} \right], \quad (2.10)$$

with superspace measures  $d^2\theta = -\frac{1}{4}d\theta d\theta$ ,  $d^2\bar{\theta} = -\frac{1}{4}d\bar{\theta}d\bar{\theta}$  and  $d^4\theta = d^2\theta d^2\bar{\theta}$ <sup>1</sup>. The general form of the global SUSY scalar potential at tree level is

$$V = \sum_i \left| \frac{\partial W}{\partial \phi_i} \right|^2 + \frac{1}{2} \sum_a g_a^2 \left( \sum_i \phi_i^\dagger T^a \phi_i \right)^2, \quad (2.11)$$

where  $T^a$  are the generators of the gauge group  $\mathcal{G}^a$  to which  $\phi_i$  belong with coupling constants  $g_a$ .

In local supersymmetry the SUSY generators are taken to depend on spacetime coordinates and therefore involve gravity. Local supersymmetry implies the existence of a massless spin 2 field which couples to matter as in General Relativity, e.g. a graviton along with its spin 3/2 fermionic partner, the gravitino. To include the effects of supergravity equation (2.10) is modified (working in units of  $M_{\text{Pl}} = 1$ ) according to

$$\mathcal{L}_{\text{SUSY}} = \int d^4\theta K(\Phi^\dagger e^{g_a T^a V^a}, \Phi) + \int d^2\theta \left[ \frac{1}{4} f_{ab}(\Phi) W^{a\alpha} W_\alpha^b + W(\Phi) + \text{h.c.} \right], \quad (2.12)$$

where  $K$  is the Kähler potential, a gauge invariant and real function and  $f_{ab}$  is an arbitrary function of the chiral superfields which is just  $\delta_{ab}$  in the global case. The scalar potential is

---

<sup>1</sup>For a single Grassmann variable,  $\eta$ , integration is defined as  $\int d\eta = 0$  and  $\int \eta d\eta = 1$ .

then

$$V = e^K [(D_m W) K^{m\bar{n}} (D_{\bar{n}} \bar{W}) - 3|W|^2] + \frac{g_a^2}{2} K_m (T^a \phi)^m (\bar{\phi} T^a)^{\bar{n}} K_{\bar{n}}, \quad (2.13)$$

where  $K^{m\bar{n}}$  is the inverse of the Kähler metric  $K_{m\bar{n}} = \partial^2 K / \partial \phi_m \partial \bar{\phi}_{\bar{n}}$ ,  $D_m W = \partial W / \partial \phi_m + W \partial K / \partial \phi_m$ ,  $D_{\bar{n}} \bar{W} = \partial \bar{W} / \partial \bar{\phi}_{\bar{n}} + \bar{W} \partial K / \partial \bar{\phi}_{\bar{n}}$  and  $K_m = \partial K / \partial \phi_m$ . The potential in local SUSY can now be negative in contrast to the global case in equation (2.11). The last term in equation (2.13) is just a  $D$ -term and the first term can be written using the  $F$ -term

$$F^m = e^{K/2} K^{m\bar{n}} D_{\bar{n}} \bar{W}. \quad (2.14)$$

If one or more of the  $F^m$  terms obtain a VEV, then local SUSY will be broken and the gravitino will absorb the goldstino and obtains a mass of

$$m_{3/2}^2 = \frac{F^m K_{m\bar{n}} F^{\bar{n}}}{3M_{\text{Pl}}^2}, \quad (2.15)$$

where  $M_{\text{Pl}}$  has been put back in. The gravitino mass is found from taking  $V = 0$  in equation (2.13) and assuming the  $D$ -term contribution to be zero.

### 2.1.3 $W_{\text{MSSM}}$ and $\mathcal{L}_{\text{soft}}^{\text{MSSM}}$

Returning to the discussion of the MSSM we now review the basic ingredients for the superpotential and soft SUSY breaking terms. The MSSM superpotential is

$$\begin{aligned} W_{\text{MSSM}} &= \hat{u}_{\mathbf{y}_u} \hat{Q} \hat{H}_u - \hat{d}_{\mathbf{y}_d} \hat{Q} \hat{H}_d - \hat{l}_{\mathbf{y}_e} \hat{L} \hat{H}_e + \mu \hat{H}_u \hat{H}_d \\ &= \eta_{\phi} \hat{\phi}_{\mathbf{y}_{\phi}} \hat{\Phi} \hat{H}_j + \mu \hat{H}_u \hat{H}_d, \end{aligned} \quad (2.16)$$

where a shorthand notation is used for the superfields so  $\phi \in \{u, d, l\}$ ,  $\Phi \in \{Q, L\}$ ,  $H_j \in \{H_u, H_d\}$  and  $\eta_u = +1, \eta_{d,l} = -1$ . The couplings in equation (2.16) are the Yukawa matrices

$\mathbf{y}_\phi$  and the supersymmetric Higgs mass  $\mu$ . The general soft SUSY Lagrangian for the MSSM is

$$\begin{aligned}
-\mathcal{L}_{\text{soft}}^{\text{MSSM}} &= \frac{1}{2} \left( M_a \tilde{\lambda}_a \tilde{\lambda}_a + \text{h.c.} \right) + \tilde{\Phi}^\dagger \mathbf{m}_\Phi^2 \tilde{\Phi} + \tilde{\phi}^\dagger \mathbf{m}_\phi^2 \tilde{\phi} \\
&+ \left( \eta_\phi \bar{\phi} \mathbf{a}_\phi \tilde{\Phi} H_j + \text{h.c.} \right) + m_j^2 |H_j|^2 + (b H_u H_d + \text{h.c.}) , \quad (2.17)
\end{aligned}$$

where  $M_a$  are the soft gaugino masses for  $\lambda_a = \tilde{B}, \tilde{W}, \tilde{g}$  ( $a = 1, 2, 3$ ),  $\mathbf{m}_{\phi, \Phi}^2$  are the soft scalar squared mass matrices,  $\mathbf{a}_\phi$  are the trilinear scalar couplings,  $b = B\mu$  is the soft Higgs bilinear and a shorthand notation is used as in equation (2.16).

The superpotential in equation (2.16) is minimal enough to build models with realistic phenomenology, but other terms could also be written down. Terms which are holomorphic and renormalizable like  $\alpha^{ijk} Q_i L_j \bar{d}_k$ ,  $\beta^{ijk} \bar{d}_i \bar{d}_j \bar{u}_k$  are allowed (with  $\beta_{ijk}$  antisymmetric in the family indices), however these type of terms violate lepton and baryon number and if such terms did exist then the coupling  $\beta_{ijk}$  could mediate rapid proton decay. For example the proton would have a half life on the order  $10^{-12}$  seconds if the coupling is  $\mathcal{O}(1)$  and the squarks have mass around 1 TeV, while the proton is known to be very stable with a lower bound on the half life of  $\mathcal{O}(10^{33})$  years [23, 24]. This can be alleviated if the coupling  $\beta^{ijk}$  is very small. Also  $B$  and  $L$  are known to be violated by non-perturbative electroweak effects. To remedy the issue of  $B$  and  $L$  conservation a discrete  $Z_2$  symmetry is introduced to the MSSM which eliminates the problematic terms in the superpotential. This is the so-called  $R$ -parity defined as

$$P_R = (-1)^{3(B-L)+2s} , \quad (2.18)$$

where  $B$  is the baryon number,  $L$  is the lepton number and  $s$  the spin of the particle. It follows that particles in the same supermultiplet have opposite  $R$ -parity, i.e. the SM fields all have  $P_R = +1$  (including the Higgs scalar fields) while the superpartners all have  $P_R = -1$  (including the Higgsino fields). Conservation of  $R$ -parity implies

- The lightest supersymmetric particle (LSP) must be absolutely stable and if neutral it

only interacts weakly, hence a DM candidate.

- Each superpartner decays to an odd number of LSPs plus SM particles.
- Superpartners are produced in pairs at colliders.

The MSSM is defined to conserve  $R$ -parity and thus can provide an explanation for the dark matter if a neutral odd  $R$  particle is the LSP, and this comes from imposing a symmetry to protect the proton from decaying too rapidly.

A further ansatz typically taken to study the MSSM is to eliminate potential flavor changing neutral currents and  $CP$  violation by assuming the squark and slepton mass matrices to be diagonal at the high scale

$$\begin{aligned} \mathbf{m}_\Phi^2 &= m_\Phi^2 \mathbf{1} \quad \text{for } \Phi = \tilde{Q}, \tilde{L}, \\ \mathbf{m}_\phi^2 &= m_\phi^2 \mathbf{1} \quad \text{for } \phi = \tilde{u}, \tilde{d}, \tilde{e}, \end{aligned} \tag{2.19}$$

where  $\mathbf{1}$  is  $3 \times 3$  unit diagonal in family space. Another assumption is that the scalar cubed couplings are proportional to the Yukawa matrices so

$$\mathbf{a}_\phi = A_\phi \mathbf{y}_\phi \quad \text{for } \phi = \tilde{u}, \tilde{d}, \tilde{e}. \tag{2.20}$$

Further typically one assumes  $\mathbf{y}_\phi \simeq \text{diag}(0, 0, y_\phi)$  so that only the third family particles have non-zero trilinears. To avoid the large new sources of  $CP$  violation the soft parameters will be taken to not introduce complex phases; in other words  $\mathcal{L}_{\text{soft}}^{\text{MSSM}}$  needs to be real. The soft scalar mass squares,  $m_\phi^2$ , are assumed real, phases of  $\mu$  and  $b = B\mu$  can be eliminated by rotating the Higgs and Higgsino fields and assuming the phases of the gaugino masses and trilinear couplings are 0 or  $\pi$ .

## 2.2 High scale models

Supersymmetry must be broken since no observed superpartners with the same mass as SM fields have been measured. Somehow SUSY breaking effects are communicated to the MSSM and just how this is done is unknown. SUSY breaking from an  $F$  or  $D$  term VEV in the MSSM supermultiplets of the observable sector is not allowed as there are no candidate singlets whose  $F$ -term could develop a VEV and the  $D$ -term VEV does not lead to an acceptable spectrum. Tree-level renormalizable terms cannot communicate breaking as this leads to sum rules of the (simplified) form  $m_{\tilde{e}_1}^2 + m_{\tilde{e}_2}^2 = 2m_e^2$  which are ruled out by experiment. To construct a viable way of communicating the breaking of SUSY to the MSSM one supposes that there is a “hidden” sector where the actual breaking of SUSY takes place and the subsequent breaking effects are transmitted to the observable sector via possibly flavor-blind interactions.

The interactions which mediate the breaking typically come from three types of mediation mechanisms: gravity, anomaly and gauge mediation. In gravity (or modulus) mediation models [25, 26, 27] the hidden sector where the SUSY breaking takes place communicates to the observable sector only through gravitational interactions. The supergravity effective Lagrangian then contains non-renormalizable terms which are suppressed by powers of  $M_{\text{Pl}}$ . Models of this type can avoid problems such as flavor changing neutral currents and  $CP$  violation if one assumes (or can explain) family universal couplings at the high scale. Typically the high scale at which unification takes place is the scale at which the gauge couplings unify,  $Q_{\text{GUT}} \simeq 1 \times 10^{16}$  GeV.

In anomaly mediation models [28, 29] the hidden sector is sequestered from the visible sector by some distance. In this case the soft terms arise from an anomalous violation of local superconformal invariance which is an extension of scale invariance. The soft terms which are generated are proportional to the beta functions and anomalous dimensions. Furthermore in theories of this type the flavor violating effects are suppressed via the exponential separation between the two sectors. The scale at which the soft terms are generated can vary, but

typically one assumes it to be at a high scale such as  $Q_{\text{GUT}}$ .

In gauge mediation models [30] the usual gauge interactions of the SM are responsible for transmitting SUSY breaking to the observable sector. New messenger fields are introduced which transmit the breaking indirectly. The soft terms arise at the loop level and the scale at which they are generated is often much lower than  $Q_{\text{GUT}}$ . In this case dangerous flavor violating effects are avoided as the soft terms are proportional to the gauge couplings.

### Connecting high and low scales

If one assumes a high scale model then in order to study the phenomenology which is relevant for experiments one must evolve the soft terms from the high scale down to the electroweak scale. The evolution is done using renormalization group equations which, for example, have been computed to the two loop level in the MSSM in [31]. Upon evolving the soft terms down the physical masses can then be computed including the radiative corrections [32]. The electroweak symmetry breaking conditions as discussed below can then be checked for consistency thus determining whether the model under question is viable.

## 2.3 Higgs potential and EWSB

Now we consider the Higgs scalar potential and conditions which arise for electroweak symmetry breaking. The tree level Higgs potential after setting charged Higgs components to zero is

$$\begin{aligned}
 V &= (|\mu|^2 + m_{H_u}^2) |H_u^0|^2 + (|\mu|^2 + m_{H_d}^2) |H_d^0|^2 + (bH_u^0 H_d^0 + \text{h.c.}) \\
 &+ \frac{1}{8} (g^2 + g'^2) (|H_u^0|^2 + |H_d^0|^2)^2 .
 \end{aligned}
 \tag{2.21}$$

In order to break electroweak symmetry  $SU(2)_L \times U(1)_Y \rightarrow U(1)_{EM}$  and give masses to the SM fermions certain stability conditions must be obeyed by the Higgs potential in equation (2.21). For the Higgs to get a non-zero VEV the origin cannot be a stable minimum which

is the same as requiring the matrix of second derivatives to obey  $\partial^2 V / \partial H_i^0 \partial H_j^{0*} < 0$ . The potential also needs to be bounded from below for large values of the scalar fields so that it will really have a minimum resulting in  $V > 0$  along the  $D$ -flat directions ( $H_u^0 = H_d^0$ ). These two conditions result in

$$\begin{aligned} b^2 &> (|\mu|^2 + m_{H_u}^2) (|\mu|^2 + m_{H_d}^2) \\ 2b &< 2|\mu|^2 + m_{H_u}^2 + m_{H_d}^2, \end{aligned} \tag{2.22}$$

with the first coming from  $\partial^2 V / \partial H_i^0 \partial H_j^{0*} < 0$  and the second from  $V(H_u^0 = H_d^0) > 0$ . If  $m_{H_u}^2 = m_{H_d}^2$  then the two conditions above cannot both be satisfied. Typically in models where the inputs are all equal at the GUT scale after evolving the parameters to the low scale one typically finds  $m_{H_u}^2 < m_{H_d}^2$ . This is a result of radiative corrections and is therefore called radiative electroweak symmetry breaking.

We can now look at the Higgs VEVs and what relations are required based on the stability conditions in equation (2.22). The Higgs fields in equation (2.21) are replaced with  $\langle H_u^0 \rangle = v_u$  and  $\langle H_d^0 \rangle = v_d$  where  $v_u^2 + v_d^2 = v^2 = 2m_Z^2 / (g^2 + g'^2) \simeq (174 \text{ GeV})^2$  and traditionally one defines  $\tan \beta = v_u / v_d$  with  $0 < \beta < \pi/2$ . Subsequent evaluation of  $\partial V / \partial v_i$  for  $i = u, d$  results in two equations which indeed satisfy the stability conditions in equation (2.22) and can be written as

$$\begin{aligned} \sin(2\beta) &= \frac{2b}{m_{H_d}^2 + m_{H_u}^2 + 2\mu^2} \\ \mu^2 &= \frac{m_{H_d}^2 - m_{H_u}^2 \tan^2 \beta}{\tan^2 \beta - 1} - \frac{1}{2} m_Z^2, \end{aligned} \tag{2.23}$$

which begs the following question: why should the SUSY preserving  $\mu$  term be of the same order of the electroweak scale and of the same order of the soft SUSY breaking parameters? Due to the hierarchy problem the soft scalar mass squared terms are expected to be  $\mathcal{O}(1 \text{ TeV})$ , whereas  $\mu$  is not renormalized and hence can take on any value. There is no reason to expect

$\mu$  to be near  $m_Z$ , but if it is not then large cancellations are required between  $m_H^2$  terms. These arguments give an overview of the so-called  $\mu$ -problem. This can be explained or understood by requiring  $\mu$  to vanish at tree-level and to be produced as a by-product of SUSY-breaking [33, 34, 35, 36, 37].

## 2.4 Superpartner masses

Here we only include the tree level contributions using (mostly) the notation of [14]. The masses are presented in the absence of  $CP$  phases, e.g. the parameters are all taken as real valued. The scalar Higgs sector of the MSSM consists of two complex doublets with 8 degrees of freedom. After EWSB 3 of these degrees of freedom are absorbed to become the longitudinal modes of the  $Z$  and  $W$  as they gain mass and the remaining 5 are the two neutral Higgs fields  $h$  and  $H$ , the pseudo-scalar Higgs,  $A$  and the two charged Higgs scalars  $H^\pm$ . These Higgs masses are given at the tree-level by

$$\begin{aligned}
m_A^2 &= 2|\mu|^2 + m_{H_u}^2 + m_{H_d}^2 \\
m_{h,H}^2 &= \frac{1}{2} \left[ m_A^2 + m_Z^2 \mp \sqrt{(m_A^2 - m_Z^2)^2 + 4m_Z^2 m_A^2 \sin^2(2\beta)} \right] \\
m_{H^\pm}^2 &= m_A^2 + m_Z^2.
\end{aligned} \tag{2.24}$$

The two neutral Higgs mass-eigenstate fields  $h$  and  $H$  (with  $m_h^2 < m_H^2$  by convention) are a mix of the neutral gauge-eigenstate fields as

$$\begin{pmatrix} h \\ H \end{pmatrix} = \sqrt{2} \begin{pmatrix} \cos \alpha & -\sin \alpha \\ \sin \alpha & \cos \alpha \end{pmatrix} \begin{pmatrix} \text{Re}H_u^0 \\ \text{Re}H_d^0 \end{pmatrix}, \tag{2.25}$$

with the mixing angle  $\alpha$  given by

$$\frac{\sin(2\alpha)}{\sin(2\beta)} = -\frac{m_A^2 + m_Z^2}{m_H^2 - m_h^2}, \quad \frac{\cos(2\alpha)}{\cos(2\beta)} = -\frac{m_A^2 - m_Z^2}{m_H^2 - m_h^2}. \tag{2.26}$$

Next we consider the superpartners of the quarks and leptons. A common practice is to write the squark mass eigenstates in the CKM basis, the so-called super-CKM basis (SCKM). In this manner one diagonalizes the squarks using  $6 \times 3$   $\mathbf{\Gamma}$  matrices and the sleptons are diagonalized using  $3 \times 3$   $\mathbf{\Gamma}$  matrices [38]

$$\begin{aligned}\tilde{f}_{La} &= \sum_{k=1}^6 \tilde{f}_k \mathbf{\Gamma}_{FL}^{*ka} \\ \tilde{f}_{Ra} &= \sum_{k=1}^6 \tilde{f}_k \mathbf{\Gamma}_{FR}^{*ka},\end{aligned}\tag{2.27}$$

where  $\tilde{f}_k$  are the mass eigenstates ( $k = 1, \dots, 6$  for  $\tilde{e}_k, \tilde{u}_k, \tilde{d}_k$  and  $k = 1, 2, 3$  for  $\tilde{\nu}_k$ ),  $\tilde{f}_{La}$  and  $\tilde{f}_{Ra}$  are the gauge eigenstates with  $a = 1, 2, 3$  and the subscript  $F = U, D, E$ . Here we just review the third generation masses which are mixings of the gauge-eigenstate fields, for example the gauge-eigenstate stop masses are from the Lagrangian term

$$\mathcal{L}_{m_{\tilde{t}}} = - \begin{pmatrix} \tilde{t}_L^* & \tilde{t}_R^* \end{pmatrix} \mathbf{m}_{\tilde{t}}^2 \begin{pmatrix} \tilde{t}_L \\ \tilde{t}_R \end{pmatrix},\tag{2.28}$$

with the stop mass matrix given by

$$\mathbf{m}_{\tilde{t}}^2 = \begin{pmatrix} m_{Q_3}^2 + m_t^2 + \delta_u & m_t (A_t - \mu \cot \beta) \\ m_t (A_t - \mu \cot \beta) & m_{\bar{u}_3}^2 + m_t^2 + \delta_{\bar{u}} \end{pmatrix}.\tag{2.29}$$

The term  $\delta_f$  for a flavor  $f$  is given by

$$\delta_f = m_Z^2 (T_f^3 - Q_f \sin^2 \theta_W) \cos(2\beta).\tag{2.30}$$

To obtain the mass-eigenstates,  $\tilde{t}_1$  and  $\tilde{t}_2$ , one diagonalizes the matrix in equation (2.29)

using

$$\begin{pmatrix} \tilde{t}_1 \\ \tilde{t}_2 \end{pmatrix} = \begin{pmatrix} \cos \theta_{\tilde{t}} & -\sin \theta_{\tilde{t}} \\ \sin \theta_{\tilde{t}} & \cos \theta_{\tilde{t}} \end{pmatrix} \begin{pmatrix} \tilde{t}_L \\ \tilde{t}_R \end{pmatrix}, \quad (2.31)$$

where the  $\mathbf{\Gamma}$  matrices from equation (2.27) are related to  $\theta_{\tilde{t}}$  as  $\Gamma_{UL}^{\tilde{t}_1\tilde{t}} = \Gamma_{UR}^{\tilde{t}_2\tilde{t}} = \cos \theta_{\tilde{t}}$  and  $\Gamma_{UL}^{\tilde{t}_2\tilde{t}} = -\Gamma_{UR}^{\tilde{t}_1\tilde{t}} = \sin \theta_{\tilde{t}}$ . For the sbottom and stau masses the same general approach is taken with the mass matrices of the same form as in equation (2.29) but with the replacements  $\sin \beta \rightarrow \cos \beta$ ,  $\cos \beta \rightarrow \sin \beta$ ,  $m_t^2 \rightarrow m_b^2$ ,  $A_t \rightarrow A_b$ , and similarly for  $\tau$ .

Finally we look in a bit of detail at the gaugino masses, as the gaugino masses are a central part of the work presented here. In the MSSM gauge-interaction basis we have the following forms of the gaugino sector masses

$$\mathcal{L}_{m_{\tilde{g}}} = -\frac{1}{2}M_3\tilde{g}\tilde{g} + \text{h.c.} \quad (2.32)$$

$$\mathcal{L}_{m_{\tilde{N}}} = -\frac{1}{2}(\psi^0)^T \mathcal{M}_{\tilde{N}}\psi^0 + \text{h.c.} \quad (2.33)$$

$$\mathcal{L}_{m_{\tilde{C}}} = -\frac{1}{2}(\psi^\pm)^T \mathcal{M}_{\tilde{C}}\psi^\pm + \text{h.c.} \quad (2.34)$$

The gluino mass is given at tree level by  $M_3$  and the pole mass including the one-loop radiative corrections can be found in [39]. In the gauge-eigenstate basis the wavefunctions are  $\psi^0 = (\tilde{B}, \tilde{W}^0, \tilde{H}_d^0, \tilde{H}_u^0)$  and  $\psi^\pm = (\tilde{W}^+, \tilde{H}_u^+, \tilde{W}^-, \tilde{H}_d^-)$ . The neutralino and chargino mass matrices are

$$\mathcal{M}_{\tilde{N}} = \begin{pmatrix} M_1 & 0 & -c_\beta s_W m_Z & s_\beta s_W m_Z \\ 0 & M_2 & c_\beta c_W m_Z & -s_\beta c_W m_Z \\ -c_\beta s_W m_Z & c_\beta c_W m_Z & \delta_{33} & -\mu \\ s_\beta s_W m_Z & -s_\beta c_W m_Z & -\mu & \delta_{44} \end{pmatrix} \quad (2.35)$$

$$\mathcal{M}_{\tilde{C}} = \begin{pmatrix} 0 & X^T \\ X & 0 \end{pmatrix} \quad X = \begin{pmatrix} M_2 & \sqrt{2}s_\beta m_W \\ \sqrt{2}c_\beta m_W & \mu \end{pmatrix}. \quad (2.36)$$

In the mass matrices  $c_\beta = \cos \beta$ ,  $s_\beta = \sin \beta$ ,  $c_W = \cos \theta_W$ ,  $s_W = \sin \theta_W$  where  $\theta_W$  is the Weinberg angle ( $e = g \sin \theta_W$ ). The diagonal  $\delta$ 's are 1-loop corrections which become important when the LSP has a sizable Higgsino and/or Wino fraction [40]. One can also write the off diagonal terms using the  $SU(2)_L$  and  $U(1)_Y$  gauge couplings  $g$  and  $g'$  via  $c_W = g/\sqrt{g^2 + g'^2}$ ,  $s_W = g'/\sqrt{g^2 + g'^2}$ ,  $v = \sqrt{v_u^2 + v_d^2} = 174$  GeV,  $\tan \beta = v_u/v_d$ ,  $m_Z^2 = (g^2 + g'^2)v^2/4$  and  $m_W = g^2v^2/4$ .

In general the parameters  $M_a$  ( $a = 1, 2, 3$ ) and  $\mu$  are complex. Then the neutralino mass matrix is not Hermitian, but it is complex and symmetric, whereas the chargino mass matrix is not Hermitian or symmetric, it is a general complex matrix. This results in different diagonalization procedures. To diagonalize the neutralino matrix one simply rotates to the mass eigenstate basis via a unitary matrix  $\mathbf{N}$ . To diagonalize the chargino mass matrix one needs two unitary matrices  $\mathbf{U}$  and  $\mathbf{V}$ , which are required to diagonalize a general complex matrix via a biunitary transformation. The unitary matrices relate the gauge and mass eigenstate bases as follows

$$\tilde{N}_i = \mathbf{N}_{ij}\psi_j^0, \quad \tilde{C}_i^+ = \mathbf{V}_{ij}\psi^+, \quad \tilde{C}_i^- = \mathbf{U}_{ij}\psi^- \quad (2.37)$$

where  $\psi^+ = (\tilde{W}^+, \tilde{H}_u^+)$  and  $\psi^- = (\tilde{W}^-, \tilde{H}_d^-)$ . Therefore the mass matrices in the diagonal basis are

$$\mathcal{M}_{\tilde{N}}^{\text{diag}} = \mathbf{N}^* \mathcal{M}_{\tilde{N}} \mathbf{N}^{-1} \quad (2.38)$$

$$\mathcal{M}_{\tilde{C}}^{\text{diag}} = \mathbf{U}^* \mathbf{X} \mathbf{V}^{-1}. \quad (2.39)$$

### Diagonalizing $\mathcal{M}_{\tilde{N}}$

Following [41] and [42] we review the method of diagonalizing  $\mathcal{M}_{\tilde{N}}$ . Reference [41] notes that if we assume  $CP$  invariance we can replace the Hermitian matrix  $\mathbf{N}$  with a real matrix

**Z**. Upon replacing  $\mathbf{N} \rightarrow \mathbf{Z}$  we have the following conditions for diagonalizing  $\mathcal{M}_{\tilde{N}}$

$$\mathbf{Z}\mathcal{M}_{\tilde{N}}\mathbf{Z}^{-1} = \text{diag}(\epsilon_1 m_{\tilde{N}_1}, \epsilon_2 m_{\tilde{N}_2}, \epsilon_3 m_{\tilde{N}_3}, \epsilon_4 m_{\tilde{N}_4}) = \mathcal{M}_{\tilde{N}}^{\text{diag}} \quad \mathbf{Z}^T \mathbf{Z} = 1 \quad (2.40)$$

where  $\epsilon_i$  is the sign of the  $i^{\text{th}}$  mass eigenvalue and the eigenvalues  $m_{\tilde{N}_i}$  are always positive. The matrices  $\mathbf{N}$  and  $\mathbf{Z}$  are then related as  $\mathbf{N}_{ij} = \sqrt{\epsilon_i} \mathbf{Z}_{ij}$  with no sum on  $i$ . Upon doing this one then solves

$$\mathbf{Z}\mathcal{M}_{\tilde{N}} - \mathcal{M}_{\tilde{N}}^{\text{diag}}\mathbf{Z} = 0 \quad \& \quad \mathbf{Z}^T \mathbf{Z} = 1 \quad (2.41)$$

to obtain the analytic formula of the terms  $\epsilon_i m_{\tilde{N}_i}$  along with the entries  $\mathbf{Z}_{ij}$  in terms of the entries in equation (2.35), which are assumed real. The results of this procedure for  $\epsilon_i m_{\tilde{N}_i}$  are rather lengthy and are given in references [41], [42] as well as in appendix A of [43] (which is a good reference for LSP dark matter). Note the mass eigenvalues are not necessarily ordered from least to greatest and one must do this, and shift the corresponding eigenvectors as well.

## 2.5 Gaugino sector

The stance taken here is that SUSY in the form of the MSSM is the BSM effective theory that will be discovered at the LHC. The possible parameter space of the MSSM is dimension 124, an immense space indeed. When considering GUT's on the other hand such as mSUGRA [25, 44] the parameter space of SUSY is reduced to dimension 4 and a sign. Although the high scale theories are very compelling for obvious reasons, as data reveals signals of SUSY the general low scale effective theory will be fit using collider and dark matter detection data. As an example this data will come in the form of various kinematic distributions of final state decay topologies at the LHC and count rates at dark matter direct detection experiments. Fitting the many possible explanations of signals of SUSY in general at the low scale will indeed be a highly difficult problem.

Bridging the gap from the SUSY effective Lagrangian at the low scale  $\mathcal{O}(\text{TeV})$  to some high scale theory, at  $2 \times 10^{16}$  GeV for example, may not turn out to be easy. Determining the mechanism responsible for breaking SUSY is a very important problem, and if such information can be harvested from the low scale measurements, then this will be very useful. For example if one could rule out gauge-mediation completely or determine that gravity-mediation is definitely responsible for the breaking, then the possible space of high scale theories could be vastly reduced. This information is very valuable as is the value of the  $\mu$  parameter, for example. Of all the possible superpartners which may be found one sector of particles is very intriguing as it contains information highly correlated to the issues just discussed. This is the gaugino sector, which contains the fermionic superpartners to the SM gauge bosons as well as new Higgs states.

In particular the soft gaugino masses  $M_a$  with  $a = 1, 2, 3$  for  $U(1)_Y$ ,  $SU(2)_L$  and  $SU(3)_C$  SM gauge groups are of extreme interest. The  $\mu$  parameter is also highly important along with the value of  $\tan \beta$ . The soft gaugino masses offer a clean window into many possible patterns which can be tied back to the form of mediation mechanism responsible for the breaking of SUSY. The  $\mu$  parameter is an important parameter to understand as well as it is intimately related to the issue of EWSB and to understand its origin will shed important light on possible high scale motivated mechanisms which are responsible for its existence. The value of  $\tan \beta$  is also highly correlated to understanding EWSB as it governs the ratio of the Higgs VEVs. These parameters at the tree level completely describe the gaugino sector of the MSSM, as seen in equations (2.32), (2.35) and (2.36); therefore studying the gaugino sector of the MSSM is highly motivated.

In particular the MSSM contains the lightest neutralino, or LSP. The LSP wavefunction is made up at the tree level by the parameters  $M_1$ ,  $M_2$ ,  $\mu$  and  $\tan \beta$  as well as the  $U(1)_Y$  and  $SU(2)_L$  gauge couplings  $g'$ ,  $g$  and the  $Z$  boson mass. Measuring the mass and understanding the make-up of the LSP will provide important insight to the gaugino sector as a whole, as well as the suitability of the LSP as a solution to the dark matter problem. The gluino mass

will likely play an important role at the LHC, and if it is of low mass the possible event rates will be largely dominated by gluino and associated production. Understanding the ratios of  $M_1$ ,  $M_2$  and  $M_3$  gives information on the possible high scale model.

## 2.6 Signals of SUSY

Many experimental arenas can help to understand and place limits on the possible SUSY models which may exist. Here the main focus of the experimental efforts will be on both astrophysical and collider measurements. Other experimental data from electroweak precision measurements and observations of rare decays can also be useful. The basic implications for dark matter and collider signals of SUSY are briefly introduced below.

### 2.6.1 Dark matter

As mentioned in the discussion of  $R$ -parity conservation the MSSM offers a possible explanation for the dark matter in the cosmos. In  $R$ -parity conserving models the lightest supersymmetric particle is stable and is an excellent candidate for a dark matter particle [45]. Two aspects of dark matter are important and mostly disconnected: the thermal abundance of the relic LSP and the dark matter experimental signatures that arise from neutralinos currently in the cosmos.

The thermal relic abundance of the LSP can account for the observed abundance measurement by WMAP of

$$\Omega_\chi h^2 \simeq 0.11, \quad (2.42)$$

although the measurement is based on the standard cosmological model which requires basic assumptions as to the thermal history of the universe.

Detection of LSPs is also an important probe of possible SUSY models. Detection experiments include both measuring direct interaction of LSPs with terrestrial detectors as well as measuring byproducts of LSP annihilation such as gamma rays, anti-matter and muons.

Predictions for a given SUSY model in the direct and indirect arenas can be made, although some of these require inferences of astrophysical properties. Identifying the dark matter as a weakly interacting massive particle (WIMP) will be a powerful hint at the existence of SUSY and the various observations from direct and indirect detection experiments can be used to help reveal the properties of the LSP. Further discussion of LSP dark matter and the relevance to detection is discussed further in the next chapter.

## 2.6.2 Colliders

Colliders will be the best tools with which to probe the BSM physics. The entire SUSY model will become important for these experiments, assuming that the particles are kinematically accessible. The focus of this work will be on the Large Hadron Collider as it will be taking data in the near future at the highest energies yet probed in a controlled environment. The basics of collider signals which are associated with SUSY can be found for example in [46, 1, 47] and references therein.

The LHC is a proton-proton collider which is designed to reach a center of mass energy of  $\sqrt{s} = 14$  TeV. Distinctive signatures which arise in  $R$ -parity conserving SUSY models are typically large missing transverse energy ( $\cancel{E}_T$ ) associated with the LSPs which escape detection. Other channels offer promising discovery such as the trilepton signal with  $\cancel{E}_T$ , for example. Certain kinematic distributions can offer important clues such as the dilepton invariant mass of the effective mass of jets and missing  $p_T$ . Typically one studies aspects of SUSY models by investigating useful signatures which arise from the decays of various produced superpartners.

# Chapter 3

## Dark matter and the LSP

In this chapter basic properties relevant to the relic abundance and detection of LSPs are discussed. In particular the detection methods and relevant calculations are discussed which will be used later in multiple places. Many reviews exist on dark matter and the possible explanation using the LSP of the MSSM, here is a partial list: [48, 49, 43, 50, 51].

Various SUSY particles can potentially describe the dark matter in the universe such as the gravitino, the sneutrino and the lightest neutralino. The gravitino interacts only via gravitational interactions and is essentially not detectable [52] while the sneutrino has mostly been ruled out via direct searches [53]. In  $R$ -parity conserving SUSY models the lightest neutralino is highly motivated as a dark matter particle since it is stable, weakly interacting, it can give the right relic density [45, 54]. In this work we will assume that the LSP is the lightest neutralino of the MSSM.

The properties of the  $\tilde{N}_1$  are highly relevant for dark matter: its mass  $m_{\tilde{N}_1}$  and its wavefunction composition (occasionally the notation  $m_\chi$  or  $m_{\tilde{\chi}}$  will also be used to denote the LSP mass and it should be obvious from the context). The wavefunction composition governs the allowed interactions of the LSP with matter and typically one discusses the gaugino fractions: Bino fraction,  $f_B$ , and Wino fraction,  $f_W$ , along with the Higgsino fraction:  $f_H$ . Going back to equation (2.37) and assuming  $CP$ -invariance so the entries in equation (2.35) are real,  $\tilde{N}_1$  is written as a linear combination of the gauge interaction states  $\tilde{B}, \tilde{W}^0, \tilde{H}_d^0, \tilde{H}_u^0$

$$\tilde{N}_1 = Z_{11}\tilde{B} + Z_{12}\tilde{W}^0 + Z_{13}\tilde{H}_d^0 + Z_{14}\tilde{H}_u^0. \quad (3.1)$$

The components of  $\tilde{N}_1$  can also be written in terms of the Bino, Wino and Higgsino fractions

as

$$f_B = Z_{11}^2, \quad f_W = Z_{12}^2 \quad \text{and} \quad f_H = Z_{13}^2 + Z_{14}^2. \quad (3.2)$$

### 3.1 Relic density

Here we highlight some important steps of the calculation. The cosmological density of dark matter of a WIMP,  $\chi$ , is

$$\Omega_\chi = \frac{\rho_\chi}{\rho_c} \quad (3.3)$$

where the critical closure density is  $\rho_c = \frac{3H^2}{8\pi G_N} \simeq 1.05 \times 10^{-5} h^2 \text{ GeV/cm}^3$  with  $H$  the Hubble parameter and  $h$  the scaled Hubble parameter defined by  $H = 100h \text{ km}/(\text{s}\times\text{Mpc})$ . The dark matter density of mass  $m_\chi$  and number density  $n_\chi$  is  $\rho_\chi = m_\chi n_\chi$ . In order to determine the current number density of  $\chi$  one solves the Boltzmann transport equation which can be written as [55]

$$\frac{dn_\chi}{dt} + 3Hn_\chi = -\langle\sigma v\rangle (n_\chi^2 - (n_\chi^{\text{eq}})^2), \quad (3.4)$$

with  $\sigma v$  the total annihilation cross section ( $\chi\chi \rightarrow \text{SM}$ ) times relative velocity and the brackets denote thermal averaging. In equation (3.4)  $H$  is the Hubble parameter, related to the expansion of the universe, and  $n_\chi^{\text{eq}}$  is the number density at thermal equilibrium. Assuming non-relativistic particles and matching solutions for  $n_\chi$  before and after freezeout, the present day thermal abundance is then

$$\Omega_\chi h^2 \simeq \frac{1.07 \times 10^9 \text{ GeV}^{-1}}{\sqrt{g_*} M_{\text{Pl}} \int_0^{y_f} \langle\sigma v\rangle dy}, \quad (3.5)$$

where  $y = T/m$  and with the subscript  $f$  denoting the freezeout temperature,  $T_f$ , found by iteratively solving

$$y_f^{-1} = \ln \left( \frac{0.038 g M_{\text{Pl}} m_\chi \langle\sigma v\rangle \sqrt{y_f}}{\sqrt{g_*}} \right), \quad (3.6)$$

where  $M_{\text{Pl}} = 2.4 \times 10^{18}$  GeV,  $g$  is the number of degrees of freedom of  $\chi$  (spin, color, etc) and  $g_*$  is the number of effective relativistic degrees of freedom of  $\chi$  at freezeout. Note the present day abundance is proportional to the inverse of the annihilation cross section of  $\chi$  in equation (3.7). The calculation of  $\langle\sigma v\rangle$  is crucial to determining  $\Omega_\chi h^2$  and is sometimes approximated as  $\langle\sigma v\rangle = a + b\langle\sigma v^2\rangle + \mathcal{O}(\langle\sigma v^4\rangle)$ , although important exceptions exist [56] which need to be accounted for. These include co-annihilations of slightly heavier state(s),  $\chi'$ , when  $m_{\chi'} - m_\chi \simeq T_f$  and one must consider not only  $\chi\chi \rightarrow \text{SM}$  but also  $\chi\chi' \rightarrow \text{SM}$  in the calculation of  $\langle\sigma v\rangle$ . Special care also needs to be taken when computing annihilation into forbidden channels, when the LSP is slightly below mass threshold of an annihilation channel which would dominate the cross section, as taking the thermal average these annihilations will take place at some rate (for example  $\tilde{g}\tilde{g}(\tilde{t}_1\tilde{t}_1)$  annihilation in  $\tilde{g}(\tilde{t}_1)$  NLSP models). Lastly if annihilation takes place near a pole in the cross section where an  $s$ -channel resonance can occur the cross section can be approximated as

$$\sigma v \simeq \frac{\alpha_\phi^2 s}{(m_\phi^2 - s)^2 - m_\phi^2 \Gamma_\phi^2}, \quad (3.7)$$

where  $\phi$  is some gauge boson or scalar field with mass  $m_\phi$  and decay width  $\Gamma_\phi$ , and  $\alpha_\phi$  is an  $\mathcal{O}(10^{-2})$  coupling constant, e.g. of electroweak strength. In this case the value of  $\langle\sigma v\rangle$  becomes very sensitive to  $s$ -channel exchange of  $\phi$  due to the pole and near  $2m_\chi \simeq m_\phi$  resonance annihilation occurs and  $\Omega_\chi h^2$  is highly depleted. In the MSSM this feature can occur when  $2m_{\tilde{N}_1} \simeq m_A$  [57], the so-called ‘‘Higgs-funnel’’.

Various codes exist which can calculate the present day thermal abundance of relic neutralinos in the MSSM including co-annihilations. Two of the more popular codes are `DarkSUSY` [58] and `micrOMEGAs` [59]. In what follows `DarkSUSY 5.0.4` is the code of choice by which the thermal relic abundance will be calculated along with direct and indirect detection observables. A full list of the included co-annihilation channels considered in computing  $\Omega_\chi h^2$  which `DarkSUSY` uses may be found in table 3 of [58].

Important exceptions to the usual assumptions outlined above may result in changes to the relic density. Non-thermal production mechanisms in the early universe may enhance the present day WIMP abundance. Here the WIMP abundance is increased by the decay of heavier particles such as gravitinos in supergravity models, or in SUSY models with a Peccei-Quinn symmetry LSPs could come from decays of axinos (SUSY partner of the Peccei-Quinn axion) [48] also see [60, 61, 62]. The presence of a scalar field in the early Universe can also significantly alter the value of the relic density [63]. Furthermore it is likely that more than one object make up the dark matter in the Universe today, or in other words that one should write

$$\Omega_{\text{dm}} = \sum_i \Omega_{\text{dm},i}, \quad (3.8)$$

for the different contributions  $\Omega_{\text{dm},i}$  to the dark matter [64]. For example neutrinos contribute, although a small amount, but surely one ought not rule out the possibility of other contributions to the dark matter in the universe.

## 3.2 Direct detection

One of the more promising methods for detecting WIMP dark matter are direct detection experiments. These experiments seek to detect WIMP-nucleon scattering by measuring nuclear recoil energies from elastic scatters or by measuring ionization of the target nucleus for inelastic scatters [65]. As experiments measure counting rates, the focus here will be on carrying out the calculation of interaction rates of LSPs with target nuclei.

A simple estimate of the rate of neutralino-nucleon scattering events in units of events/(kg×day) can be found from [48]

$$R \sim \sum_i \Phi_\chi \frac{\sigma_{\chi^i}^{\text{SI}}}{M_i} = \sum_i \frac{\langle v_\chi \rangle \rho_\chi \sigma_{\chi^i}^{\text{SI}}}{m_\chi M_i}, \quad (3.9)$$

where  $\Phi_\chi$  is the average neutralino flux through the detector,  $\langle v_\chi \rangle$  is the average neutralino velocity relative to the target (around 250 km/s) and  $M_i$  is mass of nucleon species  $i$  in the

target. The cross section of neutralino scattering off nuclear target  $i$  is  $\sigma_{\chi i}$  and  $\rho_\chi$  is the local halo density of relic neutralinos.

The local density is typically quoted as  $\rho_\chi = 0.3 \text{ GeV}/\text{cm}^3$ , and is related to the relic abundance. A value of  $\Omega_\chi h^2_{\text{min}} = 0.025$  is a crude measure by which the relic particle under consideration no longer adequately represents the local halo density of our galaxy [48] see also [66]. If one takes the thermal calculation as the true amount of relic abundance and it is  $\Omega_\chi h^2 < \Omega_\chi h^2_{\text{min}}$ , then it ought to be rescaled to reflect that the remainder of dark matter must be from some other particle not accounted for. To this end a rescaling factor,  $r_\chi$ , is sometimes used to account for an underabundant relic

$$r_\chi = \text{Min}(1, \Omega_\chi h^2 / 0.025). \quad (3.10)$$

The cross section for interaction is computed in the non-relativistic limit. The lightest neutralino in the MSSM is a Majorana particle and is its own antiparticle. It has no conserved quantum number and does not have vector or tensor interactions. Furthermore the pseudo-scalar interaction does not survive the non-relativistic limit. Hence the LSP only interacts via scalar, spin-independent (SI), or axial-vector, spin-dependent (SD) interactions. The scalar interactions arise via  $s$ -channel squark and  $t$ -channel Higgs exchange as well as 1-loop scattering of LSPs from gluons in the nuclei. The axial vector interaction arises via  $s$ -channel squark or  $t$ -channel  $Z$  boson exchange. The two cross section are

$$\sigma_{\chi i}^{\text{SI}} = \frac{\mu_{\chi i}^2}{\pi} |ZG_s^p + (A - Z)G_s^n|^2, \quad (3.11)$$

$$\sigma_{\chi i}^{\text{SD}} = \frac{4\mu_{\chi i}}{\pi} \frac{J + 1}{J} |\langle S_p \rangle G_a^p + \langle S_n \rangle G_a^n|^2, \quad (3.12)$$

where the subscripts  $s$  and  $a$  denote scalar and axial vector interactions, the coefficients  $G_{a,s}^{n,p}$  are the LSP-nucleon couplings,  $A$  is the number of nucleons,  $Z$  the number of protons,  $J$  is the nuclear spin and  $\langle S_{n,p} \rangle$  are spin expectation values in the nucleus. The term  $\mu_{\chi i} =$

$m_\chi M_i / (m_\chi + M_i)$  is the reduced mass of the nucleus-neutralino system. In targets with large atomic numbers, such as germanium (Ge) and xenon (Xe), the scalar interaction dominates as it is coherent across all nucleons. In what follows we will consider large mass targets and therefore only focus on the SI interaction. The LSP-nucleon couplings for the SI interactions are

$$G_s^N = \sum_{q=u,d,s,c,b,t} \langle N | \bar{q}q | N \rangle \times \left( \frac{1}{2} \sum_{i=1}^6 \frac{g_{L\tilde{q}_i\chi q} g_{R\tilde{q}_i\chi q}}{m_{\tilde{q}_i}^2} - \sum_{j=h,H} \frac{g_{j\chi\chi} g_{jqq}}{m_j^2} \right), \quad (3.13)$$

where the couplings  $g$  are given below and  $\sum_q \langle N | \bar{q}q | N \rangle$  are the nuclear matrix elements. The forms for the couplings  $g$  are [38]

$$\begin{aligned} g_{h\chi\chi} &= (gZ_{12} - g'Z_{11}) (-\cos\alpha Z_{13} + \sin\alpha Z_{14}) \\ g_{H\chi\chi} &= (gZ_{12} - g'Z_{11}) (\sin\alpha Z_{13} + \cos\alpha Z_{14}) \\ g_{hqq} &= -Y_q \frac{\cos\alpha}{\sqrt{2}} \\ g_{Hqq} &= Y_q \frac{\sin\alpha}{\sqrt{2}} \\ g_{L\tilde{q}_i\chi q} &= -\frac{1}{\sqrt{2}} \left( gT_3^q Z_{12} + \frac{1}{3} g'Z_{11} \right) \Gamma_{QL}^{iq} + (-Y_q Z_{1j}) \Gamma_{QR}^{iq} \\ g_{R\tilde{q}_i\chi q} &= (-Y_q Z_{1j}) \Gamma_{QL}^{iq} + \left( \sqrt{2} e_q g' Z_{11} \right) \Gamma_{QR}^{iq}. \end{aligned} \quad (3.14)$$

where  $Y_q = m_q/v_u$ ,  $Z_{1j} = Z_{13}$  for  $q = u, c, t$ ,  $Y_q = m_q/v_d$ ,  $Z_{1j} = Z_{14}$  for  $q = d, s, b$  and the subscript on the  $\Gamma$ 's is  $Q = U, D$ , depending on the squark exchanged. The Higgs mixing angle  $\alpha$  as in (2.25) and the  $6 \times 3$  matrices  $\Gamma$  diagonalize the squark mass matrices in the SCKM basis [38] as in equation (2.27).

It is important to consider further the nuclear matrix elements in equation (3.13). They have not been calculated from first principles and rather the values are inferred from pion-nucleon scattering. The  $\sigma_{\pi N}$  term in the matrix elements is currently not well understood and has large errors resulting in large uncertainties in the value of  $\sigma_{\chi p}^{\text{SI}}$ , as initially brought up by Ellis et al. [67]. Ellis et al. showed that the uncertainties in  $\sigma_{\chi p}^{\text{SI}}$  could be on the  $\mathcal{O}(50\%)$  level with similar results found by others [68]. Hopefully this uncertainty can be

brought under control in the future so that reliable predictions can be made for the value of  $\sigma_{\chi p}^{\text{SI}}$ .

To predict the rates of interaction one starts with the differential rate of interaction per nuclear recoil energy

$$\frac{dR}{dE} = \sum_i c_i \frac{\rho_\chi \sigma_{\chi i} |F_i(q_i)|^2}{2m_\chi \mu_{i\chi}^2} \int_{v_{\min}}^{\infty} \frac{f(\vec{v}, t)}{v} d^3v. \quad (3.15)$$

where  $c_i$  is the fraction of nuclear species  $i$ ,  $|F_i(q_i)|^2$  is the nuclear form factor of species  $i$  with  $q_i = \sqrt{2M_i E}$  is the momentum transfer for nuclear recoil energy  $E$ . The neutralino velocity distribution is usually taken to be Maxwellian with  $v$  the relative velocity between the LSP and detector. The nuclear recoil energies are typically in the range  $\mathcal{O}(5 - 100)$  keV. To make contact with an experiment recoil energy ranges are chosen in certain ranges,  $E_{\min} \leq E \leq E_{\max}$ , which attempt to mimic the detection capabilities of various experiments. For example in the first run of XENON10 (Xe target) [69] and CDMS II (Ge target) [70] the recoil energies considered were in the ranges

$$\begin{aligned} \text{CDMS II} & : 10 \text{ keV} \leq E_{\text{recoil}} \leq 100 \text{ keV} \\ \text{XENON10} & : 4.5 \text{ keV} \leq E_{\text{recoil}} \leq 26.9 \text{ keV}. \end{aligned} \quad (3.16)$$

These ranges are based on the physics of the detector and seek to maximize signal significance over background. The method employed to calculate rates is then to compute  $dR/dE$  in equation (3.15) in 0.5 to 1 keV intervals over the ranges

$$\begin{aligned} R_1 & : 5 \text{ keV} \leq E_{\text{recoil}} \leq 25 \text{ keV} \\ R_2 & : 10 \text{ keV} \leq E_{\text{recoil}} \leq 100 \text{ keV}, \end{aligned} \quad (3.17)$$

and subsequently constructing an interpolating function,  $R'(E)$ . This interpolating function

is then integrated over the ranges in equation (3.17)

$$R^i = \int_{E_{\min}^i}^{E_{\max}^i} R'(E)dE, \quad (3.18)$$

depending on the target type ( $i = \text{Ge}$  or  $\text{Xe}$ ), thereby determining a value for  $R$  in units of events/(kg×day).

### 3.3 Indirect detection

Indirect detection of relic neutralinos involves detecting byproducts of neutralino pair annihilation in the galactic center, or even in the center of the earth and sun. These byproducts come in various forms: gamma rays, neutrinos, and anti-matter such as positrons and anti-protons. Fluxes of the various types of byproducts are proportional to the pair annihilation rate of relic neutralinos. This rate is proportional to the square of the density of relic neutralinos ( $\text{flux} \propto \Gamma \propto \rho_{\tilde{\chi}}^2$ ) and depending on the type of byproduct being searched for different locations offer better prospects for discovery.

#### Gamma Rays

Cosmic gamma rays from neutralino pair annihilation offer a unique signal in that they travel largely unimpeded from their source as they are not influenced by galactic magnetic fields. The best place to look for these byproducts are regions of the sky where a high density of neutralinos is expected, such as the galactic center of the Milky Way. There are essentially two types of gamma ray photons which can result as byproducts: those resulting from decay chains (hadronic decays leading to neutral pions which decay to 2 photons for example) and those produced directly from 1-loop neutralino decays. At the 1-loop level the following can occur  $\chi\chi \rightarrow \gamma\gamma, \gamma Z$  and these photons have energies which are monochromatic, whereas the photons produced from decay chains have a continuous spectrum of possible energies. The monochromatic line signals occur at energies of  $E_{\gamma} = m_x$  ( $\chi\chi \rightarrow \gamma\gamma$ ) or

$E_\gamma = m_\chi - m_Z^2/4m_\chi^2$  ( $\chi\chi \rightarrow \gamma Z$ ). The continuous photons are more difficult to separate from astrophysical backgrounds, while the monochromatic signals are easier to distinguish from the background. However the rate of production of monochromatic photons is much lower than the rate of production for the continuous photons.

As in the previous section, this discussion centers on how to compute the rate of photons expected for a given SUSY model. The discussion will be similar here and we first start by considering the differential rate of photon flux per photon energy  $E_\gamma$  expected at the Earth

$$\frac{d\Phi_\gamma}{dE_\gamma} = \sum_i \frac{\langle \sigma_i v \rangle}{4\pi m_\chi^2} \frac{dN_\gamma^i}{dE_\gamma} \int_{\text{line of sight}} ds(\psi) \rho_\chi^2(r), \quad (3.19)$$

with the sum over all possible final states,  $\sigma_i$  is the annihilation cross section into final state  $i$  and  $dN_i/dE_\gamma$  is the differential spectrum of photons produced in the decay channel from the state  $i$ . The integration is over the assumed dark matter halo profile for the region of space considered, which will be taken as the galactic center.

One method used to determine the form of the dark matter profile uses N-body simulations of galactic structure formation. Recent simulations suggest the existence of a universal profile of dark matter [71] which is typically written in the form

$$\rho_\chi(r) = (\rho_\chi)_0 \frac{(r/r_0)^{-\gamma}}{[1 + (r/a)^\alpha]^{\frac{\beta-\gamma}{\alpha}}} \left[ 1 + \left( \frac{r_0}{a} \right)^\alpha \right]^{\frac{\beta-\gamma}{\alpha}}, \quad (3.20)$$

where  $r_0$  is roughly the distance from the galactic center to the earth and  $(\rho_\chi)_0 = 0.3$  GeV/cm<sup>3</sup>, which may be subjected to rescaling as in equation (3.10). The dimensionful parameter  $a$  is related to the core radius of the halo. Some of the more common choices for the parameters  $(a, r_0, \alpha, \beta, \gamma)$  are given in Table 3.1. The various profiles listed are the Navarro, Frenk and White profile (NFW) [71, 72], a modified version of the NFW profile which includes the effect of baryons, a so-called ‘‘adiabatic compression’’ (NFW+AC) [73, 74] and a singular profile by Moore [75] which also includes the adiabatic compression. It is also useful to separate the dependence of the halo profile from the SUSY dependence in the

Model	$r_0$ (kpc)	$a$ (kpc)	$\alpha$	$\beta$	$\gamma$	$\bar{J}(10^{-5} \text{ sr})$
NFW	8.0	20.0	1	3	1	$1.2644 \times 10^4$
NFW + AC	8.0	20.0	0.8	2.7	1.45	$1.0237 \times 10^6$
Moore + AC	8.0	28.0	0.8	2.7	1.65	$3.0896 \times 10^8$

Table 3.1: **Halo model parameters.** The parameters which define the three halo models we will consider in this work and the resulting value of the parameter  $\bar{J}(\Delta\Omega)$  for  $\Delta\Omega = 10^{-5}$  sr.

differential flux of equation (3.19) by constructing the parameter  $J(\psi)$  as

$$J(\psi) = \frac{1}{8.5 \text{ kpc}} \left( \frac{1}{0.3 \text{ GeV cm}^3} \right)^2 \int_{\text{line of sight}} ds(\psi) \rho_\chi^2(r). \quad (3.21)$$

In equation (3.21)  $s(\psi)$  is a parameter that runs along the line of sight at an angle  $\psi$  from the direction of the galactic center (when looking at the galactic center  $\psi = 0$ ). The value of  $J(\psi)$  is usually averaged over a region of spherical angle  $\Delta\Omega$  (e.g. the finite resolution of a detector) centered on  $\psi = 0$  and is written as

$$\langle J(\psi) \rangle_{\Delta\Omega} = \frac{1}{\Delta\Omega} \int_{\Delta\Omega} d\Omega' J(\psi'). \quad (3.22)$$

The quantity in equation (3.22) is useful for comparing computed rates with different halo profiles and the values for the profiles considered here are also listed in Table 3.1. Note the orders of magnitude differences depending on the assumed profile.

Upon separating  $\bar{J}(\Delta\Omega)$  from equation (3.19) one obtains the following form for the differential photon flux in units of photons/(cm<sup>2</sup> s GeV)

$$\frac{d\Phi_\gamma}{dE_\gamma} = 0.94 \times 10^{-13} \sum_i \frac{dN_\gamma^i}{dE_\gamma} \left( \frac{\langle \sigma_i v \rangle}{10^{-29} \text{ cm}^3 \text{ s}^{-1}} \right) \left( \frac{100 \text{ GeV}}{m_\chi} \right)^2 \bar{J}(\Delta\Omega) \Delta\Omega. \quad (3.23)$$

The SUSY model dependence is contained in  $\frac{dN_\gamma^i}{dE_\gamma} \langle \sigma_i v \rangle$  (as well as the LSP mass  $m_\chi$ ). DarkSUSY is used for the calculations of the gamma flux and the method of determining  $\frac{dN_\gamma^i}{dE_\gamma} \langle \sigma_i v \rangle$  is discussed on pages 15 and 19 in [58]. Essentially eight main annihilation chan-

nels are considered:  $c\bar{c}$ ,  $b\bar{b}$ ,  $t\bar{t}$ ,  $gg$ ,  $ZZ$ ,  $W^+W^-$ ,  $\mu^+\mu^-$  and  $\tau^+\tau^-$  which are then hadronized and/or decayed using PYTHIA 6.154 [76]. The yields of different particles per neutralino annihilation are computed for 18 values of  $m_\chi$  with the results then tabulated and interpolated.

To compute the expected flux of gamma ray photons a similar approach is taken as in the case of direct detection. An energy range relevant to an experiment is considered and an interpolating function is created which is then integrated from some threshold  $E_{\min}$  to  $E_{\max}$  (the smaller of  $m_\chi$  or the upper limit of the experiment energy resolution) thereby determining the gamma ray photon flux at Earth for a given SUSY model. To create the interpolating function a step size of 1 GeV is used. Also note that for the monochromatic cases  $\chi\chi \rightarrow \gamma\gamma, \gamma Z$  no integration is necessary as  $dN_\gamma^i/dE_\gamma = 2$  and 1 for these two cases, respectively. To compute the rate one also assumes the halo profile and occasionally results will be written in the form  $\Phi_\gamma/\bar{J}$  so as to remain neutral as to the choice of profile.

## Anti-matter

Pair annihilation of neutralinos can also result in anti-matter such as positrons or anti-protons. These objects do not travel in a straight line to earth, rather the entire galactic halo can contribute to the flux of these objects at Earth. As these charged objects travel through the galaxy they interact with the galactic magnetic fields, essentially traveling along a random walk, all the while losing energy to inverse Compton scattering and synchrotron processes. This process is modeled via a diffusion equation which contains parameters which are constrained from the analysis of stable nuclei in cosmic rays (see [77] and references therein).

Not as much focus here will be given to anti-matter signals and the recent PAMELA signal [78], although some meaningful properties of SUSY models and their relation to the positron excess can be discussed without fully trying to fit the data. For example, the  $\sigma_{WW}$  cross section and how a mostly wino LSP can give a large enough  $WW$  cross section to fit the PAMELA data fairly well. Also boost factors are often mentioned and may be necessary

to fit the PAMELA signal (see for example [79] and references therein).

## **Muons**

Neutralinos can also become gravitationally trapped at the center of celestial objects where annihilation rates will dramatically increase. Gamma ray byproducts generally cannot escape from such objects, but neutrinos can and therefore offer a way to study neutralino annihilation nearby in the sun or earth. Typically the prospects for discovery are much greater by looking at the sun as many more neutralinos can become gravitationally trapped in the sun compared to the earth. In SUSY no tree level diagrams exist for  $\chi\chi \rightarrow \nu\bar{\nu}$ , rather the neutrinos arise via decays of heavy quarks, gauge bosons,  $\tau$ 's and Higgs states.

Neutrinos which come from neutralino annihilation in the sun can be detected at neutrino telescopes such as IceCube [80]. These neutrino telescopes typically operate well underground to reduce backgrounds and detect neutrinos by observing their muon tracks which are produced by charged current interactions in or near the detector. The rate of conversion muons from neutrino annihilation in the sun may be computed and used to predict expected rates at IceCube, for example, once a SUSY model is specified.

# Chapter 4

## Dark matter signals in deflected mirage mediation

Recently a string motivated scenario called deflected mirage mediation (DMM) has been proposed in which the three main SUSY breaking mediation mechanisms all contribute to the soft terms [81, 82, 83, 84]. This framework offers a rich model context with which to study gaugino masses and the resulting dark matter signals which arise. Although the model is string-inspired and will require some background discussion, the main interest will be on the gaugino masses of the theory and the associated dark matter signals of the lightest neutralino. This serves as a good starting point to the discussion of neutralino dark matter and many of the signals which will be discussed in later chapters. The analysis given follows the work done in [85].

### 4.1 DMM parameter space

DMM models are generalizations of mirage mediation models [86, 87, 88] of which models of the type introduced by Kachru, Kallosh, Linde and Trivedi (KKLT) [89] are an example. Mirage mediation is essentially the result of two independent mass contributions to the soft masses at a high scale, typically taken as the GUT scale  $Q_{\text{GUT}} = 2 \times 10^{16}$  GeV. The mass contributions are from a universal piece as well as a term proportional to the beta function coefficients  $b_a = (33/5, 1, -3)$ . The gaugino masses in mirage mediation are discussed in more detail in Section 6.1.

The model of KKLT is based on flux compactification of Type IIB string theory in

which the stabilization of the moduli fields is addressed while simultaneously obtaining a cosmologically stable vacuum. As can be seen from equation (2.13) the scalar potential can give a negative ground state, e.g. an anti-de Sitter (AdS) vacuum. To counter this problem and obtain a phenomenologically viable positive ground state, or de Sitter (dS) vacuum, KKLT add an uplifting potential which results in a positive value of the vacuum energy [89].

Here we focus on the gaugino sector of the theory and the subsequent dark matter signals which arise. The model contains three different contributions to the soft SUSY masses in the MSSM. The contribution from Planck-suppressed operators is universal and of the form  $M_0$ . The superconformal anomaly contributions will be proportional to a scale  $m_{3/2}$  and the gauge mediated contributions are proportional to a third mass scale  $\Lambda_{\text{mess}}$ . The framework for the DMM model is considered at the 1-loop level so that the full expressions for the gaugino masses may be explored as one evolves them from high scale to the weak scale. In this way the soft gaugino masses can be studied in a model-independent manner.

Taking the high scale to be  $Q_{\text{GUT}}$  the gaugino masses receive contributions from both  $M_0$  and  $m_{3/2}$ . At a lower scale,  $Q_{\text{mess}} < Q_{\text{GUT}}$ , the messenger fields are integrated out and give contributions to the soft gaugino masses proportional to  $\Lambda_{\text{mess}}$ . The field content of the model is the usual MSSM particle content in addition to the messenger sector. The messenger sector is taken to be in complete GUT representations of the Standard Model so as to preserve the gauge coupling unification of the MSSM at  $Q_{\text{GUT}}$ . Specifically we take  $N_m$  gauge charged messengers so that the beta functions of the MSSM above  $Q_{\text{mess}}$  have the form  $b'_a = b_a + N_m$  and the gauge couplings at the GUT scale have the form  $1/g_a^2(Q_{\text{GUT}}) = 1/g_{\text{GUT}}^2 - N_m \ln(Q_{\text{GUT}}/Q_{\text{mess}})$  with  $g_{\text{GUT}}^2 \simeq 1/2$ .

The gaugino masses at the GUT scale take the form

$$M_a(Q_{\text{GUT}}) = M_0 + g_a^2(Q_{\text{GUT}}) \frac{b'_a}{16\pi^2} m_{3/2}. \quad (4.1)$$

At the 1-loop level this expression is evolved to the intermediate scale  $Q_{\text{mess}}$  where the

messengers are integrated out resulting in an effective threshold contribution to the gaugino masses of the form

$$\Delta M_a = -N_m \frac{g_a^2(Q_{\text{mess}})}{16\pi^2} (\Lambda_{\text{mess}} + m_{3/2}) . \quad (4.2)$$

At this point it is convenient to exchange the three mass contributions to the soft terms for one mass term and two dimensionless ratios. This parameterization uses the universal mass term  $M_0$  along with

$$\alpha_g \equiv \frac{\Lambda_{\text{mess}}}{m_{3/2}} \quad \text{and} \quad \alpha_m \equiv \frac{m_{3/2}}{M_0 \ln(M_{\text{Pl}}/m_{3/2})} , \quad (4.3)$$

where  $M_{\text{Pl}} = 2.4 \times 10^{18}$  GeV is the reduced Planck mass. The definition of  $\alpha_m$  is useful as it gives a ratio of order 1 and is the natural parameter from the point of view of the mirage mediation model. Further, following Choi [84] it is useful to introduce additional dimensionless ratios

$$x = \frac{1}{R + \alpha_m} \quad \text{and} \quad y = \frac{\alpha_m}{R + \alpha_m} \quad (4.4)$$

where  $R$  is given by

$$R = 1 - \frac{N_m g_{\text{GUT}}^2}{8\pi^2} \left\{ \frac{\alpha_m \alpha_g}{2} \ln\left(\frac{M_{\text{Pl}}}{m_{3/2}}\right) + \ln\left(\frac{Q_{\text{GUT}}}{Q_{\text{mess}}}\right) \right\} . \quad (4.5)$$

Upon running down the gaugino masses given in equation (4.1) and adding the threshold correction in equation (4.2) the gaugino masses at the low scale  $Q < Q_{\text{mess}}$  are given by the expression

$$M_a(Q) = M_0 \frac{1 + \beta_a(Q)t}{x} \left\{ 1 + y \left[ \frac{\beta_a(Q)t'}{1 + \beta_a(Q)t} - 1 \right] \right\} , \quad (4.6)$$

where we have defined two scaling variables  $t$  and  $t'$  via

$$t = \ln\left(\frac{Q}{Q_{\text{GUT}}}\right) \quad \text{and} \quad t' = \frac{1}{2} \ln\left(\frac{M_{\text{Pl}}}{m_{3/2}}\right) . \quad (4.7)$$

To continue and discuss the properties of the gaugino sector relevant for dark matter

observations we need to include a full model framework. This needs to be done as the gaugino sector depends on other parameters in equations (2.35) and (2.36), most notably the supersymmetric Higgs mass  $\mu$ , which is determined via the electroweak symmetry breaking conditions. Upon specifying the remaining soft terms the value of  $\mu$  can be determined and thus the gaugino sector will be fully defined allowing the investigation of the dark matter properties. Moving forward we follow the work of [82, 84] to define the remaining soft terms and trilinear couplings. The full model framework is Type IIB string theory compactified on a Calabi-Yau orientifold with flux added in the manner of KKLT. The model framework assumes a Kähler potential of the form

$$K = \sum_i (T + \bar{T})^{-n_i} \bar{\Phi}_i \Phi_i, \quad (4.8)$$

where  $T$  denotes the chiral Kähler modulus superfield whose VEV generates the universal contribution to the gaugino masses (assuming universal gauge kinetic functions  $f_a = T$ ) as

$$M_0 = \left\langle \frac{F_T}{t + \bar{t}} \right\rangle, \quad (4.9)$$

where  $t = T|_{\theta=0}$  is the scalar component of the superfield  $T$ . The values  $n_i$  in equation (4.8) are the modular weights for the matter superfield  $\Phi_i$  and they depend on the location of the matter fields, e.g. the fixed points of the compactification manifold. Following other previous works in [90] and [91] it has been argued that for models of this type the values of  $n_i$  can have values of 0, 1/2 or 1.

The order parameter in equation (4.9) will generate the remaining soft terms and trilinear couplings at the high scale. As in the case of the soft gaugino masses the soft scalar masses and trilinear couplings will also receive contributions at the high scale from the anomaly mediation proportional to  $m_{3/2}$ . The high scale soft terms are given by [82]

$$A_{ijk}(Q_{\text{GUT}}) = M_0 \left[ (3 - n_i - n_j - n_k) - \frac{(\gamma_i + \gamma_j + \gamma_k)}{16\pi^2} \alpha_m \ln \left( \frac{M_{\text{Pl}}}{m_{3/2}} \right) \right] \quad (4.10)$$

$$m_i^2(Q_{\text{GUT}}) = M_0^2 \left[ (1 - n_i) - \frac{\theta'_i}{16\pi^2} \alpha_m \ln \left( \frac{M_{\text{Pl}}}{m_{3/2}} \right) - \frac{\dot{\gamma}'_i}{(16\pi^2)^2} \left( \alpha_m \ln \left( \frac{M_{\text{Pl}}}{m_{3/2}} \right) \right)^2 \right],$$

where  $\alpha_m$  is defined in equation (4.3) and the terms  $\gamma_i$ ,  $\theta'_i$  and  $\dot{\gamma}'_i$  are functions of the beta functions, SM gauge and Yukawa couplings and their expressions are given in [82]. The primes on these indicate that the parameters take into account the presence of the messenger sector. As in the case of the soft gaugino masses these expressions are evolved to the scale  $Q_{\text{mess}}$  where integrating out the messenger fields results in threshold corrections to the soft scalar masses of the form

$$\Delta m_i^2 = M_0^2 \sum_a (2N_m C_a) \frac{g_a^4(Q_{\text{mess}})}{(16\pi^2)^2} \left[ \alpha_m (1 + \alpha_g) \ln \left( \frac{M_{\text{Pl}}}{m_{3/2}} \right) \right]^2, \quad (4.11)$$

where  $C_a$  are the quadratic Casimir operators for the gauge groups  $\mathcal{G}_a$  in the adjoint representation. The trilinear couplings receive no such correction since in gauge mediation the contributions to the trilinears are non-zero only at the two-loop order and are highly suppressed, so to a good approximation they receive no contribution from the gauge messengers. Once the threshold corrections to the soft terms have been included the terms are further evolved down to the low scale  $Q < Q_{\text{mess}}$  where the soft terms are then passed to **SuSpect** 2.4 [92] to compute the physical masses and determine the values of  $m_A$  and  $\mu$  via the EWSB conditions.

To investigate the DMM model and its properties relevant to dark matter we will consider the parameter space defined by the set  $\{M_0, x, y\}$  by setting  $M_0$  fixed at certain values so as to look at slices in the  $xy$  plane. For this we will hold fixed  $\tan \beta = 10$ ,  $Q_{\text{mess}} = 10^{10}$  GeV,  $N_m = 3$  and use the following values for the modular weights of the matter fields in the MSSM

$$\{n_Q, n_U, n_D, n_L, n_E, n_{H_u}, n_{H_d}\} = \{1/2, 1/2, 1/2, 1/2, 1/2, 1, 1\}. \quad (4.12)$$

Choosing the modular weights in equation (4.12) was done so as to match specific benchmark

models from the literature. The parameter choices just described make up the “model-dependent” scenario.

Initial scans over the parameter space in the model-dependent scenario are performed for values  $M_0 = 250, 500, 1000$  and  $2000$  TeV. These scans are analyzed so as to contain the points of interest where the spectra are physically allowed, EWSB is consistent and the LSP is the lightest neutralino. For  $xy$  scans the primary constraints come from the mass bounds on the gauginos. Relevant bounds concerning the lightest neutralino and chargino are  $m_{\tilde{N}_1} \geq 46$  GeV and  $m_{\tilde{N}_1} \geq 103$  GeV [23]. For the gluino, the mass bounds are model dependent and to remain conservative a lower bound of  $m_{\tilde{g}} \geq 200$  GeV [93] is used, although a bound of  $m_{\tilde{g}} \geq 300$  GeV is the typical limit [94].

In Figure 4.1 the allowed regions of parameter space are shown in the  $xy$  plane for the various choices of  $M_0$ . Regions that are lightly shaded are ruled out by the direct search limits on  $\tilde{N}_1$ ,  $\tilde{C}_1$  and  $\tilde{g}$  masses. Further the blue shaded region contains points where for this choice of modular weights the  $\tilde{\tau}_1$  is the LSP for small  $x$  and  $y$ . The hatched regions near  $x = 0.4, y = 0.6$  are regions where the  $\tilde{t}_1$  is the LSP. The upper left hand corners do not break electroweak symmetry and the conditions give a tachyonic pseudo-scalar Higgs,  $m_A^2 < 0$ . In the figures which follow these regions will not be considered due to the above considerations.

As previously mentioned the  $(x, y)$  plane is convenient as the various limits of the theory can be reached. This is demonstrated in Figure 4.1 where certain limits are sketched. Points in the  $(x, y)$  plane which have  $R = 0$  are on the line where  $x + y = 1$ , while points with on the line  $y = x$  have  $\alpha_m = 1$  for arbitrary  $\alpha_g$ . The intersection of these two lines is the simplest prediction of the KKLT framework which inspired the mirage mediation scenario, and so we mark this in the figure. The gauge-mediation limit of the theory is formally the origin in the  $(x, y)$  plane where  $R^{-1} \rightarrow 1$  while keeping  $RM_0$  finite, so this limit cannot be reached in the figure. The pure anomaly-mediated limit of  $(0, 1)$  can also not be reached as this is where  $\alpha_m \rightarrow \infty$  with  $\alpha_m M_0$  held fixed. The pure modulus (or gravity) mediation

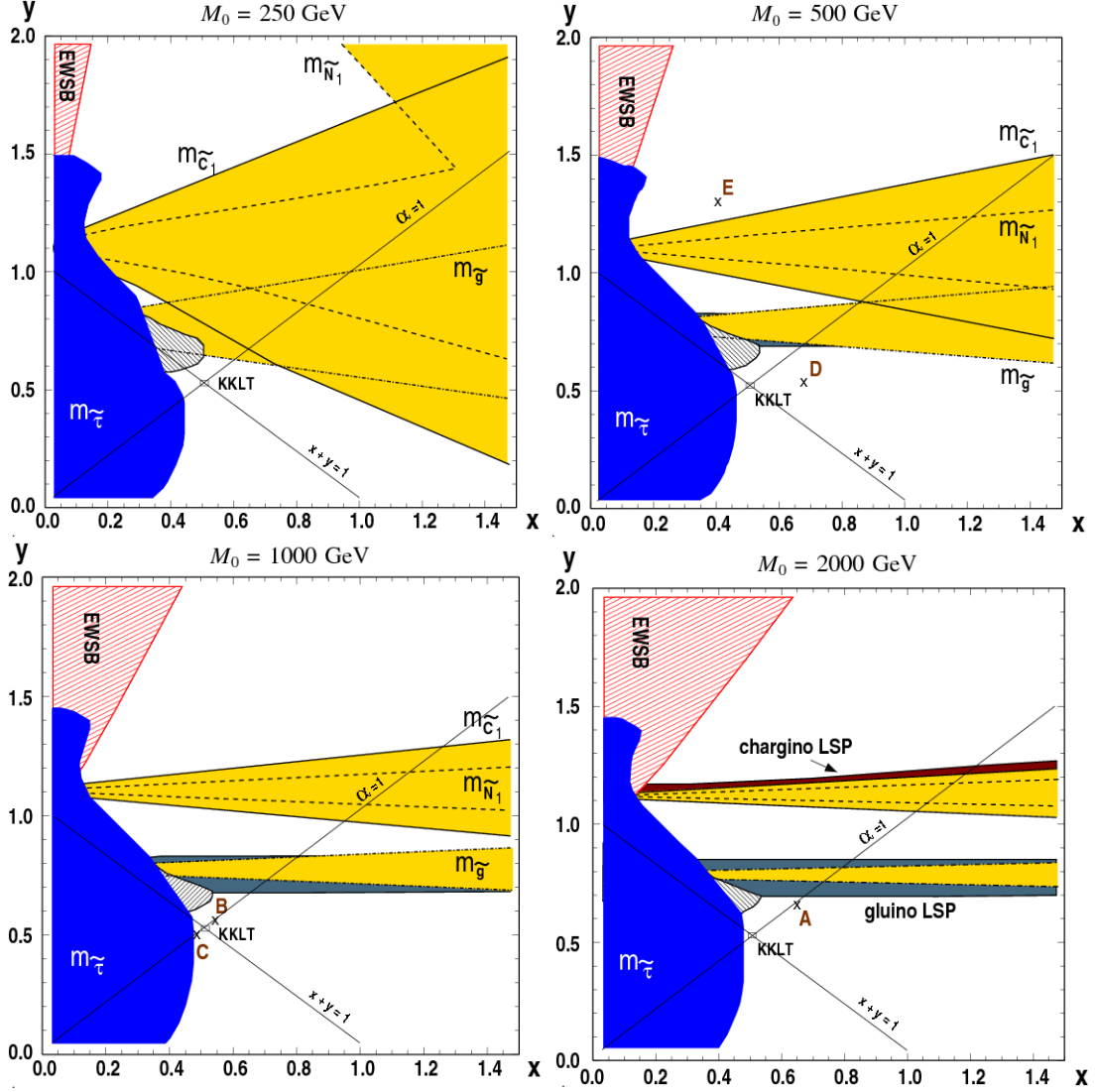


Figure 4.1: **Allowed Parameter Space for the “Model-Dependent Scenario.”** Contours indicate the lower bounds used on the sparticle masses with  $m_{\tilde{N}_1} = 46$  GeV (dashed contour),  $m_{\tilde{C}_1} = 103$  GeV (solid contour) and  $m_{\tilde{g}} = 200$  GeV (dash-dotted contour). The dark shaded region in the lower left corner is the area in which the stau is the LSP, while the smaller hatched region in the center has a stop LSP for the modular weight choice of equation (4.12). The hatched region in the upper left of each plot indicates where no EWSB occurs. For larger values of the parameter  $M_0$  we have indicated the area in which the gluino (or the chargino) is the LSP by the darker shaded region(s). The labeled points are the benchmark models of Table 4.1. The intersecting lines indicate those points for which  $\alpha_m = 1$  (lower left to upper right) and where  $R = 0$  (upper left to lower right). The intersection of these two curves designates the prediction of the simplest KKLT scenario.

	Model A	Model B	Model C	Model D	Model E	Model F
$M_0$	2000 GeV	1000 GeV	1000 GeV	500 GeV	500 GeV	933 GeV
$m_{3/2}$	62.6 TeV	32.0 TeV	32.0 TeV	13.2 TeV	51.3 TeV	31.7 TeV
$\mu_{\text{mess}}$	$10^{12}$ GeV	$10^8$ GeV	$10^{12}$ GeV	$10^{10}$ GeV	$10^{10}$ GeV	N/A
$\alpha_m$	1	1	1	0.81	3.26	1
$\alpha_g$	1	-1/2	-1	0.14	1.47	0
$N_m$	3	3	3	3	3	0
$x$	0.668	0.561	0.472	0.674	0.401	0.5
$y$	0.668	0.561	0.472	0.543	1.307	0.5

Table 4.1: **Benchmark Models.** The relevant mass scales are given in the first three entries, with the parameters of Everett et al. in the second block. The final block re-casts these parameters in terms of the parameterizations of Choi et al. from (4.4). All models are defined with positive value of  $\mu$  and  $\tan\beta = 10$ . Models A-B were considered in [81] while Model C was considered in [82]. Model F is a mirage model without messengers near the prediction for the basic KKLТ model.

limit can be reached and is the point (1, 0). It is also worth marking a few points in the figures where certain benchmarks will be singled out for further study later. The parameter values for the benchmark choice are given in Table 4.1.

The two cases  $M_0 = 500$  and 1000 TeV will be highlighted further for the various dark matter observables and therefore we focus on the LSP properties for these mass choices in the  $(x, y)$  plane as shown in Figure 4.2. Regions which are ruled out are in yellow (light shading) and correspond to the marked regions in Figure 4.1. The LSP mass contours are labeled with appropriate masses and the kinks are due to level crossings where the LSP goes from mostly bino to mostly wino, e.g. where the  $M_1$  and  $M_2$  hierarchy flips from  $M_1 < M_2$  to  $M_2 < M_1$ . Regions where the LSP is mostly Bino-like (over 95%) are marked along with where the LSP is mostly wino (over 95%). In the lower mass case of  $M_0 = 500$  GeV the hatched region is where the LSP has sizable Higgsino content (from 10% up to 50%), while this region is not allowed in the higher mass case.

In Figure 4.3 a zoomed region from 0 to 1 in both  $x$  and  $y$  is shown for various other superpartner masses shown only for  $M_0 = 500$  and 1000 GeV. As in Figure 4.2 the yellow (light shaded) region is not allowed. The upper panel of the figure shows mass contours for

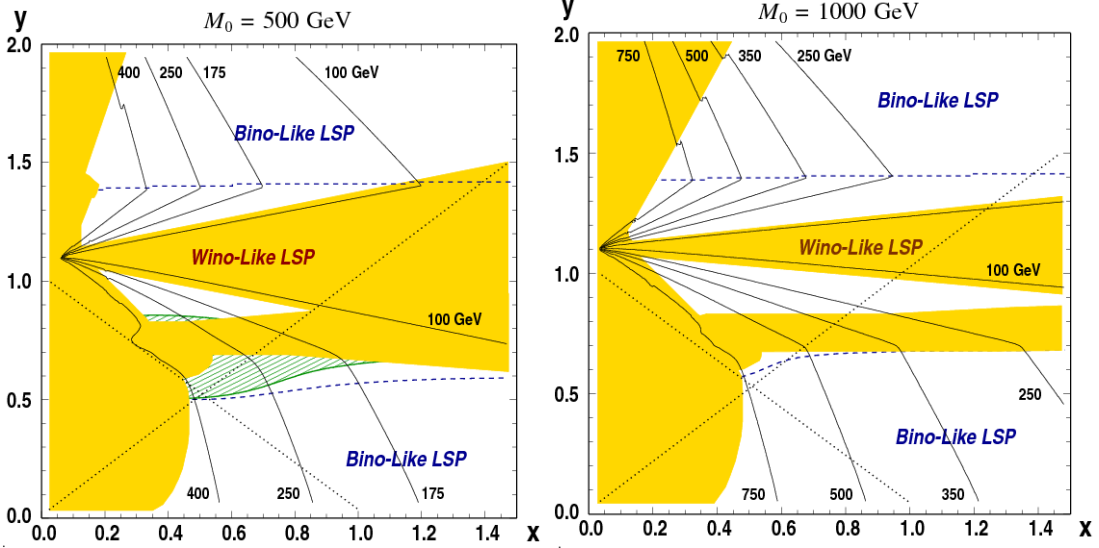


Figure 4.2: **LSP Properties for the “Model-Dependent Scenario.”** Contours of constant LSP mass  $m_{\tilde{N}_1}$  are given for the scenario with modular weights of equation (4.12) for mass scale  $M_0 = 500$  GeV (left panel) and  $M_0 = 1000$  GeV (right panel). The lightly shaded region is ruled out for the reasons indicated in Figure 4.1. For both values of  $M_0$  the LSP is primarily bino-like for  $y \lesssim 0.6$  and  $y \gtrsim 1.4$ . For the case of  $M_0 = 500$  GeV there is also some parameter space where the LSP is a mixture of Higgsino and wino, indicated by the hatched region.

the gluino (solid lines) and the light chargino (dashed) along with a curved shaded region where  $1.5 \leq m_A/m_{\tilde{N}_1} \leq 2.5$ . In the region where  $m_A \simeq 2m_{\tilde{N}_1}$  the LSP undergoes the very efficient resonant annihilation with the pseudoscalar-Higgs, thus depleting the thermal abundance of relic neutralinos. In the lower panel of the figure we take  $N_m = 0$  and plot the masses as a function of  $x$  as in this case the models are pure mirage mediation. The phenomenology of the mirage models roughly corresponds to that of the  $(x, y)$  plane where  $x + y = 1$  and this can be seen in the figure. Note that the correspondence is not exact as in the upper panels we have  $N_m \neq 0$ , and the line  $x + y = 1$  gives a solution for which the quantity in braces in equation (6.10) equation vanishes meaning that  $\alpha_g$  is non-zero. However the phenomenology of the models is similar and so the line  $x + y = 1$  can be used as a reasonable comparison for a mirage model.

It is important to note that the modular weight choices made in the model-dependent

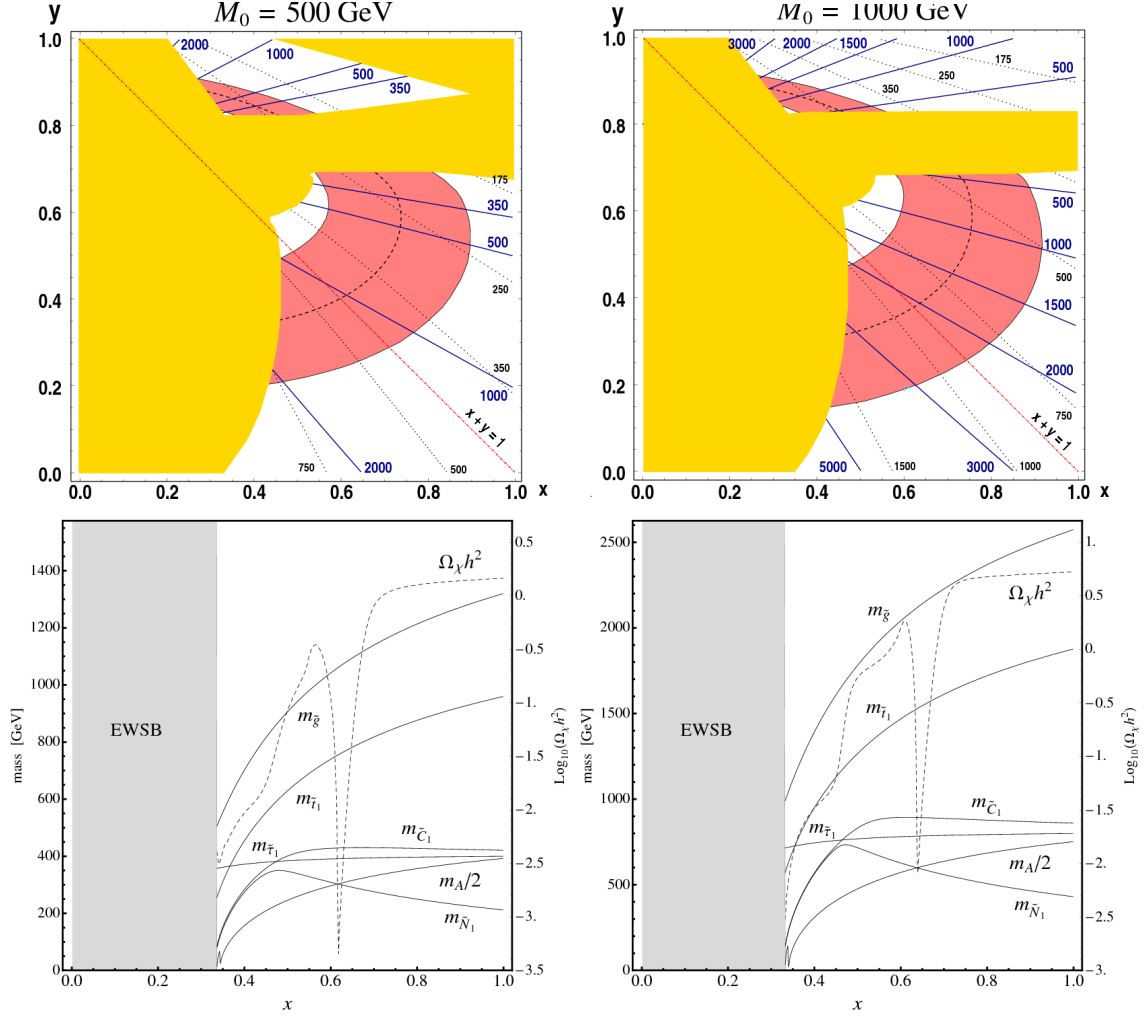


Figure 4.3: **Key Superpartner Masses for the “Model-Dependent Scenario.”** Upper panels give various masses for the  $\{x, y\}$  plane, while the lower panels plot masses along the line  $x + y = 1$  with  $N_m = 0$ . Panels on the left take  $M_0 = 500$  GeV while those on the right take  $M_0 = 1000$  GeV. The lightly shaded region in all plots is phenomenologically forbidden. The darker shaded region in the upper plots shows the area where  $1.5 \leq m_A/m_{\tilde{N}_1} \leq 2.5$ , with  $m_A = 2m_{\tilde{N}_1}$  given by the curved dashed line. In the upper plot heavy solid lines are contours of constant  $m_{\tilde{g}}$  while dashed lines are contours of constant  $m_{\tilde{C}_1}$ . All masses are in GeV.

scenario can have  $\mathcal{O}(1)$  effects on the high scale inputs in the theory as can be seen in equation (4.10). Choosing different values for the modular weights will result in different values in the low scale physical masses which in turn affects the derived value of the  $\mu$  parameter upon imposing EWSB conditions. The allowed parameter space shown for the model dependent scenario is dependent on the choices of modular weights as discussed in [95, 96, 97]. Therefore also investigated is a “model independent” scenario in which model properties are considered using low scale gaugino masses as in equation (4.6) along with just fixing at the low scale  $\mu = m_A = 1$  TeV with all other soft scalar masses set to  $\text{Max}(M_3, 1 \text{ TeV})$ . In Figure 4.4 we show allowed regions in the  $(x, y)$  plane for  $M_0 = 500$  and  $1000$  GeV. The dotted line is the contour where  $m_{\tilde{N}_1} = 1$  TeV and where a scalar particle in this case would become the LSP. That this happens is due to the gauginos becoming very massive as  $x \rightarrow 0$ . As the gluino becomes more massive it induces large radiative corrections to the Higgs potential and as a result a light Higgs mass results in the upper left corner where  $m_h \leq 100$  GeV and in the lower left corner  $m_A^2 < 0$ .

## 4.2 Survey of DM signatures

Now that the basic properties of the model have been discussed we move on to consider various dark matter signatures of the DMM model. To start the thermal relic density is considered followed by the direct and indirect detection prospects. For all calculations the physical mass spectrum is computed using `Suspect 2.4` and then passed to `DarkSUSY 5.0.4` [58] for calculation of the relic density along with the dark matter observables.

### 4.2.1 Relic density

In what follows the analysis is based on the scans in the  $(x, y)$  plane using the two values of  $M_0 = 500$  and  $1000$  GeV whose properties are shown in Figures 4.1, 4.2 and 4.3. The

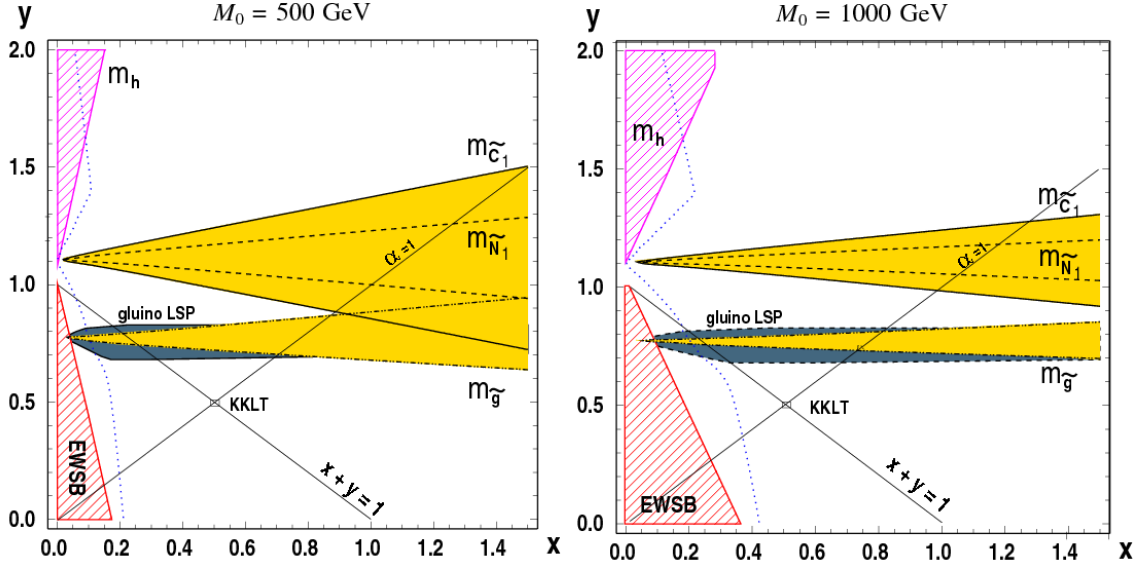


Figure 4.4: **Allowed Parameter Space for the “Model-Independent Scenario.”** Gaugino mass contours are the same as Figure 4.1. The darker shaded region is the area in which the gluino is the LSP. The dotted line on the left of each plot is the contour where  $m_{\tilde{N}_1} = 1$  TeV. The hatched region in the lower left of each plot indicates where  $m_A^2 < 0$  and no EWSB occurs for a value  $\mu = 1$  TeV. We have indicated the area in the upper left where  $m_h \leq 100$  GeV due to large radiative corrections.

WMAP three year data [98] at the  $2\sigma$  level is

$$0.0855 \leq \Omega_\chi h^2 \leq 0.1189, \quad (4.13)$$

In the figure a “WMAP” preferred range is shown for which

$$0.07 \leq \Omega_\chi h^2 \leq 0.14, \quad (4.14)$$

which is a bit easier to resolve than the value in equation (4.13). The thermal relic abundance in the  $(x, y)$  plane is shown in Figure 4.5 where the “WMAP preferred” region is indicated by the narrow red shaded region. Inside the parameter space with a wino-like LSP, and within the  $A$ -funnel region, the relic density drops below the value of  $\Omega_\chi h^2 = 0.025$ , indicated by the yellow shading. The intermediate regime of  $0.025 \leq \Omega_\chi h^2 \leq 0.07$  is indicated by blue

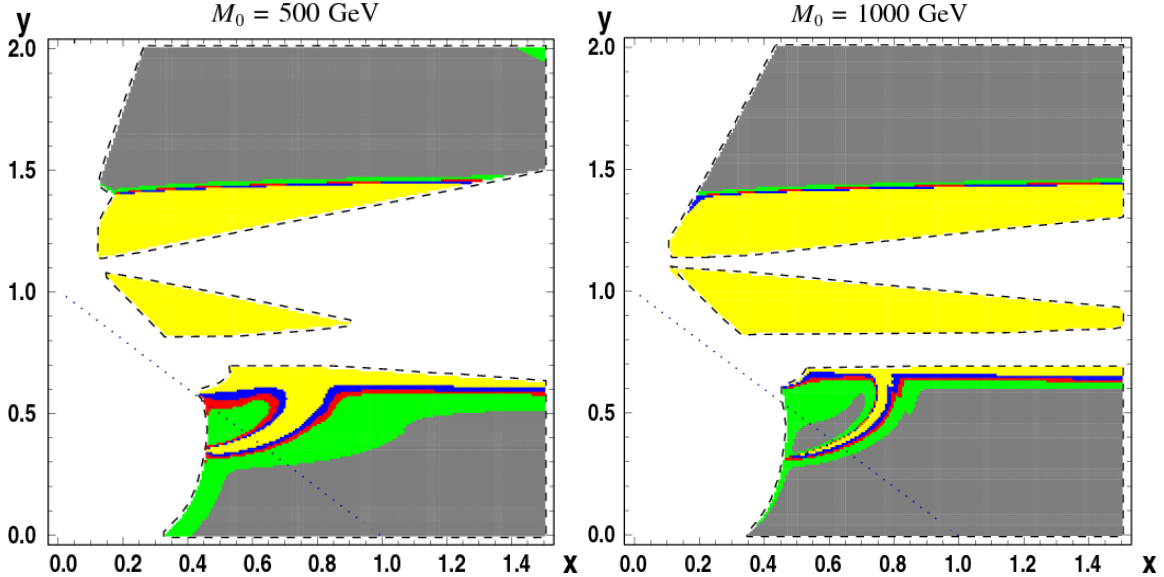


Figure 4.5: **Thermal Relic Density in Deflected Mirage Mediation.** Left panel takes  $M_0 = 500$  GeV, right panel takes  $M_0 = 1000$  GeV. The “WMAP preferred” region of  $0.07 \leq \Omega_\chi h^2 \leq 0.14$  of equation (4.13) is here indicated by the narrow red shaded region. For the wino-like LSP and within the  $A$ -funnel region the relic density drops below the critical value of  $\Omega_\chi h^2 = 0.025$ , indicated by the yellow (very light) shading. The remaining regions are  $0.025 \leq \Omega_\chi h^2 \leq 0.07$  (blue),  $0.14 \leq \Omega_\chi h^2 \leq 1$  (green) and  $\Omega_\chi h^2 > 1$  (gray).

shading. The green area in the plot has  $0.14 \leq \Omega_\chi h^2 \leq 1$  while the gray area has  $\Omega_\chi h^2 > 1$ . The transition from heavily wino-like LSP to heavily bino-like LSP occurs near  $y \simeq 1.4$  where the relic density rapidly changes from far too low to far too high. In between these extremes there exists a narrow region with  $\Omega_\chi h^2 \simeq 0.10$ .

As discussed in Section 3.1, the relic LSP need not account for all dark matter necessary to make up the WMAP measurement. In what follows we will remain neutral on this issue as the physics of the early universe is not the main focus of this analysis and we do not eliminate parameter space where the  $\Omega_\chi h^2$  is outside of the range in equation (7.4). Non-thermal mechanisms are well-motivated within string models such as the KKLТ framework [99, 100] and so may be applicable here. Too large a value of  $\Omega_\chi h^2$  is more difficult to address but mechanisms do exist which can lower the value to be closer in line to the WMAP results [101, 102, 103]. In the survey of detection experiments that follows we will rescale the assumed local density of  $\rho_\chi = 0.3$  GeV/cm<sup>3</sup> by the factor  $r_\chi = \text{Min}(1, \Omega_\chi h^2/0.025)$  from

equation (3.10). To negate the rescaling, one may estimate the necessary factor based on Figure 4.5.

## 4.2.2 Direct detection

First direct detection of the neutralino LSP will be considered. The method used will be to compute the rate of interaction with xenon and germanium targets as discussed in Chapter 3. The integration ranges will be  $R_{Xe} = R_1$ ,  $R_{Ge} = R_2$  as in equation (3.17). Here we focus on the predicted rates in current and future large scale experiments as listed in Table 4.2. For experiments that have already reported data the fiducial mass times given exposure time is used, while for future experiments the fiducial mass is taken as 80% of the nominal mass. One should also keep in mind the large uncertainties associated with the nuclear form factors when considering the rates. The rates computed here use the default values of the form factors as in DarkSUSY 5.0.4 (while similar rates computed in micrOMEGA's can be about twice as large).

Ref.	Experiment Name	Exposure [kg×yr]	$R_{10}$ [counts/(kg yr)]
[69]	XENON10	$5.4 \times 0.16$	11.54
[104]	XENON100	$170 \times 0.8 \times 1$	$7.35 \times 10^{-2}$
[105]	LUX	$350 \times 0.8 \times 3$	$1.19 \times 10^{-2}$
[104]	XENON1T	$1000 \times 0.8 \times 5$	$2.50 \times 10^{-3}$
[106]	CDMS II	$3.75 \times 0.29$	9.18
[107]	SuperCDMS (SNOLab)	$27 \times 0.8 \times 3$	0.15
[107]	SuperCDMS (DUSEL)	$1140 \times 0.8 \times 5$	$2.19 \times 10^{-3}$

Table 4.2: **Rate Estimates for Various Experiments.** The minimum threshold rate  $R_{10}$  necessary to produce 10 events in a given experiment for the fiducial mass and exposure time given is tabulated in the final column. Note that for Xenon10 and CDMS II we use the experimentally quoted fiducial masses. For all other (future) experiments we assume a fiducial mass equivalent to 80% of the nominal quoted target mass.

Bounds on the experiments considered here have been set by Xenon10 [69] and CDMS II [106] (although newer CDMS II [70] data have been reported as discussed below) with exposures of 316.4 kg×days and 397.8 kg×days, respectively. Expected backgrounds for

these two experiments were on the order of 10 events or less with backgrounds expected to be much lower at future installments. The rate to produce 10 events,  $R_{10}$  in units of counts/(kg  $\times$  yr), is considered for the given experiments using the exposure time listed in Table 4.2. Limits can be placed on a model by requiring  $R \leq R_{10}$  for a given experiment.

Model points in the  $(x, y)$  plane scans are grouped according to the potential visibility at the experiments considered as shown in Figure 4.6 for both target types. None of the model points considered here were found to be in disagreement with the upper bounds of  $R_{10}$  for the Xenon10 and CDMS II bounds considered in Table 4.2. The yellow (light shading) in all the plots means that the rates are too low to be seen in any of the experiments listed in Table 4.2. A decent amount of the parameter space becomes detectable at about the 100 kg $\times$ year level. This is indicated by the green (medium shading) in all the panels for  $11.54 > R_{10}^{\text{Xe}} \geq 0.0735$  counts/kg-yr and  $9.18 > R_{10}^{\text{Ge}} \geq 0.15$  counts/kg-yr for xenon and germanium targets, respectively. This level of exposure can be reached by the Xenon100 experiment after about 1 year and can be reached after about 4 years of exposure by SuperCDMS at SNOlab. Detection prospects are better for the larger installation xenon targets such as LUX after about 3 years of data taking can probe models in the red (dark shading) region for  $0.0735 > R_{10}^{\text{Xe}} \geq 0.0119$  counts/(kg  $\times$  yr). Regions which can be probed at about the 5 ton $\times$ year level using xenon are shown in blue with  $0.0119 > R_{10}^{\text{Xe}} \geq 0.0025$  counts/(kg  $\times$  yr). Using a germanium target the red region also shows models which can be probed at about the 5 ton $\times$ year level with  $0.15 > R_{10}^{\text{Ge}} \geq 0.00219$  counts/(kg  $\times$  yr). Recall also that the model points have been rescaled using  $r_\chi$ , and therefore would require less exposure to be probed if the rescaling is not enforced.

The various regions which arise from the rate calculations in the  $(x, y)$  plane are due to many factors. The rates depend on basic parameters like  $m_\chi$  and the target mass for example in a straightforward way in equation (3.12) and (3.15). However the couplings in equation (3.14) are more complicated functions of the LSP wavefunction, the scalar Higgs mixing angle and masses, and the squark masses and mixings. Regions with higher rates are

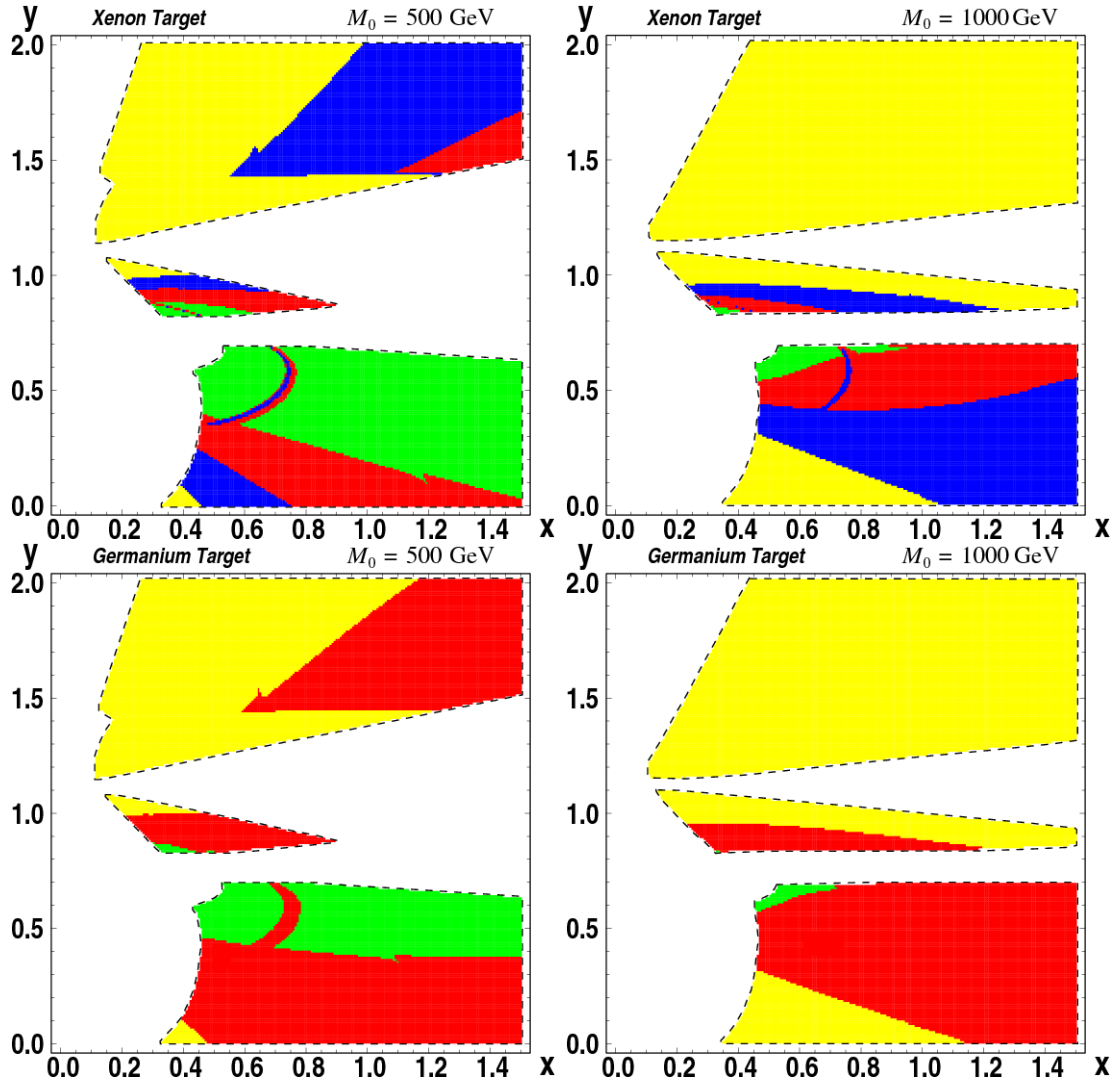


Figure 4.6: **Neutralino Recoil Rates on Xenon (top) and Germanium (bottom).** Left panels set  $M_0 = 500$  GeV, right panels set  $M_0 = 1000$  GeV. Phenomenologically allowed areas are enclosed by the heavy dashed lines. Colored shading indicates the reach of future direct detection experiments, as computed in Table 4.2. Yellow in all panels indicates parameter space that will be inaccessible to any of the future experiments in Table 4.2. For xenon targets, green indicates  $11.54 > R_{10}^{\text{Xe}} \geq 0.0735$ , red indicates  $0.0735 > R_{10}^{\text{Xe}} \geq 0.0119$  and blue indicates  $0.0119 > R_{10}^{\text{Xe}} \geq 0.0025$  in recoils per kg-year. For germanium targets, green indicates  $9.18 > R_{10}^{\text{Ge}} \geq 0.15$  and red indicates  $0.15 > R_{10}^{\text{Ge}} \geq 0.00219$  recoils per kg-year.

typical for a Higgsino-like LSP, and a mixed LSP can also achieve higher rates. The smaller rate regions can be attributed to Bino like LSPs which have the smallest interaction cross sections  $\sigma_{\chi p}^{\text{SI}}$  as well as other factors.

### 4.2.3 Gamma rays

Two types of gamma ray signals are considered here: diffuse and monochromatic. First the diffuse signals will be investigated using the Fermi/GLAST satellite as an experimental guide and later a generic air Cherenkov telescope (ACT) will be the guide for the monochromatic signals.

For the diffuse gamma ray signals we consider the Fermi/GLAST satellite [108] which has an effective area of about  $1 \text{ m}^2$  and an angular resolution of  $\Delta\Omega = 10^{-5}$  steradians. Typical energies are in the 10-100 GeV range and we integrate the differential photon flux in equation (3.23) over the range  $1 \text{ GeV} \leq E_\gamma \leq 200 \text{ GeV}$ . Note that the energy range of Fermi/GLAST is typically much lower than the masses of the neutralino LSPs which are considered. In order to discuss the prospects of signals from diffuse gamma rays one needs to assume a dark matter halo profile. Both the NFW and NFW+AC profiles will be considered here.

Furthermore the expected backgrounds need to be considered over the energy range relevant. For this the background estimation of [109] is used which gives a background flux of  $\Phi_{\text{bkgnd}} = 5.06 \times 10^{-10} \text{ photons/cm}^2/\text{sec}$  which is  $\mathcal{O}(100)$  photons/year for the aperture and energy range of Fermi/GLAST. This is in agreement with quoted sensitivity of the photon flux at Fermi/GLAST [108, 110]. The Fermi/GLAST experiment can also use the shape of the photon spectrum to enhance the signal extraction and the possibility may also exist that large background sources can be identified and subtracted to further increase the signal over background. Therefore a flux which can give 100 events in a given exposure will be considered as a potentially visible signal. The various exposures considered for this analysis are given in Table 4.3. Depending on the assumed halo profile the exposures result

Exposure [m <sup>2</sup> yr]	Halo Profile	$\Phi_{100}$ [counts/(cm <sup>2</sup> s)]
1	NFW	$5.79 \times 10^{-10}$
5	NFW	$1.16 \times 10^{-10}$
1	NFW+AC	$7.15 \times 10^{-12}$
5	NFW+AC	$1.43 \times 10^{-12}$

Table 4.3: **Reach Estimates in the Continuous Gamma Ray Flux for the Fermi/GLAST Experiment.** The quantity  $\Phi_{100}$  is the flux needed for 100 signal events at Fermi/GLAST assuming various exposure times and halo profiles.

in different values for the flux necessary to give 100 events,  $\Phi_{100}$ .

The resulting photon fluxes relevant to the Fermi/GLAST experiment are as shown in the  $(x, y)$  planes in Figure 4.7. In the framework under investigation and using the NFW or NFW+AC halo profiles the prospects for discovery are challenging using diffuse gamma rays. For the overall lower mass case of  $M_0 = 500$  GeV a few points (in red) near the  $A$ -funnel are potentially visible after 1 m<sup>2</sup>-yr of exposure using the NFW profile, e.g. have  $\Phi_{100} \geq 5.79 \times 10^{-10}$  counts/(m<sup>2</sup> × yr). The green shaded region is visible at the 5 m<sup>2</sup>-yr level assuming the NFW profile with  $5.79 \times 10^{-10} > \Phi_{100} \geq 1.16 \times 10^{-10}$  counts/(m<sup>2</sup> × yr). Upon assuming the NFW+AC profile the necessary flux to give 100 events after some exposure decreases by about a factor of 100 as this profile gives much larger signals. In the case of the NFW+AC profile the blue region denotes where points become visible after 1 m<sup>2</sup>-yr of exposure with  $1.16 \times 10^{-10} > \Phi_{100} \geq 7.15 \times 10^{-12}$  counts/(m<sup>2</sup> × yr). Again using the NFW+AC profile the points in yellow are visible after about 5 m<sup>2</sup>-years with  $7.15 \times 10^{-12} > \Phi_{100} \geq 1.43 \times 10^{-12}$  counts/(m<sup>2</sup> × yr). The light gray region is not visible at 5 m<sup>2</sup>-years assuming the NFW+AC profile, if one used an even more favorable profile like the Moore profile then the prospects would be better. Again note that the rescaling has been done and if its removed then models in the Wino-like LSP region have a better chance of being seen as they annihilate the most effectively.

Moving on the the monochromatic photons the treatment will be different. These photons have energies of  $E_\gamma = m_\chi$  for  $\chi\chi \rightarrow \gamma\gamma$  or  $E_\gamma = m_\chi - \frac{m_z^2}{4m_\chi}$  for  $\chi\chi \rightarrow Z\gamma$ , and we have seen that in the DMM model space the neutralino LSP can become rather massive. Typically

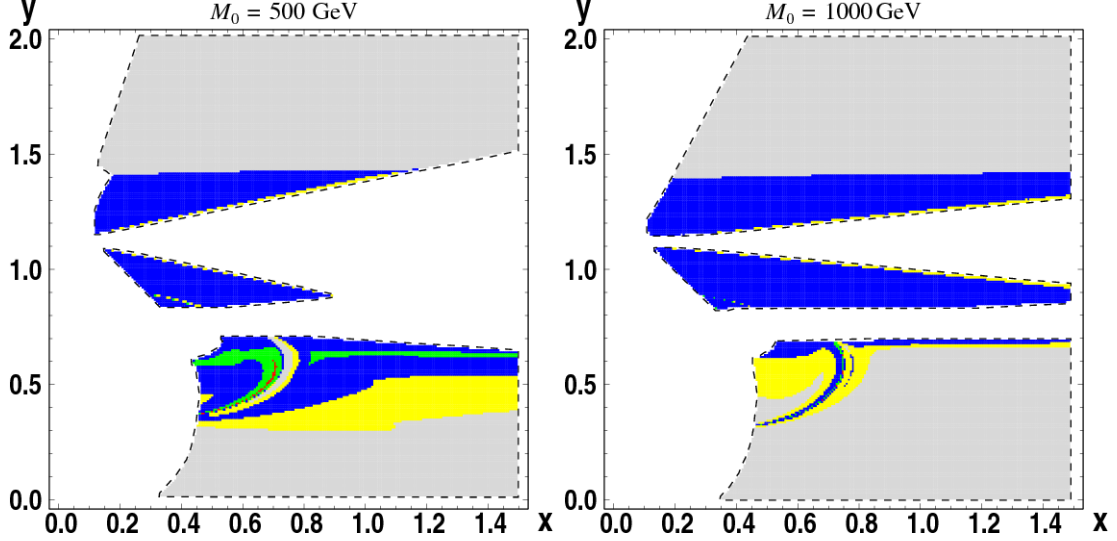


Figure 4.7: **Reach of the Fermi/GLAST Experiment for Integrated Gamma Ray Flux.** Left panel is for  $M_0 = 500$  GeV, right panel is for  $M_0 = 1000$  GeV. Phenomenologically allowed areas are enclosed by the heavy dashed lines. For  $M_0 = 500$  GeV the green shaded region has  $5.79 \times 10^{-10} > \Phi_{100} \geq 1.16 \times 10^{-10}$  photons/cm<sup>2</sup>/sec and therefore may be visible at Fermi/GLAST after five years of exposure with the NFW profile. If the fluxes are rescaled to the NFW+AC profile we obtain the reach shaded in blue (one year of data-taking) and yellow (five years of data-taking). The gray shaded area has an effective flux below  $\Phi_\gamma = 0.014 \times 10^{-10}$  and is unlikely to yield a visible signal for diffuse gamma rays at Fermi/GLAST.

the energies associated with the monochromatic signals will likely be at energies too large to be detected at Fermi/GLAST. However ground based atmospheric Cherenkov telescopes (ACTs) such as CANGAROO [111], HESS [112], MAGIC [113] and VERITAS [114] have thresholds for photon detection in the 100 GeV range and can detect energetic photons up to  $\mathcal{O}(10$  TeV). Data taking for these experiments is only done on dark, cloudless nights but the effective area of the telescopes are generally quite large.

To investigate the prospects for observing the monochromatic signals we need to consider the possible backgrounds and assume certain halo profiles. As in the case of the continuous photons here we will assume either the NFW or NFW+AC halo profiles. The backgrounds for the monochromatic photons are rather low especially at higher photon energies. Therefore we calculate the minimum flux to observe 10 events for a given exposure (in units of area $\times$ time)

Exposure [m <sup>2</sup> yr]	Halo Profile	$\Phi_{10}$ [counts/(cm <sup>2</sup> s)]
1000	NFW	$31.7 \times 10^{-15}$
100	NFW+AC	$3.92 \times 10^{-15}$
500	NFW+AC	$7.83 \times 10^{-16}$
1000	NFW+AC	$3.92 \times 10^{-16}$

Table 4.4: **Reach Estimates in the Monochromatic Gamma Ray Flux for a Generic ACT Experiment.** Flux needed for 10 signal events at a generic ACT assuming various exposures and halo profiles. Note that we are here taking one year of data-taking to be 365 days.

which coincides with the energy resolution of a typical ACT. We will consider a generic ACT with effective area of  $A_{\text{eff}} = 2 \times 10^8 \text{ cm}^2$  with energy resolution of  $\Delta E/E = 0.15$ . The estimated fluxes necessary to produce 10 events in a given exposure and halo profile that will be used are given in Table 4.4.

The results for the monochromatic signals are shown in Figure 4.8. In the figure models with LSP mass below 100 GeV have not been included as ACTs typically do not record data below 100 GeV. The signals from both the  $\gamma\gamma$  and  $\gamma Z$  fluxes have been combined as using the resolution of 15% is not sufficient to be able to differentiate between the two monochromatic signals for LSP masses above about 200 GeV. As in the continuous photon case the prospects are not very good for the monochromatic photons in the parameter space considered. Regions colored in red correspond to the highest fluxes with  $\Phi_{10} \geq 31.7 \times 10^{-15}$  photons/cm<sup>2</sup>/sec and may be visible with the NFW profile given 1000 m<sup>2</sup>-years of exposure. The larger mass case of  $M_0 = 1 \text{ TeV}$  has a better chance of observability as the photons are more energetic for the larger LSP mass case. Using now the NFW+AC profile the regions of green, blue and yellow correspond to  $31.7 \times 10^{-15} > \Phi_{10} \geq 3.91 \times 10^{-15}$  photons/cm<sup>2</sup>/sec,  $3.91 \times 10^{-15} > \Phi_{10} \geq 0.78 \times 10^{-15}$  photons/cm<sup>2</sup>/sec and  $0.78 \times 10^{-15} > \Phi_{10} \geq 0.39 \times 10^{-15}$  photons/cm<sup>2</sup>/sec, respectively. These regions are potentially visible after 1000 m<sup>2</sup>-years of exposure, while the remaining gray regions do not give large enough fluxes to be seen at the largest exposure considered here. As in the case of the diffuse fluxes, the Wino-like LSP and mixed Wino-Higgsino LSP regions have much larger signals when the rescaling is not done.

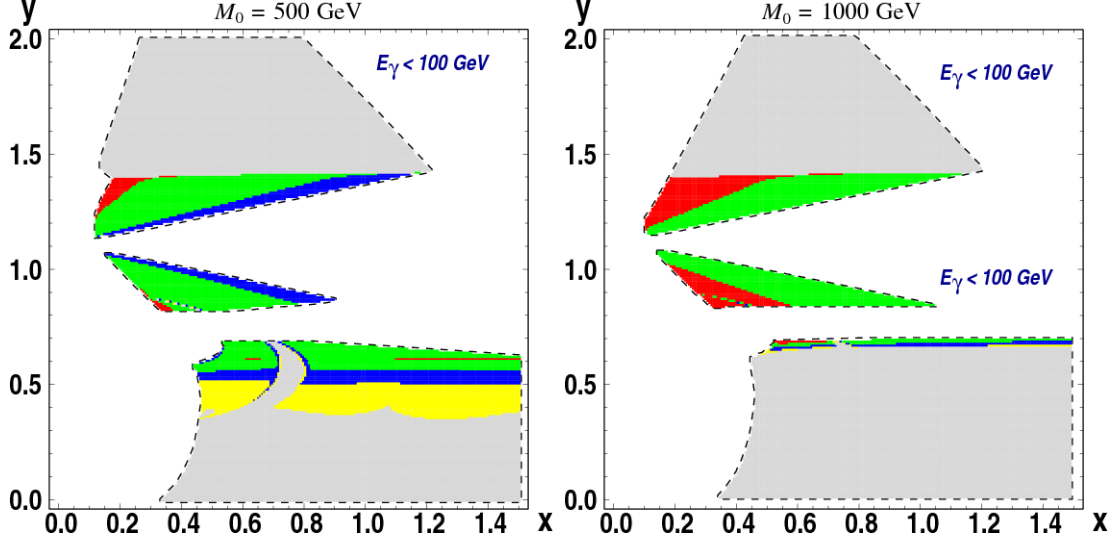


Figure 4.8: **Reach of a generic ACT experiment for Monochromatic Gamma Ray Flux.** Left panel is for  $M_0 = 500$  GeV, right panel is for  $M_0 = 1000$  GeV. Red shaded regions near the edge of the allowed area in the two plots have  $\Phi_{10} \geq 31.7 \times 10^{-15}$  photons/cm<sup>2</sup>/sec. Rescaled to the NFW+AC profile we obtain the reach shaded in green (100 m<sup>2</sup>-yr exposure), blue (500 m<sup>2</sup>-yr exposure) and yellow (1000 m<sup>2</sup>-yr exposure). Note that some of the indicated regions of the parameter space give photon energies below the lower threshold of  $E_\gamma = 100$  GeV and are therefore invisible to our generic ACT. The gray shaded region has a monochromatic flux  $\Phi_{10} \leq 0.39 \times 10^{-15}$  photons/cm<sup>2</sup>/sec and is unlikely to give a visible signal without a more favorable set of halo assumptions.

#### 4.2.4 Muons

Neutrinos from neutralino annihilation in the sun are considered here and the focus is on the IceCube experiment [80]. For these calculations the differential flux of muons is integrated over a energy range of  $50 \text{ GeV} \leq E_\mu \leq 300 \text{ GeV}$ , assuming an angular resolution of 3 degrees. IceCube has a nominal area of 1 km<sup>2</sup>, but the effective detection area is smaller and is dependent on the muon energy [115, 116, 117]. The estimated background of muon events in a year of data taking at IceCube is expected to be  $\mathcal{O}(10)$  [117]. Therefore we estimate the flux necessary to get 10 events during various exposures (in km<sup>2</sup>×yr) at IceCube in Table 4.5.

The results for the  $(x, y)$  planes considered are not very promising for the higher mass case of  $M_0 = 1$  TeV, and therefore the results shown in Figure 4.9 are only for the lower

Exposure [km <sup>2</sup> yr]	$\Phi_{10}$ [counts/(km <sup>2</sup> yr)]
0.2	50
0.5	20
1.5	6.7
10	1.0

Table 4.5: **Muon Flux Estimates for IceCube.** Flux of muons needed to produce 10 signal events at IceCube assuming various exposures.

mass  $M_0 = 500$  GeV case. The figure shows the number of muon events at IceCube in units of counts/ (km<sup>2</sup> × yr) where the combination of muons from the earth and sun are considered (earth born neutrinos offer much lower fluxes and can essentially be ignored). A recent report using 22-strings at IceCube constrain the muon flux to be below 300-500 muons per km<sup>2</sup>×yr [118]. A conservative upper limit of 400 muons per km<sup>2</sup>-yr is used and none of the points in the  $(x, y)$  plane for  $M_0 = 500$  GeV are found to violate this. Some of the points shown can produce a muon flux on the order of 50 or more muons per km<sup>2</sup>-yr as indicated by the red shaded region where  $400 > \Phi_{10} \geq 50$  counts/ (km<sup>2</sup> × yr). The region of flux for  $50 > \Phi_{10} \geq 20$  counts/ (km<sup>2</sup> × yr) is shown in green corresponding to about 0.5 km<sup>2</sup>×yr exposure at IceCube. The remaining two regions of  $20 > \Phi_{10} \geq 6.7$  counts/ (km<sup>2</sup> × yr) and  $6.7 > \Phi_{10} \geq 1.0$  counts/ (km<sup>2</sup> × yr) are shown in blue and yellow, respectively. Points which will not be probed at the 10 km<sup>2</sup>-year level are shown in gray. The regions of the parameter space which have the best prospects for discovery are consistent with mixed Higgsino/gaugino LSP and light supersymmetric Higgs sector.

### 4.2.5 Anti-Matter from cosmic rays

Here we will just be brief and comment on the positron and anti-proton fluxes in the DMM model from [85]. There has been evidence for an excess of positrons in the 10-100 GeV range [119, 120] as reported by the HEAT experiment in the 1990's and more recently the satellite based PAMELA experiment [78] seems to confirm the earlier excesses. There have been many studies (see for example [121, 79] and references therein) which have shown that

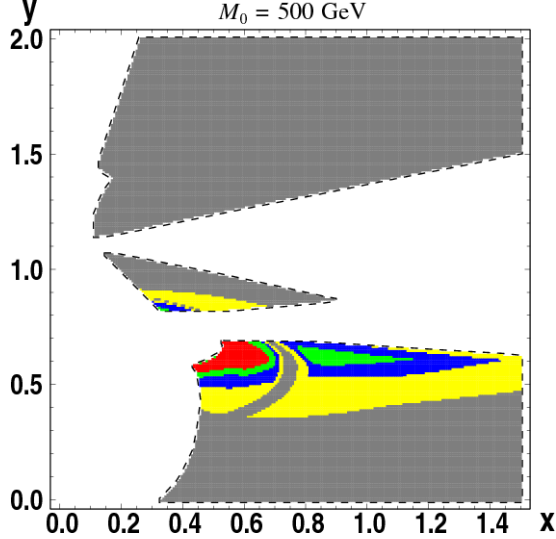


Figure 4.9: **Upward Going Muon Rates at IceCube.** The IceCube reach is shown for  $M_0 = 500$  GeV. The red shaded region is detectable with  $0.2 \text{ km}^2\text{-years}$  of exposure. Green and blue shaded regions would require  $0.5$  and  $1.5 \text{ km}^2\text{-years}$  of exposure, respectively. The yellow region gives a visible signal after  $10 \text{ km}^2\text{-years}$  of exposure. The gray region has a flux below  $1 \text{ muon per km}^2\text{-yr}$  and is likely undetectable at IceCube.

MSSM models can fit the PAMELA data, although the fits require considerable effort and involve boost factors as well as adjusting the parameters in the diffusion equation. Fitting the PAMELA data becomes more difficult if one also takes into account the recent data from the ATIC experiment [122] which reports an excess in the positron signal at even higher energies. Some attempts to explain both the PAMELA and ATIC data can be found in [123, 124, 125]. Indeed it is possible that the reported excesses are not even due to dark matter, but rather due to other astrophysical backgrounds, and understanding the reason for the excess is an ongoing problem.

To investigate the DMM parameter space and how well it may be able to fit the PAMELA data we performed an analysis in [85] which used a boost factor and a chi-squared like variable to pick out regions of the parameter space that were most promising to fit the signal. Using the NFW halo profile along with the default diffusion parameters in `DarkSUSSY 5.0.4` the results of the analysis pointed to regions of the DMM parameter space where the LSP is mostly Wino with a low mass which best can explain the signal. These regions of mostly

Wino LSP required boost factors of  $\mathcal{O}(1)$  (when no rescaling is done) and are consistent with results from other studies [121, 79]. The analysis done was a quick estimate and a more sophisticated analysis for the positron flux may be interesting in this model space.

The PAMELA satellite also recorded data on anti-protons which is consistent with expected backgrounds and previous data [126]. A simple procedure was performed to check the consistency of the anti-proton signal in the DMM parameter space. The differential flux of anti-protons was computed using the NFW profile with default diffusion parameters and the results were checked to be in agreement with the PAMELA data. None of the parameter space was found to be in conflict with the data. However if the boost factor found in the positron analysis is naively applied to the anti-proton signal then much of the parameter space was found to disagree with the PAMELA anti-proton data. Again the analysis was rather simple and if modifications were made to the diffusion parameters then perhaps the conflict could be resolved. Furthermore it is not clear if the same boost factor should be used as the two types of anti-matter are known to propagate differently through the galaxy [127].

### 4.2.6 Benchmarks

We now turn back to look at the benchmark models which were outlined in Table 4.1. As a reminder models A, B and C are specific examples presented in the original papers on deflected mirage mediation [81, 82], models D and E are chosen from the results of our parameter space scans, while model F is a point without gauge-charged messengers with  $\alpha_m = 1$  as in the KKL<sub>T</sub> model. In Table 4.6 the neutralino LSP properties are highlighted along with masses of other key particles and the values of the thermal relic abundance.

The first block of entries in Table 4.6 give the mass and wavefunction composition of the LSP, with the wavefunction composition denoted as in equation (3.2). The second block contains the next-to-lightest-superpartner (NLSP) as well as the masses of the light and pseudo-scalar Higgs bosons, which can have important effects on the thermal relic density.

	Model A	Model B	Model C	Model D	Model E	Model F
$m_{\tilde{N}_1}$	1009	626.6	772.8	257.2	193.2	710.8
$f_B$	0.912	0.989	0.983	0.914	0.000	0.932
$f_W$	0.071	0.001	0.001	0.030	0.997	0.004
$f_H$	0.017	0.009	0.017	0.057	0.003	0.064
NLSP	$\tilde{C}_1$	$\tilde{C}_1$	$\tilde{\tau}_1$	$\tilde{C}_1$	$\tilde{C}_1$	$\tilde{\tau}_1$
$m_{\text{NLSP}}$	1026	743.8	781.3	302.6	193.3	762.8
$m_h$	119.5	120.6	121.5	112.1	119.8	119.9
$m_A$	1559	1043	1136	473.5	1518	1136
$\Omega_\chi h^2$	0.117	0.891	0.517	0.088	0.001	0.537
$R_{\text{Xe}}$	0.046	0.022	0.032	1.182	$7 \times 10^{-5}$	0.178
$R_{\text{Ge}}$	0.037	0.018	0.025	0.881	$6 \times 10^{-5}$	0.140
$\Phi_{\gamma\gamma}$	$1.778 \times 10^{-17}$	$3.517 \times 10^{-17}$	$2.734 \times 10^{-17}$	$4.128 \times 10^{-16}$	$2.071 \times 10^{-15}$	$2.267 \times 10^{-17}$
$\Phi_{\gamma Z}$	$9.169 \times 10^{-17}$	$3.244 \times 10^{-18}$	$3.326 \times 10^{-18}$	$8.868 \times 10^{-16}$	$6.399 \times 10^{-15}$	$1.157 \times 10^{-17}$
$\Phi_{\text{tot}}$	$1.846 \times 10^{-12}$	$2.260 \times 10^{-12}$	$2.041 \times 10^{-12}$	$1.449 \times 10^{-10}$	$1.463 \times 10^{-11}$	$4.319 \times 10^{-12}$
$\Phi_\mu$	0.738	0.194	0.495	11.766	0.016	3.616
$\Phi_{\bar{D}}$	$8.096 \times 10^{-15}$	$2.155 \times 10^{-14}$	$1.195 \times 10^{-14}$	$1.631 \times 10^{-12}$	$2.824 \times 10^{-14}$	$2.560 \times 10^{-14}$
$\Phi_{\bar{p}}$	$7.438 \times 10^{-11}$	$9.979 \times 10^{-11}$	$8.923 \times 10^{-11}$	$6.523 \times 10^{-9}$	$8.617 \times 10^{-10}$	$1.887 \times 10^{-10}$
$B$	4774	5156	5145	102.9	1147	2510

Table 4.6: **Characteristics of Benchmark Models From Table 4.1.** All masses are given in GeV and we denote wave-function components as  $f_B = |N_{11}|^2$ ,  $f_W = |N_{12}|^2$  and  $f_H = |N_{13}|^2 + |N_{14}|^2$ . Direct detection rates  $R_i$  have units of recoils/kg-year. Photon fluxes are given in units of photons/cm<sup>2</sup>/sec and  $\Phi_{\text{tot}}$  represents the diffuse gamma flux integrated from 1 to 200 GeV. The muon flux is given in units of muons/km<sup>2</sup>-year.  $\Phi_{\bar{D}}$  is given in units of anti-deuterons/(GeV s cm<sup>2</sup> sr) and is computed at 0.25 GeV.  $\Phi_{\bar{p}}$  is given in units of anti-protons/(GeV s cm<sup>2</sup> sr) and is computed at 10 GeV.

All of the benchmarks listed have a value of  $\Omega_\chi h^2 < 1$ , while only models A and D are in the WMAP window of  $\Omega_\chi h^2 \simeq 0.11$ , and model E has  $\Omega_\chi h^2 < 0.025$  and therefore has the local halo density rescaled by the factor  $r_\chi = 0.04$ . For all of the models the thermal relic density is affected by coannihilation to varying degrees, and model D is an example of a model in the  $A$ -funnel region with  $2m_\chi \simeq m_A$ .

All of the models, except for the mostly wino LSP in model E, have decent prospects for discovery in direct detection experiments. In terms of the rates mentioned in Table 4.2, the models should be probed in the few hundred kg $\times$ year level, while models D and E offer the best prospects for discovery. It is worth noting that both model D and E have mixed bino/Higgsino LSPs with model D also containing a few percent of Wino (and a lower value of LSP mass). As will be discussed in the next chapter these type of mixed cases typically give rise to the largest rates as both the Higgs exchange and the squark exchange diagrams contribute to the scattering and hence give larger cross sections. The rather low rate of model

E is due to the large Wino content which reduces the Higgs exchange diagrams and if the rescaling is not done the rates are still low, being  $1.75 \times 10^{-3}$  and  $1.5 \times 10^{-3}$  counts/(kg $\times$ yr) on xenon and germanium, respectively.

For the gamma ray photon signals the halo profile used is the NFW profile. To convert to the NFW+AC profile one must simply multiply the fluxes by the conversion factor of  $\bar{J}|_{\text{NFW+AC}}/\bar{J}|_{\text{NFW}} \simeq 81$  using the values in Table 3.1. Model D gives the best signal for the continuous gamma flux at Fermi/GLAST,  $\Phi_{\text{tot}}$ , possibly visible at 1 m<sup>2</sup> $\times$ year over the backgrounds. If the NFW+AC profile is used all of the models have signals which may be observed with 1 m<sup>2</sup> $\times$ year of exposure. Model E gives the largest monochromatic photon fluxes as the Wino LSP annihilates at a higher rate through the 1-loop diagrams (of which many involve  $\tilde{C}$ 's circulating in the loops) and is possibly visible at 5000 m<sup>2</sup> $\times$ year of exposure (i.e. (10 events)/(5000 m<sup>2</sup> $\times$ yr) =  $6.34 \times 10^{-15}$  events/(cm<sup>2</sup> $\times$ sec)). If one uses the NFW+AC profile then models A and D also become promising with  $\Phi_{\text{mono}} = \Phi_{\gamma\gamma} + \Phi_{\gamma Z} \simeq 1.1 \times 10^{-16}$ ,  $13.0 \times 10^{-16}$  photons/(cm<sup>2</sup> $\times$ sec), respectively.

Turning to the muon fluxes from neutralino annihilation in the sun,  $\Phi_{\mu}$ , only models D and F have promising rates which may be detected at IceCube based on the estimates in Table 4.5. To give rates which may be detected at IceCube one needs to have an LSP with sizable Higgsino content as both these models have. Models A, B, C and E are not very promising and give rates which are most likely not detectable at IceCube even at 10 km<sup>2</sup> $\times$ years.

The lowest block of Table 4.6 gives the anti-matter fluxes of anti-protons, the boost factor to fit the PAMELA positron data,  $B$ , and (for completeness) the fluxes of anti-deuterons for the benchmarks. Beginning with the anti-proton flux,  $\Phi_{\bar{p}}$ , all of the models are below the expected background value of  $\mathcal{O}(10^{-7})\bar{p}/(\text{GeV}\times\text{s}\times\text{cm}^2\times\text{sr})$  [128] at a reference point of 10 GeV for the kinetic energy of the anti-proton. All of the models save for model D require rather large boost factors to fit the PAMELA data, however the models were rescaled and if this is not done then the Wino model of point E has a smaller boost. Naively applying the

boost factors to the anti-proton data would give anti-proton fluxes in conflict with the data with signals about an order of magnitude above the background. The anti-deuteron flux,  $\Phi_{\bar{D}}$ , is also included which is computed at a value of kinetic energy of 0.25 GeV for the  $\bar{D}$  which is relevant for the planned GAPS experiment [129]. Only model D is likely to give an observable signal of anti-deuterons.

### 4.3 Summary

Deflected mirage mediation is motivated from realistic string-inspired model building in which the moduli are stabilized and a positive vacuum energy is obtained. The model is also very interesting as it contains contributions to the soft terms which come from gravity, anomaly and gauge mediation. If supersymmetry is discovered in the coming era determining just how the SUSY breaking is transmitted is a highly important question which will need to be addressed. By studying a model which contains the three mediation mechanisms one can build up intuition as to the types of dark matter signals which can be obtained when all three mediation mechanisms are present, as compared to studies which assume a sole contribution to the breaking.

Various regions of the parameter space within the DMM model have been investigated. It has been demonstrated that regions of the parameter space exist in which all three mediation mechanisms contribute to the soft terms and the thermal relic abundance is in agreement with the WMAP measurements. Furthermore regions of the parameter space will be probed at upcoming dark matter experiments and have the potential to be visible above backgrounds. More specifically the parameter space has been shown to give regions which have mixed Higgsino/Wino LSPs which are good candidates to give large event rates at direct detection experiments.

# Chapter 5

## Dark matter signals of non-universal gaugino masses?

This chapter will focus on neutralino dark matter along with some basic LHC collider phenomenology. The focus on dark matter and collider phenomenology in this chapter serves as a link to the following chapter in which the focus will be on non-universal gaugino masses and important LHC signatures which help reveal the level of non-universality which may be present. It is also important to consider not just one arena of observations but to look at both dark matter and LHC observables to better understand the models under study.

The CDMS II experiment recently reported the observation of two nuclear recoil events in 612 kg-days of exposure [70]. The events are consistent with scattering of a WIMP with the germanium nuclei used in the experiment. They measured recoil energies of 12.3 and 15.5 keV, which is near the lower threshold for the experiment. They estimate a signal efficiency of no less than 25% with a maximum of 32% at 20 keV in this energy range. Prior to unblinding the expected background events were  $\Delta N = 0.6 \pm 0.1$  (stat), which can be due to mis-identified electron or neutron scatters from radioactive decays and/or cosmic rays. After investigating the events more closely the background estimate becomes  $\Delta N = 0.8 \pm 0.1$  (stat)  $\pm 0.2$  (syst), so it is quite possible that the two reported events could just be mis-identified background events. If one or both are taken as signal events from WIMP nucleon scattering, it implies a spin independent cross section at the level of few  $\times 10^{-44}$  cm<sup>2</sup>.

Assuming that one or both of the reported events are indeed due to the scattering of

the lightest neutralino in the MSSM, then exciting implications will follow. Some interesting supersymmetric scenarios to explain the events have been investigated, for early works see [130, 131, 132, 133]. In the analysis presented here we highlight the ability of non-universalities within the gaugino sector of the MSSM to explain the events. Specific benchmark models are analyzed which can explain the event(s) reported at CDMS and which make predictions for the upcoming germanium and xenon based direct detection experiments. Also considered are indirect signal predictions for gamma-ray experiments such as Fermi/GLAST [108] and the neutrino experiment at IceCube [80]. The signal from the PAMELA experiment [78] will be discussed, along with the compatibility of the benchmarks to accommodate the relic abundance as favored by WMAP. Also some basic LHC predictions for these benchmarks will be given for center of mass energies of  $\sqrt{s} = 7, 10$  and  $14$  TeV for  $1 fb^{-1}$  of luminosity. This analysis is based on the work in [134].

## 5.1 Benchmark models for CDMS II signal

The sensitivity of the CDMS II experiment can be translated to the spin independent (SI) cross section for proton-neutralino scattering,  $\sigma_{\chi p}^{\text{SI}}$  and is dependent on the mass of the neutralino. For LSPs with masses between 100 and 300 GeV a detectable event rate at CDMS II implies a cross-section  $\sigma_{\chi p}^{\text{SI}} \gtrsim \text{few} \times 10^{-44} \text{ cm}^2$ . Assuming a signal efficiency of 30% at the CDMS II experiment then the effective exposure is 184 kg-days. A cross section of  $\sigma_{\chi p}^{\text{SI}} = 10^{-44} \text{ cm}^2$  for  $m_{\chi} \simeq 150$  GeV implies about 0.5 events in this 184 kg-day exposure, which is useful to compare to the data. In supersymmetry models with universal gaugino masses which have mostly bino-like LSPs the interaction cross sections are generally too low [135, 136] to be able to explain the CDMS II data. In particular the SI cross section can be dominated by t-channel diagrams involving Higgs exchange, which depend on the Higgsino content of the LSP. Neutralino LSPs with a sizable mixture of non-Bino components, in particular Higgsino, can give  $\sigma_{\chi p}^{\text{SI}}$  values in the range favored by CDMS II [137, 138, 139,

140, 141, 142].

The supersymmetric model framework considered here is the mSUGRA model [25, 44] with non-universal gaugino masses (NUGM) [143]. The mSUGRA model is defined at  $Q_{\text{GUT}} \simeq 2 \times 10^{16}$  GeV via the universal scalar mass,  $m_0$ , the universal gaugino mass,  $m_{1/2}$ , the universal trilinear coupling,  $A_0$ ,  $\tan \beta$  and  $\text{sign}(\mu)$ . To introduce the non-universalities we use

$$M_a = m_{1/2}(1 + \delta_a) \quad (5.1)$$

and only consider  $\delta_2, \delta_3 \neq 0$ . The approach here is similar to the method explored in [139, 140] and has been shown to give SUSY models compatible with direct and indirect constraints while having relatively large values of  $\sigma_{\chi p}^{\text{SI}}$  [144, 145]. The neutralino wavefunction also depends on the supersymmetric Higgs mass  $\mu$  which is determined by solving the EWSB conditions at the low scale. The soft gluino mass  $M_3$  is important to the LSP in an indirect way as it influences the eventual value of  $\mu$  via the RGE effects on the running of the Higgs soft scalar masses [146, 147, 148].

The dependence of  $\sigma_{\chi p}^{\text{SI}}$  on the LSP wavefunction is given explicitly in equations (3.13) and (3.14). As a demonstration of how the cross section depends on the LSP wavefunction we show in Figure 5.1 a sample of model points within the framework considered here, plotted as  $m_\chi$  vs  $\sigma_{\chi p}^{\text{SI}}$ . No constraint on  $\Omega_\chi h^2$  is imposed and points are grouped according to wavefunction composition. Blue circles have  $f_B \geq 95\%$ , red  $f_W \geq 95\%$ , green  $f_H \geq 95\%$  and gray are otherwise, e.g. mixed LSP states. This figure demonstrates how the mixed LSPs may better account for the CDMS II signal and is a guide to choosing specific benchmark models of which can explain the CDMS II signal. Points in Figure 5.1 satisfy current collider searches for superpartner masses using the approach of [149] which takes bounds from [23]. The light Higgs mass lower bound is relaxed a bit, and the bounds used with masses in GeV are

$$m_h > 110$$

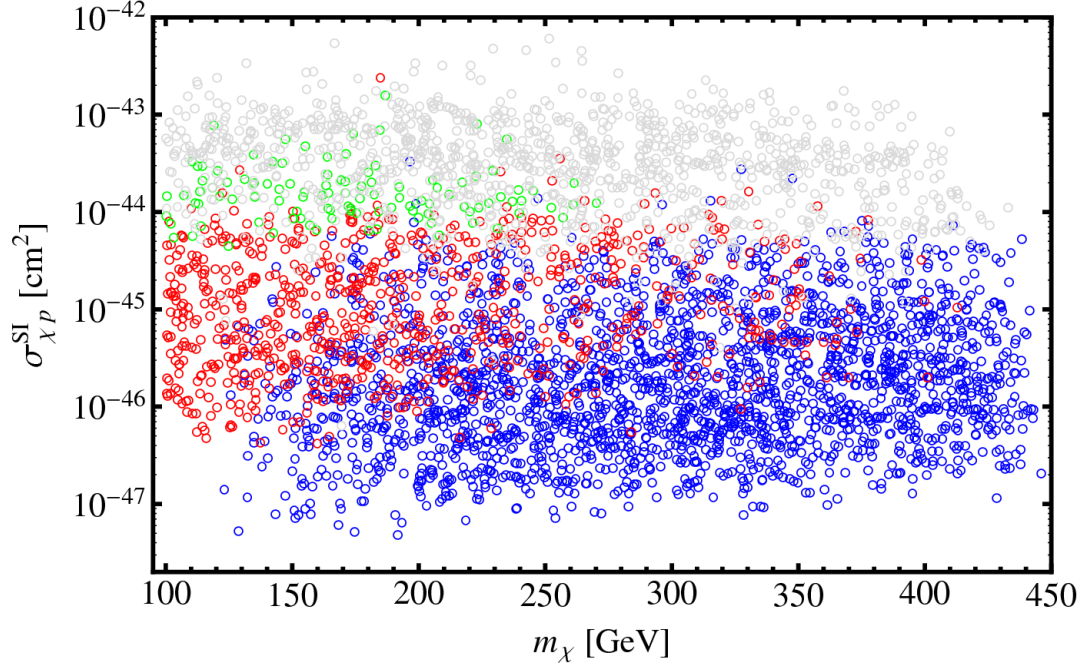


Figure 5.1: **Neutralino-proton spin independent scattering cross sections for NUGM.** Prediction for the neutralino-proton spin independent scattering cross section  $\sigma_{\chi p}^{\text{SI}}$ , as computed by DarkSUSY, is displayed as a function of the LSP mass  $m_\chi$ .

$$m_{\tilde{N}_1} > 50$$

$$m_{\tilde{C}_1} > 100$$

$$m_{\tilde{g}} > \begin{cases} 310 & m_{\tilde{g}} \neq m_{\tilde{q}} \\ 390 & m_{\tilde{g}} = m_{\tilde{q}} \end{cases}$$

$$m_{\tilde{q}} > 300 \quad q = u, d$$

$$m_{\tilde{b}_1} > \begin{cases} 90 & m_{\tilde{b}_1} - m_{\tilde{N}_1} \geq 10 \\ 70 & m_{\tilde{b}_1} - m_{\tilde{N}_1} < 10 \end{cases}$$

$$m_{\tilde{t}_1} > \begin{cases} 96 & m_{\tilde{t}_1} - m_{\tilde{N}_1} \geq 10 \\ 76 & m_{\tilde{t}_1} - m_{\tilde{N}_1} < 10 \end{cases}$$

$$m_{\tilde{e}_R} > 73$$

$$m_{\tilde{\mu}_R} > \begin{cases} 94 & m_{\tilde{\mu}_R} - m_{\tilde{N}_1} \geq 10 \\ 74 & m_{\tilde{\mu}_R} - m_{\tilde{N}_1} < 10 \end{cases}$$

$$m_{\tilde{\tau}_1} > \begin{cases} 82 & m_{\tilde{\tau}_1} - m_{\tilde{N}_1} \geq 10 \\ 72 & m_{\tilde{\tau}_1} - m_{\tilde{N}_1} < 10. \end{cases} \quad (5.2)$$

The points shown in Figure 5.1 also satisfy electroweak precision bounds. We impose a  $3\sigma$  bound on  $\text{br}(b \rightarrow s\gamma)$  using the recent HFAG measurement [150].

$$2.77 \times 10^{-4} < \text{br}(b \rightarrow s\gamma) < 4.27 \times 10^{-4}, \quad (5.3)$$

as well as a conservative bound [151] on  $a_\mu$  and  $\Delta\rho$

$$-5.7 \times 10^{-10} < \frac{g_\mu - 2}{2} < 47.0 \times 10^{-10} \quad (5.4)$$

$$\Delta\rho < 2.2 \times 10^{-3} \quad (5.5)$$

and a 95% CL upper bound [152] on  $(B_s \rightarrow \mu^+\mu^-)$  of

$$\text{br}(B_s \rightarrow \mu^+\mu^-) < 5.8 \times 10^{-8}. \quad (5.6)$$

Table 5.1 contains five benchmark points with event rates in a similar range to the events reported by CDMS II. The upper portion gives the GUT scale inputs and all points have positive  $\mu$ . The consistent choice of  $\delta_3 < 0$  is preferred as it tends to decrease the value of  $\mu$ , and therefore increase the LSP Higgsino content. The lower portion of the table gives the relevant information to connect these models to the CDMS II signal. The LSP mass and wavefunction composition is given as well as the value of  $\sigma_{xp}^{\text{SI}}$  and the expected event rate over a recoil energy range of  $10 \leq E \leq 100$  keV on a germanium target in an exposure of  $0.3 \times 612 = 183.6$  kg-days. Furthermore the benchmarks were chosen to have varying wavefunctions as can be seen in the table. The inputs are run to the low scale using **Suspect 2.4** and fed to **DarkSUSY**.

Due to the low statistics reported by the data any one of these points could be interpreted

Point	A	B	C	D	E
$m_0$	750	500	350	350	350
$m_{1/2}$	750	500	575	575	575
$A_0$	370	270	150	150	100
$\tan \beta$	25	15	30	30	30
$\delta_2$	0.65	0.62	-0.6	0.82	-0.47
$\delta_3$	-0.35	-0.3	-0.3	-0.35	-0.3
$m_{\chi_1^0}$ (GeV)	138	190	175	112	230
B%	3.0%	70.2%	0.3%	5.4%	40.9%
W%	0.4%	0.4%	95.8%	0.5%	53.0%
H%	96.6%	29.4%	3.9%	94.1%	6.1%
$\sigma_{\chi p}^{\text{SI}} \times 10^{45}$ (cm <sup>2</sup> )	11.9	44.4	41.3	35.3	74.8
$N_{\text{Ge}}$ (184 kg-days)	0.51	1.36	1.30	1.65	1.90

Table 5.1: Soft term parameters for selected benchmark points are shown in the upper portion. All masses are given in units of GeV and all points were picked to have  $\mu > 0$ . In the lower portion masses and LSP properties were computed using `SuSpect 2.41`, while scattering cross-sections and the expected number of events were computed using default values in `DarkSUSY 5.0.4`. These scattering cross sections and event rates carry uncertainties associated with certain nuclear matrix elements, as mentioned in the text. The event rates on germanium nuclei assume an effective exposure of 183.6 kg-days as appropriate for the CDMS II data.

to give rise to the signal. It is important to note also that the uncertainties involved with the calculation of the interaction rates can be quite large. As a comparison using `MicrOmegas` [59] one finds that the rates predicted for germanium are about twice as large. That this happens is due to a different value of the  $\pi N \Sigma$  term which leads to different values in the strange quark hadronic form factor. With the statistical and theoretical uncertainties in mind the benchmark models have been chosen to have  $0.5 \leq N_{\text{Ge}} \leq 2.0$  to be conservative. It is noted that recent calculations of the matrix element  $\langle n | s \bar{s} | n \rangle$  [153] may imply an even lower value for  $\sigma_{\chi p}^{\text{SI}}$  which would make the interpretation of CDMS II data as scattering of neutralino LSPs more difficult.

## 5.2 Other DM signals

Upon selecting candidate models as outlined in Table 5.1, which give reasonable rate predictions which can be interpreted to give rise to the signal at CDMS II, we now look at other experimental predictions relevant to other dark matter detection experiments. Based on the low statistics given from the CDMS II experiment it is not clear whether the events truly correspond to neutralino nucleon scattering. The choice of benchmark models given in Table 5.1 also represents a variety of LSP possibilities which can explain the signal. It is important to be able to use data from other experiments to help confirm if these are truly SUSY events. Here we consider the implications on upcoming direct and indirect detection experiments for the benchmark models considered. To begin we first look at the rates predicted by the benchmarks on xenon targets, as Xenon10 has already published limits [69] and soon Xenon100 will probe further into the SUSY parameter space.

Using the Xenon10 reported limits we first check that the models put forth are in agreement with what was reported in [69]. The rate calculation for the xenon targets are performed in the same manner as the germanium rates although for the Xenon10 and Xenon100 experiments we perform the integration over a smaller range from 5 to 25 keV as this is quite similar to the range of recoils considered in [69]. The initial reported data from Xenon10 utilized an exposure of 316.4 kg $\times$ days and the group reported about 10 events where the signal was expected, although these events were consistent with their background estimation. As can be seen in Table 5.2 the predicted rates of the benchmarks at Xenon10 are in the one to five event range in the exposure of 316.4 kg $\times$ days, and therefore are consistent with what that experiment measured. In the future upgrade of Xenon100 the predictions for the event rates of the candidate models are much larger, as the exposure can increase significantly. For the Xenon100 predictions we assume a fiducial mass of 80% of the nominal mass target of 100 kg as well as 60 days of exposure time, thus the predicted number of events at Xenon100 are for an exposure of 13.15 kg $\times$ years. Assuming a reliable method of background rejection at Xenon100, the benchmark models ought to give clear signals of LSP-nucleon scattering

Point	A	B	C	D	E
$R_{\text{Xe}}$ ( $\text{kg}^{-1}\text{-yr}^{-1}$ )	1.32	3.64	3.66	4.63	5.15
$N_{\text{Xe}}$ (Xenon10)	1.14	3.16	3.17	4.01	4.47
$N_{\text{Xe}}$ (Xenon100)	17.4	47.9	48.1	60.9	67.7
$(\Phi_{\text{int}}/J) \times 10^{15}$ ( $\text{cm}^{-2} \text{ s}^{-1}$ )	196.8	9.27	1020.4	243.8	164.1
$\Phi_{\gamma\gamma}/\Phi_{\gamma Z}$	0.52	0.20	0.33	0.57	0.31
$\Phi_{\mu}$ ( $\text{km}^{-2} \text{ yr}^{-1}$ )	114.0	171.3	63.4	130.7	123.5
$\langle\sigma v\rangle_{WW} \times 10^{25}$ ( $\text{cm}^3/\text{s}$ )	1.9	0.1	23.8	2.0	4.5
$\Omega h^2 _{\text{thermal}}$	0.005	0.112	0.001	0.006	0.003

Table 5.2: Predictions of the benchmark models in Table 5.1 for other dark matter search experiments including the thermal relic density of neutralinos. All calculations were performed using DarkSUSY 5.0.4.

events at the upcoming Xenon100 experiment as can be seen in Table 5.2.

If a clear signal above background is observed in the upcoming liquid xenon direct detection experiments then it provides more evidence that the CDMS II experiment indeed observed a dark matter scattering event. It would also lend evidence that the events are truly the result of neutralino-nucleon scattering consistent with the LSP of the MSSM. However if it is indeed the case that a supersymmetric neutralino is responsible then many models (of which Table 5.1 are just a few) may give rise to compatible signals in the direct detection experiments. It would be desirable to obtain some further evidence from the dark matter experimental efforts to try to reduce the possible models within supersymmetry which may be responsible for the observed signals. As the benchmarks given in Table 5.1 are quite different especially in regard to the LSP wavefunction and mass one ought to look at what types of predictions can be made for the indirect detection signals and what types of differences are expected.

The Fermi/GLAST satellite is currently observing the flux of gamma ray photons from the galactic center, and some of these photons may be the result of neutralino annihilation. It may be possible to observe a significance of the photons from neutralino annihilation over the astrophysical backgrounds. As has been discussed previously in the Chapter 3 the flux of gamma ray photons from neutralino annihilation depends on both the supersymmetric model

inputs as well as the assumed dark matter halo profile at the center of the galaxy. Assuming an angular resolution of  $\Delta\Omega = 10^{-5}$  steradians which corresponds to the Fermi/GLAST satellite the choices of the NFW halo profile gives  $\bar{J} = 1.2644 \times 10^4$ . To compute the expected continuum photon flux at Fermi/GLAST we use the NFW profile and integrate the differential photon flux over the energy range 1 to 200 GeV. The results for the continuum photon flux are given in Table 5.2 where the halo dependence has been factored out, e.g. we give the value of  $\Phi_\gamma/\bar{J}$  and one may estimate the fluxes for different halo profiles using the values of  $\bar{J}$  in Table 3.1. Using the predicted background flux of  $\Phi_{100} = 5.79 \times 10^{-10}$  photons/(cm<sup>2</sup>×sec) necessary to give 100 photon events for 1 m<sup>2</sup>×yr at Fermi/GLAST (from Table 4.3) we can convert this to  $(\Phi_{100}/\bar{J}_{\text{NFW}}) \times 10^{15} = 45.8$  photons/(cm<sup>2</sup>×sec). All the benchmark models except for model B are above this value and hence have good discovery prospects at Fermi/GLAST for the NFW profile, however we stress that the estimates can vary across many orders of magnitude depending on the halo profile employed.

Along with the diffuse gamma ray photons just described the smoking gun signals of 1-loop neutralino annihilation to  $\gamma\gamma$  and  $\gamma Z$  can offer other important experimental evidence for the existence of neutralino dark matter [154, 155, 156]. To investigate these signals in Table 5.2 we compute the ratio of these line fluxes as it eliminates the halo dependence and it is known that this ratio is correlated with the wavefunction of the LSP [157]. The ratio of  $\Phi_{\gamma\gamma}/\Phi_{\gamma Z}$  varies by as much as a factor of 2 across the different benchmarks and gives important information as to the type of LSP which may be responsible for the scattering. However the ability of the atmospheric Cherenkov telescopes to measure these signals will require a favorable halo profile as well as very good energy resolution to be able to resolve the two independent line signals.

Another promising signal of neutralino dark matter can arise from neutrinos which arise from LSP annihilation in the sun. For these signals the halo profile issues are no longer present and the signals can vary quite a bit based on the makeup of the LSP. Some fraction of the neutrinos which are produced from neutralino annihilation in the sun will escape and

travel to the Earth where they can be detected, for example at IceCube [80] via the conversion of muon neutrinos into muons. Using an angular resolution of 3 degrees appropriate for IceCube we integrate the differential flux of conversion muons from both the sun and Earth over the muon energy range of 50 to 300 GeV. IceCube has a nominal target area of 1 km<sup>2</sup>, although the effective area for muon detection is smaller and dependent on the muon energy [115, 116, 117]. As can be seen in Table 5.2 the conversion muon flux,  $\Phi_\mu$ , for the benchmark models are below the limit of about 300-400 muons/(km<sup>2</sup>×year) which was set based on a 22-string run at IceCube. These models are promising for the upcoming runs at IceCube and using an exposure of 0.2 km<sup>2</sup>-years all of the benchmarks can produce at least 10 signal events (an estimate of the background expected at IceCube).

Anti-matter from cosmic rays offer further evidence for the existence of neutralino dark matter. Here we focus on the positron flux and implications to the recent PAMELA data of positrons in the 10-100 GeV energy range [78]. It is now understood that standard MSSM models can fit the apparent positron excess at PAMELA, but doing so requires some difficulty. In order to fit the data it has been pointed out that a thermally averaged annihilation cross section into  $W^+W^-$  final states is necessary. Models with significant Wino or Higgsino content are able to give  $\langle\sigma v\rangle_{WW} \sim 10^{-24}$  cm<sup>3</sup>/s and thus may be able to explain the positron excess [123, 121]. Looking at Table 5.2, it is apparent that model C has the best prospects to agree with the PAMELA data, while the others have a bit too low of value of  $\langle\sigma v\rangle_{WW}$  (although still in the right neighborhood). Typically models which do give large annihilation rates to  $W^+W^-$  also annihilate very effectively in the early universe and thus deplete the value of  $\Omega_\chi h^2$ , as is seen for the mostly Wino benchmark of model C. Only one of the models, model B, gives a value of  $\Omega_\chi h^2$  in the range of  $2\sigma$  WMAP three year data [98] of

$$0.0855 \leq \Omega_\chi h^2 \leq 0.1189, \quad (5.7)$$

while the other models are well below this. The other model points ought to be able to fit the measured value of  $\Omega_\chi h^2 \simeq 0.11$  if one applies non-thermal production mechanisms [62, 99,

Point	A	B	C	D	E
$m_{\chi_1^0}$	138	190	175	112	230
$m_{\chi_2^0}$	152	254	235	130	239
$m_{\chi_3^0}$	326	261	505	252	504
$m_{\chi_4^0}$	1008	663	513	846	515
$m_{\chi_1^\pm}$	146	243	175	123	234
$m_{\chi_2^\pm}$	1008	663	514	846	515
$m_{\tilde{g}}$	1156	847	952	890	951
$m_{\tilde{t}_1}$	826	607	719	544	709
$m_{\tilde{t}_2}$	1284	925	862	964	865
$m_{\tilde{b}_1}$	1155	853	809	766	812
$m_{\tilde{b}_2}$	1271	903	874	943	871
$m_{\tilde{\tau}_1}$	740	520	344	338	352
$m_{\tilde{\tau}_2}$	1079	724	414	752	424
$m_h$	115	112	113	114	113
$\sigma_{\text{SUSY}}^{7\text{TeV}}$ (pb)	1.3	0.3	1.2	2.7	0.4
$\sigma_{\text{SUSY}}^{10\text{TeV}}$ (pb)	2.3	1.2	2.5	5.1	1.3
$\sigma_{\text{SUSY}}^{14\text{TeV}}$ (pb)	4.0	4.1	5.7	10.0	3.7

Table 5.3: Relevant SUSY mass spectra and total production cross sections at the LHC, for the benchmark models in Table 5.1. All masses are in GeV.

100, 101]. Note that the models which have  $\Omega_\chi h^2 < \Omega_\chi h_{\text{min}}^2 = 0.025$  have *not* been rescaled by the factor  $r_\chi$  in equation (3.10) as the assumption is that the non-thermal mechanisms can bring them in line with the WMAP measurement and thus not require the rescaling.

### 5.3 LHC signatures

Here we consider some common search strategies at the LHC and indicate which signals may help reveal the models considered in Table 5.1. In Table 5.3 the key physical masses of the benchmark models are given following renormalization group evolution from  $Q_{\text{GUT}}$  to the low scale using **Suspect 2.41**. A common feature is a compressed gaugino sector, specifically the mass gap  $\Delta^\pm \equiv m_{\chi_1^\pm} - m_{\chi_1^0}$  is rather small. This mass gap is crucial to many standard SUSY search channels at the LHC involving leptons and can result in soft leptons which do not trigger and escape detection.

The analysis of the models at the LHC involves generating the events using PYTHIA [158] with the detector simulator PGS4 [159]. Prior to inputting the models to PYTHIA the Higgs and superpartner masses are calculated using SUSYHIT [160] which includes important loop decays not implemented in PYTHIA. For each of the benchmark models considered  $1 \text{ fb}^{-1}$  of data was generated at center of mass energies of  $\sqrt{s} = 7, 10$  and  $14 \text{ TeV}$ . Also  $1 \text{ fb}^{-1}$  samples of Standard Model background processes were also considered which consist of Drell-Yan, QCD dijet,  $t\bar{t}$ ,  $b\bar{b}$ ,  $W/Z$ +jets and diboson production at the same three values of  $\sqrt{s}$ . These backgrounds are further discussed in the Appendix 9. The level 1 (L1) triggers in PGS are used which were designed to mimic the CMS trigger tables [161].

The last line of Table 5.3 gives the total tree-level SUSY production at the LHC for center of mass energies  $\sqrt{s} = 7, 10$  and  $14 \text{ TeV}$ . The discovery prospects at the LHC at  $\sqrt{s} = 7 \text{ TeV}$  for these models is not so good, especially if the missing energy,  $\cancel{E}_T$ , and  $p_T$  measurements are not reliable. Also the leptonic signatures suffer in these models (to be discussed below) and as so we consider the higher energies which have better discovery prospects.

To gain some basic insight to these models we consider standard SUSY discovery modes [162, 163] which are slightly modified to maximize the signal significance. Table 5.4 gives the five signatures which are considered along with the number of signal events and signal significance,  $S/\sqrt{B}$ , at  $\sqrt{s} = 10 \text{ TeV}$ . Results are also shown in Table 5.5 for a center of mass energy  $\sqrt{s} = 14 \text{ TeV}$ . For all events an initial cut is applied on the post L1 data of transverse sphericity  $S_T \geq 0.2$  and  $\cancel{E}_T \geq 250 \text{ GeV}$  for all signatures except the trilepton signal where we only require  $\cancel{E}_T \geq 200 \text{ GeV}$ . The multijet signature requires no isolated leptons and requires at least four jets with transverse momenta satisfying  $p_T \geq 200, 150, 50, 50 \text{ GeV}$ , respectively. For the leptonic signatures we consider only  $\ell = e, \mu$  and require at least two jets with  $p_T \geq 100, 50 \text{ GeV}$ , respectively.

The multijet signal gives the best prospect for signal significance for these models. In Table 5.4 we see that for all models except A the multijet signature gives the best discovery channel at  $\sqrt{s} = 10 \text{ TeV}$ . Model A has the heaviest gluino and therefore the multijet events

Numbers of Events					
Point	A	B	C	D	E
Multijets	16	68	72	114	57
$1\ell + \text{jets}$	17	78	61	70	19
OS $2\ell + \text{jets}$	0	14	2	12	1
SS $2\ell + \text{jets}$	0	1	2	4	0
$3\ell + \text{jets}$	0	4	0	4	0

Significance $S/\sqrt{B}$					
Point	A	B	C	D	E
Multijets	2.0	8.4	8.9	14.0	7.0
$1\ell + \text{jets}$	1.1	5.2	4.1	4.7	1.7
OS $2\ell + \text{jets}$	NA	4.4	0.6	3.8	0.3
SS $2\ell + \text{jets}$	NA	1.0	2.0	4.0	NA
$3\ell + \text{jets}$	NA	2.9	NA	2.9	NA

Table 5.4: Number of signal events for standard discovery channels at the LHC for  $\sqrt{s} = 10$  TeV for the benchmark models of Table 5.1.

are more suppressed than the other benchmarks. The leptonic signatures are best for model B which has the largest value of  $\Delta^\pm$  at about 50 GeV. When this value gets much below about 10 GeV the leptonic signatures can become less effective as the leptons generally have too little  $p_T$  to be triggered. This reduction in the leptonic signal is likely to be a generic property of non universalities in the gaugino sector. As the energy increases to  $\sqrt{s} = 14$  TeV the models become visible in at least two of the five channels at least  $4.5\sigma$  level, except for model A which does have a  $2.5\sigma$  significance in the 1 lepton + jets channel. Also of note is that in all models  $m_{\tilde{C}_1}$  and  $m_{\tilde{N}_2}$  do not get heavier than about 250 GeV, which indicates the states should be accessible at a  $\sqrt{s} = 500$  GeV  $e^+e^-$  linear collider.

## 5.4 Summary

If the CDSM-II data is indeed due to the scattering of neutralinos from nuclei then the analysis presented here suggests that within the MSSM non-universalities in the gaugino sector are highly likely, although not necessary. The CDMS II data seems to prefer MSSM models with a suppression of the gluino mass as compared to typical predictions made

Numbers of Events					
Point	A	B	C	D	E
Multijets	99	321	402	436	298
$1\ell + \text{jets}$	62	336	202	310	111
OS $2\ell + \text{jets}$	8	45	12	45	7
SS $2\ell + \text{jets}$	2	19	6	16	3
$3\ell + \text{jets}$	3	8	4	6	1

Significance $S/\sqrt{B}$					
Point	A	B	C	D	E
Multijets	6.6	21.4	26.9	29.1	19.9
$1\ell + \text{jets}$	2.5	13.6	8.2	12.5	4.5
OS $2\ell + \text{jets}$	1.3	7.4	2.0	7.4	1.2
SS $2\ell + \text{jets}$	0.8	7.2	2.3	6.0	1.1
$3\ell + \text{jets}$	1.2	3.3	1.6	2.5	0.4

Table 5.5: Number of signal events for standard discovery channels at the LHC for  $\sqrt{s} = 14$  TeV for the benchmark models of Table 5.1.

such as in mSUGRA. The data may also favor a compression in the electroweak gaugino masses which would lead to diminished lepton-based discovery modes at the LHC. We have chosen some benchmarks which give event rates favorable to the reported data by CDMS II and we have given some basic predictions for other dark matter experiments and LHC signatures. These predictions are important as they serve to give a picture of what to expect at future experiments if the events reported at CDMS II are indeed due to neutralino-nucleon scattering. Furthermore if the neutralino turns out to be mostly Wino or Higgsino then it appears that scenarios with non-thermal production mechanisms will become more likely. The models considered here are predicted to have clear signals at the upcoming XENON100 experiment along with the IceCube experiment and therefore positive results from those experiments will further lend evidence to non-universalities in the gaugino sector.

# Chapter 6

## LHC phenomenology of non-universal gaugino masses

In this chapter the focus is on collider aspects of non-universal gaugino masses. Here interest is on how a specific string-based non-universality in the gaugino sector may reveal itself at the LHC. This is a convenient parameterization for non-universal gaugino masses as it involves a single parameter  $\alpha$  which relates the three soft gaugino masses along with an overall mass scale. The models under consideration here are simple versions of the DMM parameter space of Chapter 4 with  $N_m = 0$ . Specific signatures are investigated which have been shown to be useful for models with non-universalities in the gaugino sector [164]. Two specific benchmark models are studied and the resulting LHC phenomenology is studied for varying values of the  $\alpha$  parameter. It is shown that certain signatures are more effective at tracking changes in the value of  $\alpha$ , and among the most important is the effective mass variable.

First the parametrization of the gaugino masses is briefly discussed followed by a description of the two benchmark models which the analysis is based upon. These benchmark models will form the base models by which  $\alpha$ -lines are set up. Next certain signatures are highlighted which have been shown to be effective in tracking the variations of the  $\alpha$  parameter along with comments on how to distinguish different values of  $\alpha$  for the same model. Last the LHC signatures under consideration are analyzed for the two model lines investigated here and the amount of luminosity required to differentiate models along the  $\alpha$ -lines are shown.

## 6.1 Background

Before discussing the benchmark models it is necessary to briefly go over the non-universal gaugino mass parameterization considered here. The parametrization considered is based on work in [88] and references therein. The authors of [88] considered many classes of string motivated models and in particular one called mirage mediation provides a nice way to introduce gaugino mass non-universalities via a single parameter  $\alpha$ . The name mirage comes from the fact that for non-zero values of  $\alpha$  the gaugino masses unify at a scale which is different from  $Q_{\text{GUT}} \simeq 2 \times 10^{16}$  GeV where the gauge couplings continue to unify.

The theoretical background for the mirage pattern are string motivated scenarios like KKLT modulus stabilization in D-brane models [89, 165] as well as Kähler stabilization in heterotic string theory [166]. It is also worth noting that this scenario can also arise in non string based models like deflected-anomaly mediation [167, 168]. As in the models of Chapter 4 a universal contribution to the gaugino masses at the high scale (taken as  $Q_{\text{GUT}}$ ) is balanced by a contribution proportional to the beta function coefficients of the three Standard Model gauge groups. The universal contribution is associated with Planck-suppressed operators (gravity mediation) while the contribution proportional to the beta function coefficients is associated with anomaly mediation. The mirage parametrization is a tunable scenario which allows one to move between the two mediation mechanisms. The focus here will be on small deviations from universality, and the benchmark models give rise to specific predictions of the  $\alpha$  parameter.

It is instructive to outline the manner in which the mirage pattern arises for the gaugino masses. Here we will be general and not adhere to any underlying string framework. Assume that the supersymmetry breaking effects are transmitted to the observable sector at a high scale  $Q_{\text{GUT}}$  and that the gaugino masses get two contributions: a universal contribution  $M_u$  as well as a contribution from anomaly mediation  $m_{3/2}$ . The anomaly contribution is proportional to the beta function coefficients and appears at the 1-loop [169, 170] level so

we can write

$$M_a(Q_{\text{GUT}}) = M_u + g_a^2(Q_{\text{GUT}}) \frac{b_a}{16\pi^2} m_{3/2}. \quad (6.1)$$

Subsequent renormalization group evolution to a lower scale  $Q < Q_{\text{GUT}}$  along with some new definitions gives

$$\frac{M_a(Q)}{g_a^2(Q)} = \frac{M_u}{g_{\text{GUT}}^2} \left( 1 + g_{\text{GUT}}^2 b_a \alpha \frac{\ln(M_{\text{Pl}}/m_{3/2})}{16\pi^2} \right), \quad (6.2)$$

where  $g_a^2(Q_{\text{GUT}}) = g_{\text{GUT}}^2 \simeq 1/2$  is the unified gauge coupling and the  $\mathcal{O}(1)$  parameter  $\alpha$  is defined as

$$\alpha \equiv \frac{m_{3/2}}{M_u \ln(M_{\text{Pl}}/m_{3/2})}. \quad (6.3)$$

The definition of  $\alpha$  follows [88] and is seen to be  $\alpha_m$  of equation (4.3) with  $M_u = M_0$ . The gaugino masses no longer unify at  $Q_{\text{GUT}}$  for  $\alpha \neq 0$ , rather they unify at some other scale  $Q_{\text{mir}}$

$$Q_{\text{mir}} = Q_{\text{GUT}} \left( \frac{m_{3/2}}{M_{\text{Pl}}} \right)^{\alpha/2} \quad (6.4)$$

which for values of  $0 \leq \alpha \leq 2$  happens at a scale between the weak scale (1 TeV) and  $Q_{\text{GUT}}$ , hence “mirage”. Models which exhibit mirage unification result in compressed gaugino mass values at the low scale relative to the universal case. The parametrization in equation (6.2) is theoretically quite interesting and also offers a nice way to parametrize non-universalities in the gaugino sector at the low scale as the ratios of the three soft gaugino masses at 1 TeV are

$$M_1 : M_2 : M_3 = (1.0 + 0.66\alpha) : (1.93 + 0.19\alpha) : (5.87 - 1.76\alpha). \quad (6.5)$$

The single parameter  $\alpha$  can be varied continuously so as to study how non universalities in the gaugino sector will be revealed at the LHC. Model lines will be constructed using small ranges  $0 \leq \alpha \leq 1$  and the resulting collider signatures will be investigated for two specific benchmark models described next.

Parameter	Point A	Point B	Parameter	Point A	Point B
$\alpha$	0.3	1.0	$m_{Q_3}^2$	$(1507)^2$	$(430.9)^2$
$m_{3/2}$	1.5 TeV	16.3 TeV	$m_{U_3}^2$	$(1504)^2$	$(610.3)^2$
$M_1$	198.7	851.6	$m_{D_3}^2$	$(1505)^2$	$(352.2)^2$
$M_2$	172.1	553.3	$m_{L_3}^2$	$(1503)^2$	$(381.6)^2$
$M_3$	154.6	339.1	$m_{E_3}^2$	$(1502)^2$	$(407.9)^2$
$A_t$	193.0	1309	$m_{Q_{1,2}}^2$	$(1508)^2$	$(208.4)^2$
$A_b$	205.3	1084	$m_{U_{1,2}}^2$	$(1506)^2$	$(302.7)^2$
$A_\tau$	188.4	1248	$m_{D_{1,2}}^2$	$(1505)^2$	$(347.0)^2$
$m_{H_u}^2$	$(1500)^2$	$(752.0)^2$	$m_{L_{1,2}}^2$	$(1503)^2$	$(379.8)^2$
$m_{H_d}^2$	$(1503)^2$	$(388.7)^2$	$m_{E_{1,2}}^2$	$(1502)^2$	$(404.5)^2$

Table 6.1: **Benchmark model soft term inputs.** High scale values of supersymmetry breaking soft terms at  $Q_{\text{GUT}} = 2 \times 10^{16}$  GeV. Both points are taken to have  $\mu > 0$  and  $\tan\beta = 10$  and all masses are given in GeV.

## 6.2 Benchmarks

Two distinct string based benchmark models will be considered around which to form  $\alpha$  lines. The first is from a class of heterotic string models studied in [171, 172, 166] with Kähler stabilization of the dilaton. This first benchmark model, labeled A, used here is from [173] and predicts a value of  $\alpha = 0.3$ . The second is from a class of Type IIB string theory with flux compactification as in KKLT [89]. This second benchmark model, labeled B, was studied in [87] and predicts a value of  $\alpha = 1$ . For further details on the benchmarks see appendix A of [164].

In Table 6.1 the high scale model inputs are given for each of the benchmark models. Both of the models considered are examples of the mirage pattern, although the predicted soft scalar masses are quite different. The unification scale of the gaugino masses are at  $Q_{\text{mir}} = 2.0 \times 10^{14}$  GeV for model A and at  $Q_{\text{mir}} = 1.5 \times 10^9$  GeV for model B. These soft terms are run down to the electroweak scale (here taken as 1 TeV) using **Suspect** [92] with the resulting low scale physical masses given later in Table 6.4. Two loop running was used for all but the gaugino masses so that the 1-loop results are still applicable for the gaugino mass parametrization in terms of  $\alpha$ . The resulting low scale models will be perturbed around

Object	Minimum $p_T$	Minimum $ \eta $
Photon	20 GeV	2.0
Electron	20 GeV	2.0
Muon	20 GeV	2.0
Tau	20 GeV	2.4
Jet	50 GeV	3.0

Table 6.2: **Initial cuts to keep an object in the event record.** After event reconstruction using PGS4 with L1 triggers we apply additional cuts listed to the individual objects in the event record. Detector objects which do not satisfy the above criteria are removed from the event record and do not enter our signature analysis.

the predicted value of  $\alpha$  and specific signatures will be used to determine the level of gaugino mass non-universality present in the model. In the next section the specific signature lists used will be introduced along with the criterion used for distinguishing between models with different values of  $\alpha$ .

### 6.3 Signature lists and distinguishing models

Here we provide a brief discussion about the distinguishability criterion and the signature lists used for studying the  $\alpha$  lines; for a thorough discussion see [164]. There are many possible signatures which may be considered at the LHC, and specific signatures were designed in [164] to track small changes in the  $\alpha$  parameter. This was done using many random low scale MSSM models with  $\alpha$  lines constructed.

There are three lists of signatures which were found and they were constructed to try to keep the correlations between the signatures small and hence the final state topologies are grouped according to

$$\begin{aligned}
 N_{\text{jets}} \leq 4 \text{ versus } N_{\text{jets}} \geq 5, \\
 N_{\text{leptons}} = 0 \text{ versus } N_{\text{leptons}} \geq 1.
 \end{aligned}
 \tag{6.6}$$

The signatures considered are built up from events from a simulation using PYTHIA [158] + PGS4 [159], where the level 1 (L1) triggers are imposed in PGS4. Following the L1 triggers object level cuts are imposed as in Table 6.2. Events passing the object level cuts are

furthermore required to have  $\cancel{E}_T > 150$  GeV, transverse sphericity  $S_T > 0.1$ , and  $H_T > 600$  GeV (400 GeV for events with 2 or more leptons) where  $H_T = \cancel{E}_T + \sum_{\text{Jets}} p_T^{\text{jet}}$ . The three signature lists constructed are given in Table 6.3.

**Signature List A**

	Description	Min Value	Max Value
1	$M_{\text{eff}}^{\text{any}} = \cancel{E}_T + \sum_{\text{all}} p_T^{\text{all}}$ [All events]	1250 GeV	End

**Signature List B**

	Description	Min Value	Max Value
1	$M_{\text{eff}}^{\text{jets}}$ [0 leptons, $\geq 5$ jets]	1100 GeV	End
2	$M_{\text{eff}}^{\text{any}}$ [0 leptons, $\leq 4$ jets]	1450 GeV	End
3	$M_{\text{eff}}^{\text{any}}$ [ $\geq 1$ leptons, $\leq 4$ jets]	1550 GeV	End
4	$p_T$ (Hardest Lepton) [ $\geq 1$ lepton, $\geq 5$ jets]	150 GeV	End
5	$M_{\text{inv}}^{\text{jets}}$ [0 leptons, $\leq 4$ jets]	0 GeV	850 GeV

**Signature List C**

	Description	Min Value	Max Value
Counting Signatures			
1	$N_\ell$ [ $\geq 1$ leptons, $\leq 4$ jets]		
2	$N_{\ell+\ell^-}$ [ $M_{\text{inv}}^{\ell+\ell^-} = M_Z \pm 5$ GeV]		
3	$N_B$ [ $\geq 2$ B-jets]		
[0 leptons, $\leq 4$ jets]			
4	$M_{\text{eff}}^{\text{any}}$	1000 GeV	End
5	$M_{\text{inv}}^{\text{jets}}$	750 GeV	End
6	$\cancel{E}_T$	500 GeV	End
[0 leptons, $\geq 5$ jets]			
7	$M_{\text{eff}}^{\text{any}}$	1250 GeV	3500 GeV
8	$r_{\text{jet}}$ [3 jets $> 200$ GeV]	0.25	1.0
9	$p_T$ (4th Hardest Jet)	125 GeV	End
10	$\cancel{E}_T/M_{\text{eff}}^{\text{any}}$	0.0	0.25
[ $\geq 1$ leptons, $\geq 5$ jets]			
11	$\cancel{E}_T/M_{\text{eff}}^{\text{any}}$	0.0	0.25
12	$p_T$ (Hardest Lepton)	150 GeV	End
13	$p_T$ (4th Hardest Jet)	125 GeV	End
14	$\cancel{E}_T + M_{\text{eff}}^{\text{jets}}$	1250 GeV	End

Table 6.3: **Signature Lists.**

Signature list A was found to be the best single signature to differentiate models with different values of  $\alpha$  and is built from the effective mass of everything in an event

$$M_{\text{eff}}^{\text{any}} = \cancel{E}_T + \sum_{\text{all}} p_T^{\text{all}}, \quad (6.7)$$

integrated over a specific range from 1250 GeV on up. The single signature in list A is sensitive to mass differences between the gluino and the lighter electroweak gauginos, and

these mass gaps are governed by changes in  $\alpha$ . In fact many of the signatures considered in Table 6.3 are kinematic distributions which are integrated over specific ranges. For list A no partitioning of the data is performed, while for lists B and C partitioning of the data is performed according to equation (6.6). Signature list B contains signatures which are correlated to the less than 10% level, while list C contains signatures which are correlated at a level of 30% or less. Furthermore list C contains the first examples of true counting signatures. List C also contains some normalized signatures, such as  $r_{\text{jet}}$  defined as

$$r_{\text{jet}} \equiv \frac{p_T^{\text{jet3}} + p_T^{\text{jet4}}}{p_T^{\text{jet1}} + p_T^{\text{jet2}}}. \quad (6.8)$$

Given the signatures listed in Table 6.3 we now turn to how to use them to tell apart the same base model along the  $\alpha$  lines based on [164]. The distinguishability criterion of two models is based on signature lists with  $n$  signatures and separated to a confidence level  $p$ . The models will be separated to a confidence level  $p$  with a 95% probability that the models are truly different using  $n$  uncorrelated signatures after a minimum amount of luminosity according to

$$L_{\min}(p) = \frac{\lambda_{\min}(n, p)}{R_{AB}}. \quad (6.9)$$

The criterion in equation (6.9) involves the use of the non-central chi-square distribution, with non-centrality parameter  $\lambda(n, p)$ , which is a calculable quantity given  $n$  and  $p$ . For example the relevant values of this parameter for lists A and B at the  $p = 95\%$  confidence level are  $\lambda(1, 0.95) = 12.99$  and  $\lambda(5, 0.95) = 19.78$ . The quantity  $R_{AB}$  in equation (6.9) contains the physics of models  $A$  and  $B$  and is given by

$$R_{AB} = \sum_i (R_{AB})_i = \sum_i \frac{(\sigma_i^A - \sigma_i^B)^2}{\sigma_i^A + \sigma_i^B} \quad (6.10)$$

where the sum is over the number of signatures  $n$  considered. The value of the cross sections are  $\sigma_i = N_i/L$ , where  $N_i$  is the number of events for signature  $i$  and  $L$  is the luminosity

Parameter	Point A	Point B	Parameter	Point A	Point B
$m_{\tilde{N}_1}$	85.5	338.7	$m_{\tilde{t}_1}$	844.7	379.9
$m_{\tilde{N}_2}$	147.9	440.2	$m_{\tilde{t}_2}$	1232	739.1
$m_{\tilde{N}_3}$	485.3	622.8	$m_{\tilde{e}_L}, m_{\tilde{u}_L}$	1518	811.7
$m_{\tilde{N}_4}$	494.0	634.3	$m_{\tilde{e}_R}, m_{\tilde{u}_R}$	1520	793.3
$m_{\tilde{C}_1^\pm}$	147.7	440.1	$m_{\tilde{b}_1}$	1224	676.8
$m_{\tilde{C}_2^\pm}$	494.9	635.0	$m_{\tilde{b}_2}$	1507	782.4
$m_{\tilde{g}}$	510.0	818.0	$m_{\tilde{s}_L}, m_{\tilde{d}_L}$	1520	815.4
$\mu$	476.1	625.2	$m_{\tilde{s}_R}, m_{\tilde{d}_R}$	1520	793.5
$m_h$	115.2	119.5	$m_{\tilde{\tau}_1}$	1487	500.4
$m_A$	1557	807.4	$m_{\tilde{\tau}_2}$	1495	540.4
$m_{H^0}$	1557	806.8	$m_{\tilde{\mu}_L}, m_{\tilde{e}_L}$	1500	545.1
$m_{H^\pm}$	1559	811.1	$m_{\tilde{\mu}_R}, m_{\tilde{e}_R}$	1501	514.6

Table 6.4: **Low energy physical masses for benchmark models.** Low energy physical masses (in units of GeV) are given at the scale 1 TeV. All points have  $\mu > 0$ .

used to generate the data. The cross sections also include estimates of the Standard Model background via  $\sigma_i = \sigma_i^{\text{SUSY}} + \sigma^{\text{SM}}$ . The SM backgrounds are based on the approach taken in the LHC Olympics [174] and further discussion is given in the Appendix 9. In what follows we will use  $p = 95\%$  and each of the signature lists in Table 6.3 to determine the minimum amount of luminosity required to separate a given benchmark model for different values of  $\alpha$ .

## 6.4 Benchmark model LHC analysis

The low scale physical masses in Table 6.4 are used as starting points for setting up  $\alpha$  lines. To do this the gaugino masses at the low scale are adjusted via equation (6.5) for  $0 \leq \alpha \leq 1$ . This is done so that the signatures introduced in the previous section can be studied which have been shown to be sensitive to changes in  $\alpha$ . The distinguishability methods previously introduced will be used to determine how much luminosity is required to separate  $\alpha = 0.3$  from  $\alpha = 1$ , for example.

Prior to looking into how well the signature lists can track changes in  $\alpha$  it is useful to

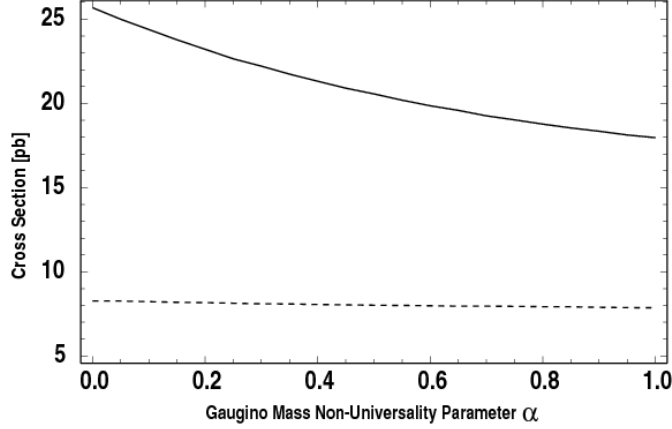


Figure 6.1: Total cross sections for model A (solid) and model B (dashed) along the  $\alpha$  line.

look into some important properties of the benchmark models. First we can consider the total SUSY cross sections at the LHC which are shown in Figure 6.1. Model A (solid line) has heavy squarks with mass around 1.5 TeV, but it has a lighter gluino of 510 GeV and hence has the larger cross section compared to Model B (dashed line). For both models the cross sections diminish for larger values of  $\alpha$  and essentially the only important changes as one varies  $\alpha$  are the masses of  $\tilde{N}_1$ ,  $\tilde{N}_2$ , and  $\tilde{C}_1$  which grow larger as  $\alpha$  increases. The three largest SUSY subprocess cross sections at a few points along the  $\alpha$  line are given in Table 6.5. Model B has a light stop whose production is a dominant mode along the  $\alpha$  line with

$\alpha$	model A		model B	
	mode	$\sigma$ [pb]	mode	$\sigma$ [pb]
0.0	$gg \rightarrow \tilde{g}\tilde{g}$	13.4	$qg \rightarrow \tilde{q}_R\tilde{g}$	1.6
	$q\bar{q}' \rightarrow \tilde{N}_2\tilde{C}_1$	6.2	$qg \rightarrow \tilde{q}_L\tilde{g}$	1.5
	$q\bar{q} \rightarrow \tilde{C}_1\tilde{C}_1$	3.2	$gg \rightarrow \tilde{t}_1\tilde{t}_1$	1.5
0.3	$gg \rightarrow \tilde{g}\tilde{g}$	13.4	$qg \rightarrow \tilde{q}_R\tilde{g}$	1.6
	$q\bar{q}' \rightarrow \tilde{N}_2\tilde{C}_1$	4.0	$qg \rightarrow \tilde{q}_L\tilde{g}$	1.5
	$q\bar{q} \rightarrow \tilde{C}_1\tilde{C}_1$	2.0	$gg \rightarrow \tilde{t}_1\tilde{t}_1$	1.5
1.0	$gg \rightarrow \tilde{g}\tilde{g}$	13.4	$qg \rightarrow \tilde{q}_R\tilde{g}$	1.6
	$q\bar{q}' \rightarrow \tilde{g}\tilde{g}$	1.4	$qg \rightarrow \tilde{q}_L\tilde{g}$	1.5
	$q\bar{q} \rightarrow \tilde{C}_1\tilde{C}_1$	1.2	$gg \rightarrow \tilde{t}_1\tilde{t}_1$	1.5

Table 6.5: Dominant production SUSY subprocess cross sections for the benchmark models.

the other modes staying mostly constant as one changes  $\alpha$ .

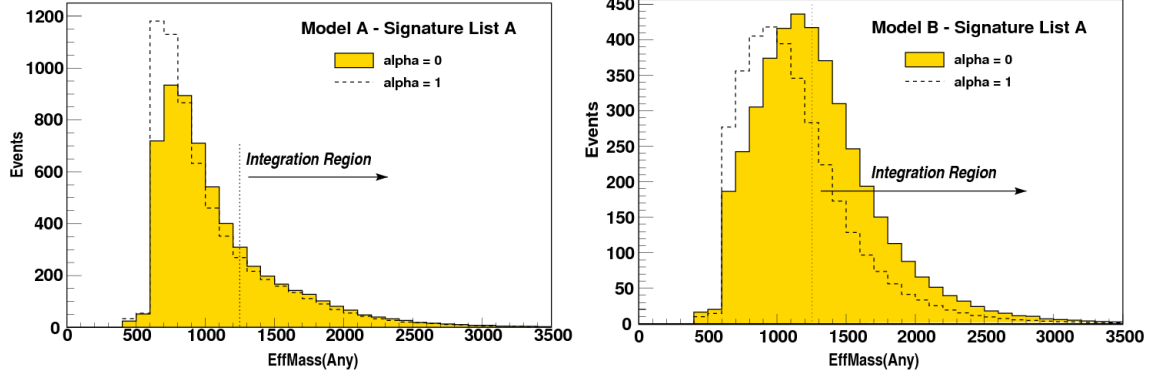


Figure 6.2: **Benchmark model distributions of  $M_{\text{eff}}^{\text{any}}$  from signature List A.** The left panel is model A and the right panel is model B. The solid filled histogram is the case for  $\alpha = 0$  and dotted histogram is the case for  $\alpha = 1$ . The lower bound for the integration region is indicated by the dotted line at 1250 GeV. The sharp lower bound in the distribution is an artifact of the event-level cuts imposed on the data using L1 triggers in PGS.

Moving on we now consider the effective mass distributions for the two benchmark models. These are shown in Figures 6.2 with the integration region marked which is relevant for computing the  $M_{\text{eff}}^{\text{any}}$  value of signature list A. The distributions are quite different between the two cases. Model A shows little change above the integration region between  $\alpha = 0$  and 1, while model B shows much more change. Model A produces mostly gluinos which decay via three body decays to lighter electroweak gauginos and quarks. These decays remain mostly constant across the  $\alpha$  line and the effective mass distribution essentially tracks the production and decay of the gluino. In the case of model B the effective mass distribution tracks the production and decays of the gluinos and squarks which have more substantial decays changing along the line and hence the  $M_{\text{eff}}^{\text{any}}$  variable is more interesting.

After gaining a bit of familiarity with the variable considered in signature list A we now consider the minimum luminosity required to separate the models using the three signature lists. The procedure is as described earlier in Section 6.3 where the quantities  $R_{AB}$  are computed for two points on an  $\alpha$  line for the same benchmark model. Upon then using the necessary value for  $\lambda(n, 0.95)$  for a signature list of  $n$  signatures one can then compute the minimum luminosity required to say the two model points have a probability of 95% of

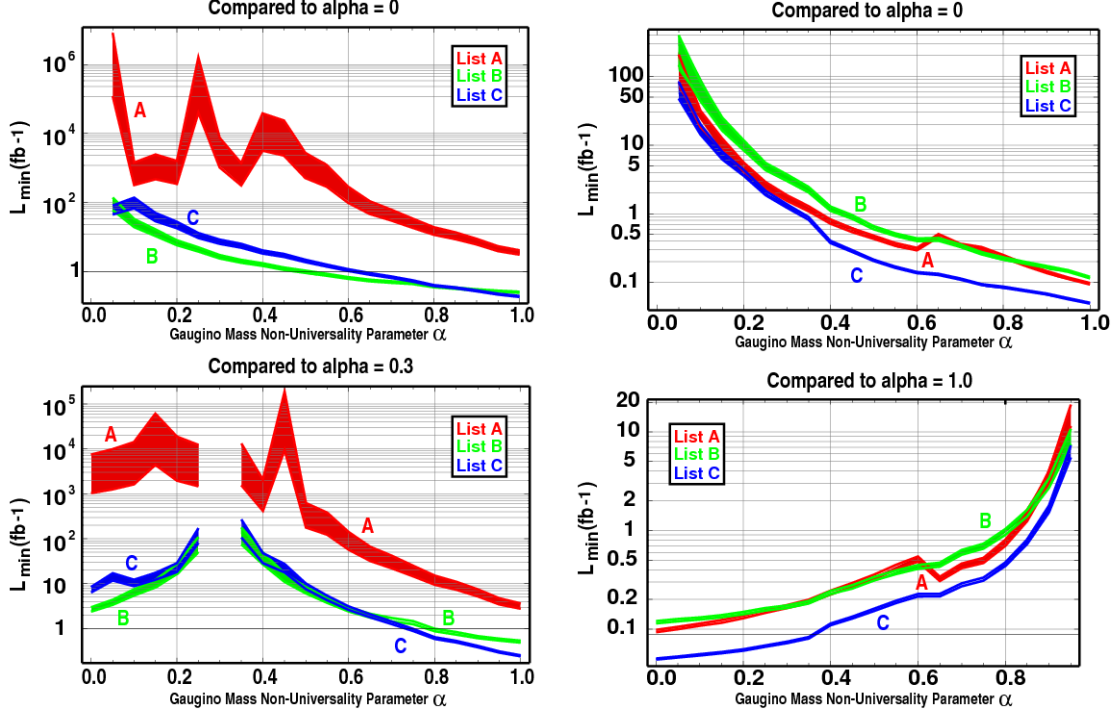


Figure 6.3:  $L_{\min}$  as a function of  $\alpha$  for the benchmark models. The three shaded regions correspond to the three signature lists as indicated in the legend. The lower bound of each shaded region indicates the minimum integrated luminosity  $L_{\min}$  needed to separate the model with the specified  $\alpha$  from  $\alpha = 0$  (top panels) or the predicted value of  $\alpha$  (lower panels). The upper bound of the shaded region represents an estimate of the 1 sigma upper bound on the calculated value of  $L_{\min}$  caused by statistical fluctuations.

being different models at a confidence level of 95%. The results of the calculations for both benchmark models using the three signature lists given in Table 6.3 are shown in Figure 6.3. Using the distinguishability criterion, a base model corresponding to one point along an  $\alpha$  line for both of the benchmarks is chosen. In the upper panel of Figure 6.3 we use the base model point for both benchmarks as the  $\alpha = 0$  point. In the lower panel the base model is chosen as the predicted value of  $\alpha$  from the theory which is  $\alpha = 0.3$  for model A and  $\alpha = 1$  for model B. All of the signature lists save for list A for model A do a good job of distinguishing points along the  $\alpha$  lines for both benchmark models.

Looking at the results in Figure 6.3 one can see that the signature list A does a good job for model B, but not for model A. This is expected based on the distributions of  $M_{\text{eff}}^{\text{any}}$

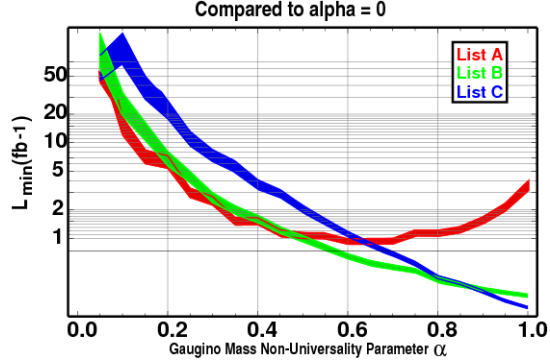


Figure 6.4:  $L_{\min}$  as a function of  $\alpha$  for benchmark model A with relaxed lower bound on  $M_{\text{eff}}^{\text{any}}$ . The three shaded regions correspond to the three signature lists as in the upper left panel of Figure 6.3. In this case the lower bound of the integration range for the single observable of List A has been relaxed to 500 GeV.

as shown in Figure 6.2, where model B showed large differences between  $\alpha = 0$  and  $\alpha = 1$  above the integration boundary, while model A did not. The small fluctuations in the count rates for this signature in model A results in instability in computing the  $L_{\min}$  values along the  $\alpha$  line. The signature lists that are used here were optimized over a large set of randomly chosen base models for which  $\alpha$  lines were then created. Model B is similar to the types of random models chosen for the optimization, whereas model A is not similar to the random models and hence it is an example for which the optimization will not work. Had the random models been chosen so as to include the type of model which represents model A then the optimization likely would have found a better signature to use. For example looking at Figure 6.2, model A does show the most difference in the distribution at smaller values of  $M_{\text{eff}}$  and if the integration region was chosen differently the results can get better. As a demonstration of this in Figure 6.4 we show the same figure as in the upper left panel of Figure 6.3 but with the lower bound of integration for  $M_{\text{eff}}^{\text{any}}$  of 500 GeV. Relaxing the lower bound to 500 GeV clearly increases the utility of list A for model A.

Looking at the left panels of Figure 6.3 also shows that the largest signature list C is not able to distinguish models along the  $\alpha$  line using the least amount of integrated luminosity. List B in this case is able to distinguish points along the line using the least amount of data.

For this model the jet invariant mass variables in both lists as well as the normalized  $\cancel{E}_T$  signatures and  $p_T(\text{jet}, 4)$  observable of list C are more sensitive to the changes in  $\alpha$  than the single variable of list A. In this case the largest possible signature list is not the most effective at tracking changes in  $\alpha$  as most of the signatures in list C are not very helpful. Model A again does not reflect the random models chosen for the optimization and as a result many of the signatures in list C are not effective in tracking the variations associated with changes in  $\alpha$  for this model.

Moving on to benchmark model B we see in Figure 6.3 that all of the lists do pretty well to distinguish points along the  $\alpha$  line. This model is a good example for which to understand the utility of the various signatures in the three lists and how they track important properties which vary along the  $\alpha$  line. The sparticle spectrum for this model is richer than the case of model A and many important thresholds are crossed as one moves along the  $\alpha$  line. As has been mentioned already list A does a good job in this case at distinguishing points along the  $\alpha$  line which is expected based on the distribution of  $M_{\text{eff}}^{\text{any}}$  shown in Figure 6.3. In this case signature list C is the most effective at distinguishing points along the  $\alpha$  line as most of the signatures in the list contribute to distinguishing points along the line. List B does a good job at distinguishing points also and it is easier to consider the 5 signatures in the list and what properties of the model cause the signatures to be so effective.

Still considering model B it is useful to look at some of the important branching fractions which change along with the individual  $(R_{AB})_i$  values. Considering the signatures in list B we plot each of the 5  $(R_{AB})_i$  values as a function of  $\alpha$  in Figure 6.5 where the base model is chosen to be the model point with  $\alpha = 0$ . As one moves away from  $\alpha = 0$  the signatures clearly show separation as each of the individual  $(R_{AB})_i$  values grow, thus contributing to the overall lowering of the necessary  $L_{\text{min}}$  needed to distinguish points along the  $\alpha$  line. The two most powerful signatures for this model are signature 1 and 5 of list B which are given in the left panel of Figure 6.5, with the other three signatures shown in the right panel. To understand what causes some of the signatures to change as they do we can look at the

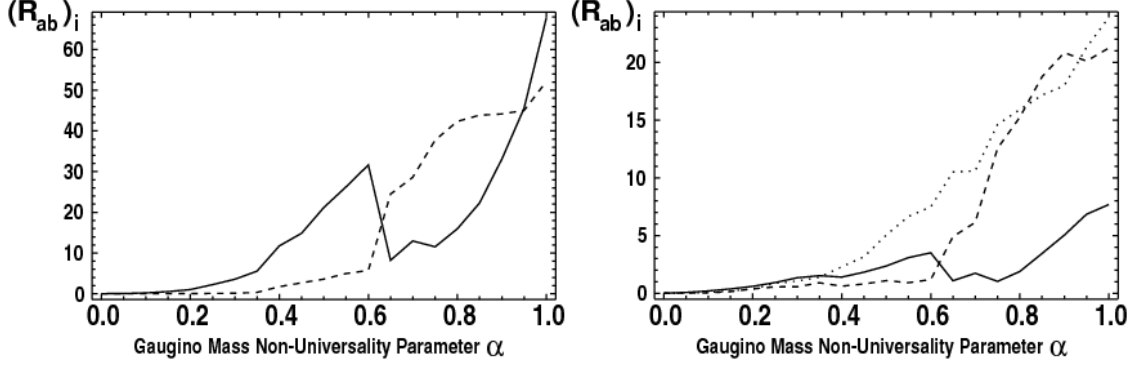


Figure 6.5: Values of  $(R_{AB})_i$  for the five signatures of List B as a function of  $\alpha$  for benchmark model B. The ability of each individual signature from List B to resolve the case  $\alpha = 0$  from the indicated value of  $\alpha$  is given by the height of the curve  $(R_{AB})_i$  in the above plots. In the left panel we display signature 1 (solid curve) and signature 5 (dashed curve). In the right panel we display signature 2 (solid curve), signature 3 (dashed curve) and signature 4 (dotted curve).

decays of the light stop which is one of the dominantly produced superpartners with the decays shown in the left panel of Figure 6.6.

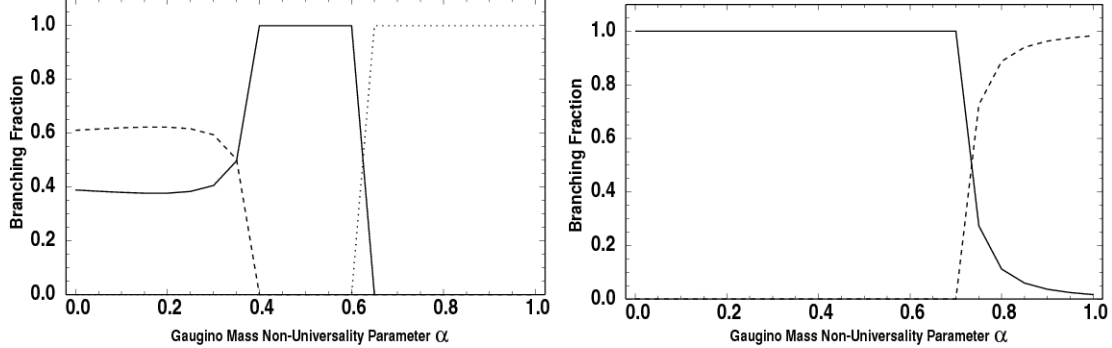


Figure 6.6: Branching fractions for principal decay modes of lightest stop (left panel) and lightest chargino (right panel) as a function of  $\alpha$  for benchmark model B. In the left panel the decay modes are  $\tilde{t}_1 \rightarrow \tilde{N}_1 t$  (dashed curve),  $\tilde{t}_1 \rightarrow \tilde{C}_1 b$  (solid curve), and  $\tilde{t}_1 \rightarrow \tilde{N}_1 c$  (dashed curve). In the right panel the decay modes are  $\tilde{C}_1 \rightarrow \tilde{N}_1 W$  (solid curve) and  $\tilde{C}_1 \rightarrow \tilde{t}_1 \bar{b}$  (dashed curve).

For smaller values of  $\alpha \lesssim 0.35$  the stop decays mostly to  $\tilde{N}_1 t$  as well as  $\tilde{C}_1 b$ , as the  $\tilde{N}_1$  and  $\tilde{C}_1$  are sufficiently light. The decay to light charginos drops off first at  $\alpha = 0.4$  as it becomes too massive to be a decay product and the lightest neutralino decay with a bottom

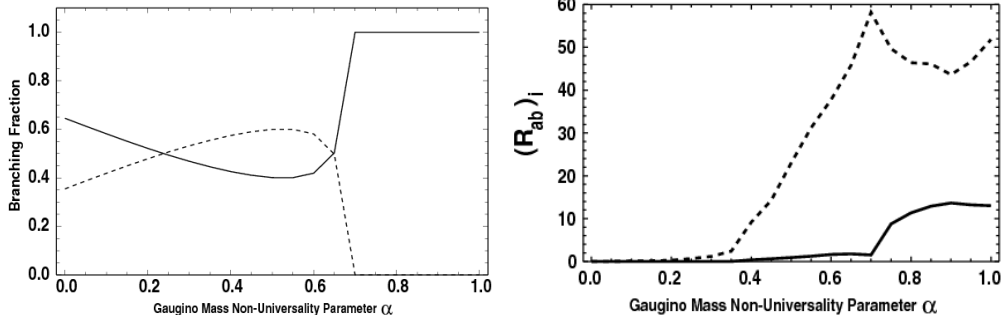


Figure 6.7: **Branching fraction for next-to-lightest neutralino (left) and  $(R_{AB})_i$  values for key counting signatures from List C (right).** The branching fraction of the next-to-lightest neutralino  $\tilde{N}_2$  for benchmark model B is plotted as a function of  $\alpha$  in the left panel. The decay modes are  $\tilde{N}_2 \rightarrow \tilde{N}_1 h$  (dashed curve) and  $\tilde{N}_2 \rightarrow \tilde{N}_1 Z$  (solid curve). In the right panel the  $(R_{AB})_i$  values for the opposite sign leptons from  $Z$  decays counting signature (signature 2 – solid curve) and the inclusive B-jet counting signature (signature 3 – dashed curve) are plotted as function of  $\alpha$ .

quark drops off at  $\alpha = 0.65$  as it becomes too massive. About half of the time the  $W$  decays from the  $t$  will decay hadronically and hence help populate the jet variables in list B. For values of  $\alpha \gtrsim 0.6$  the dominant decay mode of the stop is  $\tilde{N}_1 c$ . The right panel of Figure 6.6 shows the decays of the light chargino which decays purely to  $\tilde{N}_1 W$  up to  $\alpha = 0.7$  when the decay mode  $\tilde{t}_1 \bar{b}$  opens up as the chargino becomes more massive. All of these various decays contribute to the various signatures considered in list B.

It is also useful to consider a few of the signatures from list C which track some important properties of model B along the  $\alpha$  line. For this we consider the signatures 2 and 3 of list C which are plotted against  $\alpha$  in Figure 6.7 along with the decays of the second lightest neutralino. These signatures are related to the “spoiler” modes for the trilepton signal and essentially count on-shell  $Z$  and  $h$  boson decays. In this figure we have shown two of the simpler variables from list C which are both affected by the decays of  $\tilde{N}_2$  which decays to both  $\tilde{N}_1 Z$  and  $\tilde{N}_1 h$  for values of  $\alpha \lesssim 0.7$  and after  $\alpha = 0.7$  only the decay of  $\tilde{N}_2$  to  $\tilde{N}_1 h$  is allowed. In this model the  $h$  decays about 70% of the time to  $b\bar{b}$ , while the  $Z$  decays to  $\ell\bar{\ell}$  about 10% and  $b\bar{b}$  about 15% of the time. One can readily see the correlation between the effectiveness of these spoiler mode signatures and the daughters produced from the  $\tilde{N}_2$

decays. Similar arguments can be made using the superpartner decays for the various other signatures in the lists.

## 6.5 Summary

In this chapter we have discussed in some detail the LHC phenomenology of an example of non-universal gaugino masses. Two string-motivated benchmark models were used as base models by which small perturbations on the non-universality parameter  $\alpha$  were performed to study the resulting LHC signatures. Using specific signature lists which were constructed to efficiently track the variations in  $\alpha$  we have shown that these targeted observables can determine non-universalities in the gaugino sector using a minimum amount of integrated luminosity. When taking the universal case as the point of reference the signature lists can reveal the presence of non-universalities of  $\alpha \gtrsim 0.2$  using 10-20  $fb^{-1}$  of LHC data for the benchmark models. If the predicted values of  $\alpha$  are used for the benchmarks then a similar statement holds when one moves more than 0.2 in  $\alpha$  away from the predicted value.

# Chapter 7

## Lifting model degeneracies in LHC data using dark matter observations

The previous chapters have focused on both dark matter and collider signatures of non-universal gaugino masses. Other than suggesting possible correlations between the dark matter and collider signatures in Chapter 5 the two experimental arenas have been mostly separate. In this final chapter we investigate how dark matter signatures can help alleviate possible model degeneracies which can arise in LHC data. This serves as a study of the complementarity of both LHC and dark matter data and how it can be used to help understand which SUSY models are good fits to data.

### 7.1 LHC inverse problem

If BSM physics is established at the LHC the community will be faced with the task of reconstructing an underlying theoretical framework. Under the assumption that the BSM physics is SUSY, in [175] the authors argue that within a reduced 15 dimensional parameter space of the MSSM many possible candidate models may give rise to indistinguishable signatures at the LHC. Sets of parameters may have many pairs of “degenerate twins” which give similar fits to the data and how to differentiate these degenerate models is the LHC inverse problem. The degenerate pairs discovered in [175] are used as the basis for a study on the ability to separate the degenerate models using observations from dark matter experiments.

We now give a brief description of how the models were simulated and then deemed degenerate in [175]. These degenerate pairs were the result of simulating  $10fb^{-1}$  of LHC

data for over 43,000 points within the MSSM. These points were defined at the weak scale via the 15 parameters

$$\left\{ \begin{array}{c} \tan \beta, \mu, M_1, M_2, M_3 \\ m_{Q_{1,2}}, m_{U_{1,2}}, m_{D_{1,2}}, m_{L_{1,2}}, m_{E_{1,2}} \\ m_{Q_3}, m_{U_3}, m_{D_3}, m_{L_3}, m_{E_3} \end{array} \right\}, \quad (7.1)$$

while holding fixed  $m_A = 850$  GeV,  $A = 800$  GeV for third generation squarks and  $A = 0$  GeV for all others. For the LHC simulations PYTHIA [158] + PGS4 [159] was used and no Standard Model background was used. Two classes of LHC signatures were considered to describe the data: simple counting signatures of final state topologies and shapes of kinematic distributions of final state decay products. The distributions were parametrized so as to be able to be combined into a  $\chi^2$ -like variable. In all 1808 signatures  $s_i$  were used to classify each SUSY model.

The authors of [175] grouped the  $s_i$  values into a  $\chi^2$ -like variable,

$$(\Delta S_{AB})^2 = \frac{1}{N_{\text{sig}}} \sum_i \left( \frac{s_i^A - s_i^B}{\sigma_i^{AB}} \right)^2, \quad (7.2)$$

where  $A$  and  $B$  represent two different models,  $N_{\text{sig}}$  is the total number of signatures considered and  $\sigma_i^{AB}$  is a measure of the error associated with the  $i$ -th signature

$$\sigma_i^{AB} = \sqrt{(\delta s_i^A)^2 + (\delta s_i^B)^2 + \left( f_i \frac{s_i^A + s_i^B}{2} \right)^2}. \quad (7.3)$$

Invariably some SM background may remain in the data samples and the quantity  $f_i$  represents the error associated with this. A value of  $f_i = 0.01$  was used for individual signatures while  $f_i = 0.15$  was used for the overall event rate. In this way equation (7.2) represents a metric on the signature space of models. To determine whether two models are distinct using  $(\Delta S_{AB})^2$  the *same* model was simulated many times and the 95th percentile of

the distribution of  $(\Delta S_{AB})^2$  values was used as a lower bound for distinguishing models,  $(\Delta S_{AB})^2|_{95\text{th}} = 0.285$ . In other words if two distinct models gave  $(\Delta S_{AB})^2 < 0.285$  they were considered degenerate.

Of the over 43,000 models considered using the separability criterion 283 pairs of these models were deemed indistinguishable using the criterion outline above. These 283 pairs were comprised of 384 individual sets of input parameters which we were provided by the authors of [175]. Using the same method for LHC simulation, 50k events were generated and a smaller sample of 36 signatures were considered by which it was deemed that the pairs were indeed degenerate using a separation criterion of  $(\Delta S_{AB})^2|_{95\text{th}} = 0.63$ .

These same degenerate pairs were recently studied by [176, 177], where the authors looked at the utility of the international linear collider (ILC) in distinguishing the models. A general conclusion of this study is that if the charged superpartners were kinematically accessible they were usually detectable above Standard Model backgrounds, while if only neutral superpartners were accessible then the models were usually not detectable. If one or both degenerate models had an accessible and visible charged superpartner they were generally distinguishable at a 500 GeV linear collider. The result is that 57 (63) model pairs were distinguishable at the  $5\sigma$  ( $3\sigma$ ) level. If the center of mass energy is increased to 1 TeV, then many more pairs can be distinguished as the degenerate models generally have relatively higher mass lighter gaugino states.

It is important to note here that  $(\mu, M_1, M_2, M_3)$  and  $\tan\beta$  are varied randomly resulting in non-universal gaugino sectors of the models. That dark matter observables can help lift LHC degeneracies is of no surprise as the signals are sensitive to the make-up of the LSP, of which LHC signals are much less so. Here we outline the utility of dark matter observables to lift LHC degeneracies following [178].

## 7.2 Classifying degenerate pairs

Before proceeding to the dark matter observables of the models there are a few basic properties which will be addressed. To calculate the mass spectrum of the degenerate pairs `PYTHIA` was used to compute the tree-level masses and mixings. When this is done the lightest chargino can sometimes be slightly lighter than the lightest neutralino and to approximate the radiative correction `PYTHIA` adds twice the neutral pion mass. In the initial model set 149 of the 384 models had just such an issue, which caused these model points to be jettisoned by the ILC study. In contrast these points are kept for the dark matter observables as the small mass gap only affects the calculation of the thermal relic density of the lightest neutralino.

The thermal relic density is an important cosmological quantity which is related in an indirect way to dark matter calculations relevant for interpreting observations. The local halo density of neutralinos is important to the observables that are considered and the relationship between it and the thermal relic density is not so precise. The relic density is a highly sensitive calculation of masses and mixings from the SUSY model as well as SM inputs and furthermore the assumptions governing the calculation are not well understood. In moving forward with the analysis we will be unbiased about the predicted thermal relic abundance and display results both utilizing the relic calculation and not. It is understood that the model points under study may well be replaced with a similar model set whose points have a sensible value of the relic density while remaining degenerate at the LHC.

Using the low scale model input parameters we use the computer package `DarkSUSY` [58] to compute the thermal relic density. Of the 384 models originally considered 6 gave a  $\tilde{\tau}_1$  LSP with the spectrum computed in `DarkSUSY`. To continue we demand that the LSP be the  $\tilde{N}_1$  and so we drop these 6 models and continue with 378 models. The resulting values for the degenerate models are shown in Figure 7.1. The horizontal lines bound the three year

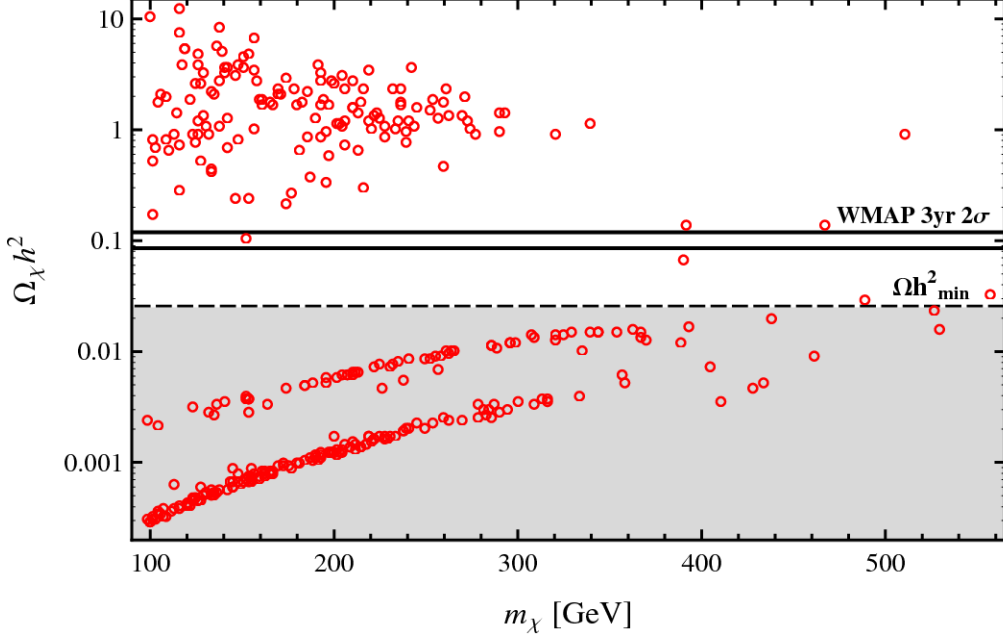


Figure 7.1: **Thermal relic abundance of neutralino LSPs for the 378 models from [175].** Prediction for the thermal relic abundance  $\Omega_\chi h^2$ , as computed by DarkSUSY, plotted as a function of the LSP mass  $m_\chi$ . The solid horizontal lines indicate the  $2\sigma$  band favored by the WMAP three-year data. The region below the horizontal dashed line represents those models where the local density of neutralinos should be rescaled.

$2\sigma$  WMAP favored value [98]

$$0.0855 < \Omega_\chi h^2 < 0.1189. \quad (7.4)$$

Of the 378 models only 1 lies within WMAP range, 145 are above the upper value and 232 fall below the lower bound. Of the 232 models below the lower bound 224 have  $\Omega_\chi h^2 \leq 0.025$ . We will consider all 378 models regardless of the  $\Omega_\chi h^2$  values and group the pairs who have  $\Omega_\chi h^2 > 0.1189$  separately. For models who have  $\Omega_\chi h^2 < 0.025$  we will rescale the local halo density of  $\rho_\chi = 0.3 \text{ GeV/cm}^3$  by the multiplicative factor  $r_\chi = \text{Min}(1, \Omega_\chi h^2/0.025)$  as in equation (3.10). Results will be shown in which the rescaling is done as well as for which no rescaling is done.

As further classification of the model pairs we consider the bounds on the light Higgs mass as well as indirect constraints. Bounds on  $m_h$ ,  $\text{Br}(b \rightarrow s\gamma)$  and the SUSY contribution

to the anomalous magnetic moment of the muon from [151] are

$$\begin{aligned}
 m_h &\geq 114.4 \text{ GeV} \\
 2.65 \times 10^{-4} &\leq \text{Br}(b \rightarrow s\gamma) \leq 4.45 \times 10^{-4} \\
 a_\mu|_{\text{SUSY}} &\leq 4.7 \times 10^{-9}.
 \end{aligned}
 \tag{7.5}$$

Of the 378 models considered 43 violate the  $m_h$  bound, 101 violate the  $b \rightarrow s\gamma$  bound and 6 violate the  $a_\mu$  bound. These constraints are not so important for the dark matter signatures we consider and so we will consider all 378 models moving forward, but they will be grouped according to the value of  $\Omega_\chi h^2$  as well as the bounds given in equation (7.5). A subset of 127 models (77 degenerate pairs) is deemed “physical” if they have  $\Omega_\chi h^2 < 0.1189$  and satisfy all three constraints in equation (7.5). Furthermore the results of the ILC study of [176, 177] are considered to compare how well the dark matter observations can complement in model distinguishability. To estimate which models would be distinguishable at the ILC we simply require a charged superpartner be kinematically accessible at  $\sqrt{s} = 500$  GeV and use a conservative estimate of 240 GeV in mass to be visible. Using this estimate 190 models are deemed visible of which 68 have no chargino mass warning from PYTHIA<sup>1</sup>. This initial division of the 378 models is given in Table 7.1.

The assumptions going forward are that several years of data taking and subsequent analysis has been performed using a broad set of global observables as in the previous chapter or as in [175]. The values of the superpartner masses will not be assumed to be known here so as to truly be model independent. Furthermore we assume that a fit has been performed in which many degenerate model pairs can fit the data equally well. To proceed we take these models as inputs and look at the resulting dark matter signatures and whether degenerate models may be separated.

---

<sup>1</sup>The physical gaugino masses are computed at the tree level in PYTHIA and sometimes the lightest chargino is slightly lighter than the lightest neutralino. PYTHIA fixes this problem by making the lightest chargino mass to be twice the neutral pion mass plus the lightest neutralino mass. In models where this happens PYTHIA issues a warning flag.

	Models	Pairs
Initial Set	378	276
PYTHIA chargino warnings	149	124
Relic Density		
$\Omega_\chi h^2 > 0.1189$	145	116
$\Omega_\chi h^2 < 0.0250$	224	164
Additional Constraints		
$m_h < 114.4$ GeV	43	52
$\text{Br}(b \rightarrow s\gamma) > 4.45 \times 10^{-4}$	101	98
$a_\mu _{\text{SUSY}} > 4.7 \times 10^{-9}$	6	6
Visible at 500 GeV ILC	190	173
Remove PYTHIA chargino warnings	68	65
All Physical Conditions Satisfied	127	77

Table 7.1: **Summary of global properties of the 378 models.** The column labeled “Models” gives the number of individual models which satisfy the given property. The column labeled “pairs” gives the number of model pairs where *at least one* of the two models in the pair satisfies the given property. If a model passes all of the tests listed in the table and has  $\Omega_\chi h^2 < 0.1189$  it is then counted in the last row. If *both* models in a degenerate pair pass the given tests and have  $\Omega_\chi h^2 < 0.1189$  then the pair is counted in the last row.

### 7.3 Direct detection

We begin by looking at the ability of direct detection experiments to differentiate the model pairs. The method for distinguishing model pairs involves comparing the two degenerate model inputs “A” and “B” and computing relevant dark matter signatures  $s_i$  for both models. To claim that an experiment can distinguish two model pairs we require both  $s_i^A$  and  $s_i^B$  to be detectable above background and that the values are sufficiently separated to have a statistically significant difference with respect to the error  $\sigma_i^{AB}$ . For the case of direct detection we consider a single type of observable: count rates.

The experiments which are considered are listed in Table 7.2 and are chosen for the reliability of background estimation and simplicity of presentation. All of the listed experiments have either cryogenic germanium bolometers or dual-phase liquid/gas xenon targets and hence mainly probe the spin-independent scattering of neutralinos with nucleons. For both target types at the time of this investigation the experiments listed in the upper portion of

Ref.	Experiment Name	Target	Mass (kg)	Detected Object(s)
[106]	CDMS II	Ge	3.75	ap, ic
[69]	XENON10	Xe	5.4	sp, ic
[179]	ZEPLIN II	Xe	7.2	sp, ic
[107]	SuperCDMS (Soudan)	Ge	7.5	see CDMS II
[107]	SuperCDMS (SNOLab)	Ge	27	see CDMS II
[107]	SuperCDMS (DUSEL)	Ge	1140	see CDMS II
[180]	EDELWEISS-2	Ge	9	ap, ic
[104]	XENON100	Xe	170	see XENON10
[181]	ZEPLIN III	Xe	8	see ZEPLIN II
[181]	ZEPLIN IV	Xe	1000	see ZEPLIN II

Table 7.2: **List of direct detection experiments considered.** The first three experiments listed (CDMS II, XENON10 and ZEPLIN II) have reported limits on neutralino-nucleon interaction rates. The masses given for these three experiments are the reported fiducial masses, while the masses for the other experiments are the nominal masses proposed. Detected objects are athermal phonons (ap), scintillation photons (sp) and ionization charge (ic).

the table have been operational with larger installations planned. The table lists the target types as well as the fiducial mass for currently running experiments and nominal masses for planned experiments. For the planned experiments the fiducial mass will be taken to be 80% of the nominal mass. The method of detecting the scattering events is also listed and is either via athermal phonons and/or ionization charge. The experiments which have already reported data give background estimations which we will extrapolate to the larger mass targets. Using the two target types of germanium and xenon we will present the resolving power of multiple experiments as a function of exposure (mass $\times$ time) on a given target.

An important property of a given model will be the spin-independent cross section for neutralino-nucleon scattering. Using the default nuclear form factors in **DarkSUSY** we compute  $\sigma_{\chi p}^{\text{SI}}$  according to equation (3.12) with the results shown in Figure 7.2. The points are grouped according to the value of the thermal relic abundance with:  $\Omega_{\chi}h^2 > 0.1189$  (darker filled triangles),  $0.025 < \Omega_{\chi}h^2 < 0.1189$  (lighter inverted triangles) and  $\Omega_{\chi}h^2 < 0.025$  (filled circles). Also shown are the reaches associated with some of the experiments listed in Table 7.2 with the lines labeled by the appropriate experiment. For the XENON10 and CDMS II

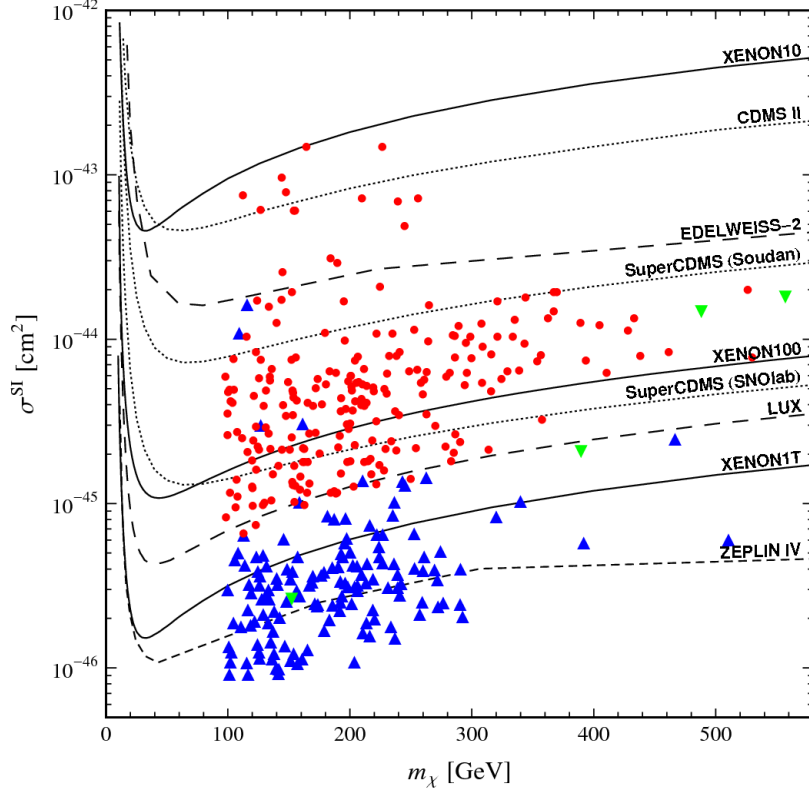


Figure 7.2: **Spin independent neutralino-proton interaction cross-section as a function of  $m_\chi$  for the 378 models.** The 378 models are divided into three groups: those with  $\Omega_\chi h^2 > 0.1189$  (darker filled triangles),  $0.025 < \Omega_\chi h^2 < 0.1189$  (lighter inverted triangles) and  $\Omega_\chi h^2 < 0.025$  (filled circles). Sensitivity curves for several of the experiments in Table 7.2 are overlaid on the plot with the curves taken from the web-based utility [182].

experiment the lines are the actual exclusion curves, while for the future experiments they are the range which is expected to be probed. The ZEPLIN II data is not shown as it is weaker, on the order of  $10^{-42} \text{ cm}^2$ .

Based on the cross sections shown in Figure 7.2, it seems that some of the models ought to have already been ruled out by direct detection experiments. Here it is argued that the plot is somewhat deceptive in this regard as the experiments do not measure the cross sections, rather they measure count rates of scattering events. The true relationship between the event rates and the cross sections involves further assumptions about the local density of relic neutralinos and the LSP velocity distribution. For the models considered here about 60% of the models have  $\Omega_\chi h^2 \leq 0.025$  – including all of the models whose cross sections are

above the XENON10 and CDMS II reach curves in Figure 7.2. If one rescales the models with  $r_\chi$  in equation (3.10) where necessary then *none* of the models give rates which should have been seen already, an example of why it is important to work with the count rates rather than using just the cross sections.

As described in Chapter 3 the interaction rates of the degenerate pairs are computed via integration of the interpolating function built by computing  $dR/dE$  from equation (3.15) in 0.5 keV intervals. The rates which are employed here reflect the range used by Xenon10 and CDMS II in equation (3.16) so that the targets are considered for ranges

$$\begin{aligned} R_1 & : 5 \text{ keV} \leq E_{\text{recoil}} \leq 25 \text{ keV} \\ R_2 & : 10 \text{ keV} \leq E_{\text{recoil}} \leq 100 \text{ keV}, \end{aligned} \tag{7.6}$$

with  $R_{\text{Xe}} = R_1$  and  $R_{\text{Ge}} = R_2$ . To compute the rates the default values of `DarkSUSY 4.1` are used here and for the rest of the analysis. Proceeding with the analysis we now discuss the expected background rates at the experiments considered.

The experiments considered all use similar background rejection methods involving the collection of ionization charge. There are essentially two types of backgrounds “true” and “fake” neutron recoils. The true background recoils happen when a neutron recoil occurs though not via interaction from a neutralino, e.g. neutron interacts with alpha particles or cosmic rays. These backgrounds can be reduced with proper shielding and by choosing a sufficiently deep experiment site. The fake recoils refer to when electric charge is collected in the correct time window with the other data signaling the recoil, but when the electric charge is induced from something other than the neutron recoil. These electron recoil backgrounds are harder to eliminate, but hopefully the necessary improvements can be made which are anticipated in the reach curves shown in Figure 7.2.

In what follows a single overall background figure will be used for each type of target. This is done so that one may use the entire collection of future experiments as an ensemble in

order to try to resolve degeneracies. Projections for large scale germanium-based detectors are for background event rates of no more than a few events per year of exposure. The liquid xenon detectors project a slightly higher rate, but still on the order of 10-20 events per year of exposure (mostly of the electron recoil variety). To be conservative, the following requirements are used on two potential signals  $s$  to proclaim them distinguishable:

1. The count rates for the two experiments ( $N_A$  and  $N_B$ ), obtained from integrating equation (3.15) over the appropriate range in equation (7.6), must *both* exceed  $N$  events when integrated over the exposure time considered. We will usually consider  $N = 100$ , but also show results for the weaker condition  $N = 10$ .
2. The two quantities  $N_A$  and  $N_B$  must differ by at least  $n\sigma^{AB}$ , where we will generally take  $n = 5$ .

The error term  $\sigma^{AB}$  is crucial to the ability of the experiments to be able to resolve degeneracies. We compute  $\sigma^{AB}$  in a manner similar to equation (7.3) by assuming that the statistical errors associated with the measurement are purely  $\sqrt{N}$

$$\sigma^{AB} = \sqrt{(1+f)(N_A + N_B)}, \quad (7.7)$$

and the overall multiplicative factor  $(1+f)$  allows us to be even more conservative by taking into account a nominal background rate or allow for uncertainties in the local halo density. The theoretical errors associated with the uncertainties in the nuclear matrix elements necessary to the calculation of  $\sigma_{\chi p}^{\text{SI}}$  are not included here but will be addressed later.

Using the distinguishability criteria none of the 378 models would have been distinguished already in CDMS II, XENON10 or ZEPLIN II. Nine models would have given at least ten events in 316.4 kg-days of exposure time in the Xenon10 experiment, and five would have given at least ten events in 397.8 kg-days of exposure time in the CDMS II experiment. These are models that could have been discovered at CDMS II (where no signal-like events were observed in the data *prior* to [70] where they may have seen something) or nearly discovered

at Xenon10 (where ten signal-like events were reported). However these models all have  $\Omega_\chi h^2 < 0.025$  and upon rescaling  $\rho_\chi$  by  $r_\chi$  none of the models give rates which should have been detected.

In Figures 7.3 and 7.4 we show the percentage of 276 degenerate pairs which can be distinguished as exposure time is accumulated in xenon and germanium targets. In both figures we use a separation criterion of  $5\sigma$  and assume no theoretical uncertainty. Heavy (red) lines are labeled for xenon, thinner (blue) lines are labeled for germanium. Solid lines have not been rescaled by the relic density ratio  $r_\chi$ , dashed lines have been rescaled. The upper four lines are obtained by requiring only  $N \geq 10$  recoil events for both models. The lower four lines are obtained by requiring  $N \geq 100$  recoil events for both models. The predicted exposure after one year for three projected liquid xenon experiments is indicated by the vertical lines as labeled, with the assumption of 200 days of data-taking per calendar year with 80% of the mass from Table 7.2 used as a fiducial target mass.

Working under the assumption of perfect theoretical inputs, when two models are visible above the background, they are easily distinguished. It is worthwhile to look at an example of the degenerate pairs listed in Table 7.3. The two models were deemed indistinguishable at

	Mass Parameters (GeV)						LSP Wave Function			
	$m_{N_1}$	$m_{N_2}$	$m_{C_1}$	$m_{\tilde{\tau}_1}$	$m_h$	$\mu$	$\tilde{B}\%$	$\tilde{W}\%$	$\tilde{H}\%$	$\Omega_\chi h^2$
Point A	237	240	239	261	117.4	991	78%	21%	1%	0.0054
Point B	260	749	260	450	117.4	949	0%	99%	1%	0.0026

Table 7.3: **Pair 212 of the 276 degenerate pairs.** Some key parameters for the two models making up degenerate pair #212. This particular case is an example of a “squeezer” degeneracy, as so dubbed by the authors of [175].

the LHC by the authors of [175] and such a model was dubbed a “squeezer” as the mass gaps in the electroweak gauginos in one model is small giving very soft, essentially undetectable leptons. The other model has similar lepton signatures due to the stau masses which happens by accident. Both models are physically acceptable although  $\Omega_\chi h^2$  is rather small due to the Wino content of the LSP. The SI cross sections for the two models are  $\sigma_{\chi p}^A = 3.61 \times 10^{-45}$

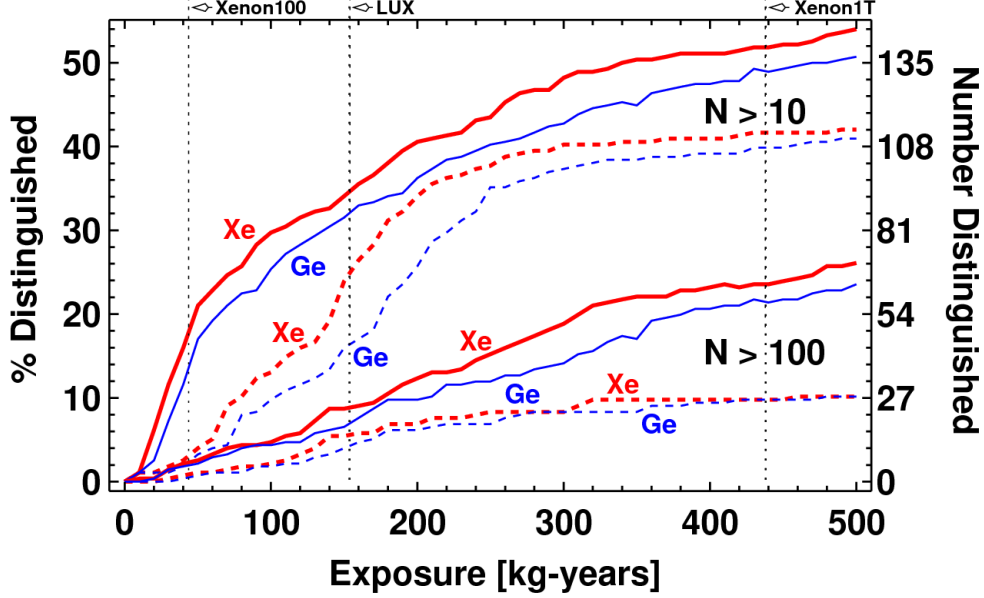


Figure 7.3: **Distinguishability analysis in 500 kg-years of exposure.** Plotted are the number of degenerate pairs and the percentage of the total that can be distinguished as a function of integrated exposure time. Both the exposure of germanium and xenon targets are shown with heavy (red) lines corresponding to xenon and thinner (blue) lines corresponding to germanium. The solid lines have not been rescaled by  $r_\chi$ , while the dashed lines have been rescaled. The upper four lines require only  $N \geq 10$  recoil events for both models and the lower four lines require  $N \geq 100$  recoil events for both models. The vertical lines are the predicted exposure after one year for three xenon experiments as indicated and for this we assume 200 days of data taking per year with 80% of the mass from Table 7.2 used as the fiducial target mass.

$\text{cm}^2$  and  $\sigma_{\chi p}^B = 4.56 \times 10^{-45} \text{ cm}^2$ . Without rescaling and using a xenon target we estimate that after 1 ton $\times$ year exposure (*not* the same as “Xenon1T”) the number of events would be  $N_A = 1310$  and  $N_B = 1517$ . If the rates are rescaled then the numbers become  $N_A = 282$  and  $N_B = 157$  which using  $f = 0$  (0.5) is a separation of  $6.4\sigma$  ( $5.3\sigma$ ).

The model pair just discussed is typical of the other degenerate pairs. The results are further shown using various values for the factor  $f$  in equation (7.7) at different exposures in Table 7.4. The models are still distinguishable to a good degree when  $f = 0.5$ , although this has all been done assuming perfect knowledge of the nuclear matrix elements. These tables indicate how well the experiments can potentially do to resolve the degeneracies but, as we will discuss next, without improving the uncertainties in the nuclear matrix elements

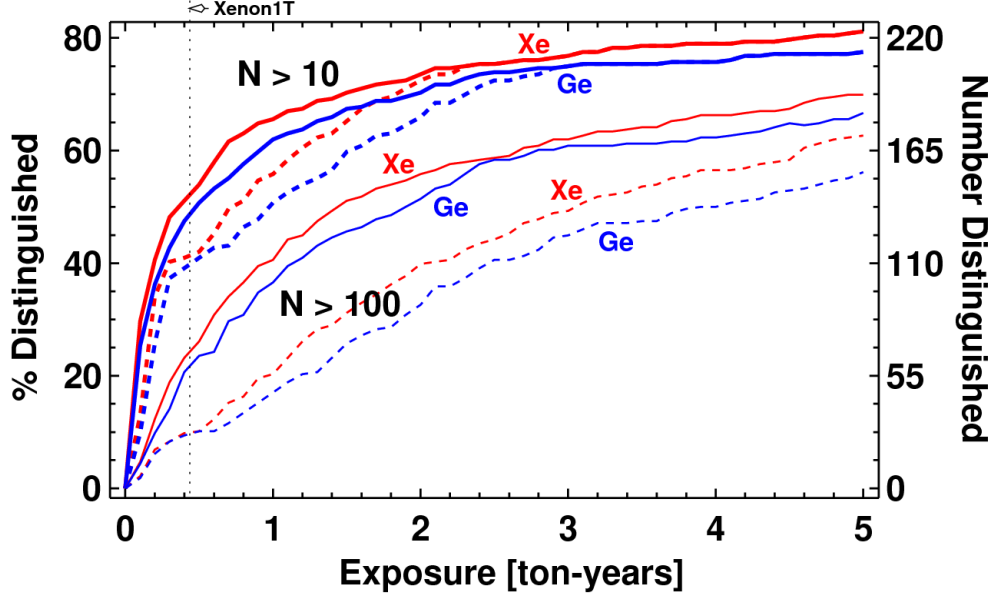


Figure 7.4: **Distinguishability analysis in 5 ton-years of exposure.** Same as Figure 7.3 but now for much larger exposures. The vertical line is our projection for one year of data taking at the XENON1T experiment where again we assume 200 days of data taking per year with 80% of the mass from Table 7.2 used as the fiducial target mass.

these results will be severely reduced.

Now we investigate the effects of the above analysis if we were to include uncertainties in the nuclear matrix elements. Initially this issue was brought up by Ellis et al. [67] by looking at the variation of  $\sigma_{\chi p}^{\text{SI}}$  which results from different inputs of the  $\pi N \Sigma$  term. We initially looked into this by using the range of inputs of the  $\pi N \Sigma$  term as in Ellis et al. and found an error in  $\sigma_{\chi p}^{\text{SI}}$  could occur as large as 50%, which was similar to the results of Ellis et al. as well as others [68]. To look at the effect of the errors on the ability of the direct detection experiments to distinguish models, uncertainties in the cross section are introduced via

$$(\delta\sigma_{\chi}^{\text{SI}})_{\text{theor}} = \epsilon \times \sigma_{\chi}^{\text{SI}}. \quad (7.8)$$

For the moment assuming this is the only source of error then  $\sigma^{AB}$  becomes

$$\sigma^{AB} = \epsilon \sqrt{N_A^2 + N_B^2}, \quad (7.9)$$

With Density Rescaling										
Require 100 Events						Require 10 Events				
Xenon			Germanium			Xenon			Germanium	
		$f = 0$	$f = 0.5$	$f = 0$	$f = 0.5$		$f = 0$	$f = 0.5$	$f = 0$	$f = 0.5$
0.1 ton-yr	$3\sigma$	8	8	8	7	$3\sigma$	24	22	24	21
	$5\sigma$	6	4	5	3	$5\sigma$	14	9	14	8
1 ton-yr	$3\sigma$	79	71	69	58	$3\sigma$	164	148	157	136
	$5\sigma$	52	43	48	37	$5\sigma$	112	81	105	73
5 ton-yr	$3\sigma$	199	182	187	178	$3\sigma$	217	199	212	201
	$5\sigma$	170	159	162	151	$5\sigma$	187	175	183	172

Without Density Rescaling										
Require 100 Events						Require 10 Events				
Xenon			Germanium			Xenon			Germanium	
		$f = 0$	$f = 0.5$	$f = 0$	$f = 0.5$		$f = 0$	$f = 0.5$	$f = 0$	$f = 0.5$
0.1 ton-yr	$3\sigma$	51	41	49	41	$3\sigma$	116	102	111	98
	$5\sigma$	36	29	32	25	$5\sigma$	81	69	77	63
1 ton-yr	$3\sigma$	177	168	168	161	$3\sigma$	210	200	208	198
	$5\sigma$	154	144	147	134	$5\sigma$	181	165	175	155
5 ton-yr	$3\sigma$	242	235	240	234	$3\sigma$	242	235	240	234
	$5\sigma$	224	216	217	211	$5\sigma$	224	216	217	211

Table 7.4: **Direct detection summary table.** Shown are the number of pairs distinguishable after a given accumulated exposure in xenon or germanium, based on the integration ranges specified in the text. Numbers in the upper table were computed with interaction rates scaled by the quantity  $r_\chi$ , while those in the lower table are not rescaled.

which can be a huge number compared to that in equation (7.7)! Adding the new source of error from equation (7.8) in quadrature with equation (7.7) now eliminates the potential for the direct detection experiments to resolve degenerate pairs. The results of including various values of  $\epsilon$  for the analysis done above is summarized in Table 7.5. The values in the table

Require 10 Events, Xenon					
		$\epsilon = 0$	$\epsilon = 0.1$	$\epsilon = 0.25$	$\epsilon = 0.5$
1 ton-yr	$3\sigma$	164	118	13	0
	$5\sigma$	112	46	0	0
5 ton-yr	$3\sigma$	217	149	25	0
	$5\sigma$	187	77	0	0

Table 7.5: **Effect of including theoretical uncertainties associated with nuclear matrix elements.** The number of pairs distinguishable after a given accumulated exposure in xenon when the theoretical uncertainty from equation (7.8) is included. The experimental error is taken to be purely statistical ( $f = 0$ ) and require 10 signal events. Numbers in this table were computed with interaction rates scaled by the quantity  $r_\chi$ .

can be compared to the upper right portion in Figure 7.4, which uses the same assumptions for  $\epsilon = 0$ . It is quiet clear that without improved values of the nuclear matrix elements

then the direct detection experiments will be unable to distinguish models. However if the errors can be reduced to the 10% level then there is hope for direct detection experiments to possibly lift model degeneracies which may arise at the LHC.

## 7.4 Gamma rays

Here the ability to distinguish models using continuous photon signals from neutralino annihilation in the galactic center is investigated. Monochromatic photons are also investigated in [178], but this will not be discussed here. The focus will be on the Fermi/GLAST experiment for the continuous photon signal. As in the case for the direct detection experiments we will calculate the continuous photon flux and then proceed to turn this into a number of photons in a given exposure (in units of area $\times$ time). The backgrounds will be outlined and then a method of distinguishability will be introduced. Reach curves similar to those in the previous section will be shown and finally the effect of considering a theoretical error in the calculation from not knowing exactly the precise dark matter halo profile.

The method of computing the rates has been explained in Chapter 3. A given halo model (from the choice of three in Table 3.1) will be assumed and then using equation (3.23) the differential photon flux is computed. An interpolating function of  $d\Phi/dE$  is then built in 1 GeV steps over the range from 1 GeV to 200 GeV as appropriate for Fermi/GLAST. Integrating the interpolation function over appropriate ranges will then give the photon flux,  $\Phi_\gamma$ . The photon flux has units of photons/(cm<sup>2</sup> $\times$ seconds) and choosing an effective area for Fermi/GLAST for a given time of data acquisition one can create a number of expected photons for a given model. These numbers of expected photons for the two degenerate model pairs can then be compared to deem if the models are distinguishable using the photon signal.

The backgrounds of continuous photons from other astrophysical sources are not as easy to deal with as the backgrounds in the direct detection experiments. The background photons can be rather substantial and furthermore one needs accurate and reliable modeling of the

background photon rate in order to be able to distinguish models. Gamma ray photons which contribute to the background can be produced in a variety of ways; for some examples see [183]. For photon energies in the range from 100 MeV to 1 TeV, which is relevant for the neutralino annihilation, the sum of the various backgrounds can be modeled in terms of the differential spectrum of the form [109]

$$\frac{d^2\Phi_\gamma^{\text{bkg}}}{d\Omega dE_\gamma} = \left( \frac{d\Phi_\gamma^{\text{bkg}}}{d\Omega dE_\gamma} \right)_0 \left( \frac{E_\gamma}{1 \text{ GeV}} \right)^{-2.7} \quad (7.10)$$

in units of photons/(cm<sup>2</sup>×sec×sr×GeV). A reasonable value for the prefactor is

$$\left( \frac{d^2\Phi_\gamma^{\text{bkg}}}{d\Omega dE_\gamma} \right)_0 \simeq 9 \times 10^{-5} \text{ photons/cm}^2/\text{s/sr/GeV} \quad (7.11)$$

in the direction of the galactic center. Using equation (7.11) and integrating equation (7.10) over an energy range of 1 GeV ≤ E<sub>γ</sub> ≤ 200 GeV with an angular resolution of ΔΩ = 10<sup>-5</sup> sr gives about 100 photon events per m<sup>2</sup>×year of exposure. Typically a given model is considered to be visible over the backgrounds if the flux is of order Φ<sub>γ</sub> ≃ 10<sup>-10</sup> photons/(cm<sup>2</sup>×sec×sr×GeV) [108, 110].

The backgrounds are not quite as straightforward as discussed above [183, 184, 185, 186]. The satellite-based experiment EGRET [187] found a higher than expected photon flux in the direction of the galactic center for photons with energy in the range 100 MeV to 10 GeV. Ground based ACT experiments have also observed large photon fluxes in the direction of the galactic center for photons with energies in the range 200 GeV to 10 TeV [188, 189, 190, 191]. A good possibility for these large backgrounds in both cases may be new point sources near the galactic center [192, 193] and it is expected that these point sources can be subtracted from the diffuse signal expected from the neutralino annihilation. In [194] the dark matter signals were separated from the background sources and we follow the method from [194] to account for the EGRET signal.

To proceed we consider two types of background sources. The first is the “low” back-

ground modeled by equation (7.10) using the prefactor as in equation (7.11). The second is the “high” background modeled as in the low background case along with adding an additional contribution

$$\frac{d\Phi_{\gamma}^{\text{EG}}}{dE_{\gamma}} = 2.2 \times 10^{-7} \times \exp\left(-\frac{E_{\gamma}}{30 \text{ GeV}}\right) \times \left(\frac{E_{\gamma}}{1 \text{ GeV}}\right)^{-2.2} \text{ photons/cm}^2/\text{s/GeV}. \quad (7.12)$$

to account for the EGRET measurement. The low and high backgrounds can now be used along with the signal calculations in order to distinguish models.

The Fermi/GLAST satellite will be the experimental proxy from which we base the study. The relevant parameters for the experiment are given in Table 7.6. The photon flux signal,

	$E_{\text{min}}$	$E_{\text{max}}$	$\sigma_{E/E}$	$A_{\text{eff}}$	$\Delta\Omega$
GLAST	50 MeV	300 GeV	10%	$1 \times 10^4 \text{ cm}^2$	$1 \times 10^{-5} \text{ sr}$

Table 7.6: **Gamma ray Fermi/GLAST experiment.** For the analysis presented in this section we consider the gamma ray observatory of the Fermi/GLAST satellite-based experiment.

$\Phi_{\gamma}$ , is found for six energy bins: 1-10 GeV, 10-30 GeV, 30-60 GeV, 60-100 GeV, 100-150 GeV and 150-200 GeV. The total gamma ray flux is also found for each model over the range 1 to 200 GeV. The following conditions are required in order for two degenerate models to be deemed distinguishable using the continuous photon flux:

1. The total number of gamma ray photons  $N_{\gamma}$  collected by the experiment over the full energy range  $1 \text{ GeV} \leq E_{\gamma} \leq 200 \text{ GeV}$  must satisfy  $N_{\gamma} > 100$ . We require this to be true of *both* models in the model pair.
2. We require in addition that a significant excess of gamma ray photons above background is observed in *multiple, adjacent* energy bins. The premise behind this requirement is the desire to have some spectral information on the component of the flux arising from dark matter annihilation to better separate this source from other astrophysical sources. Specifically, if  $i = 1, \dots, 6$  labels our six energy bins, then we

demand  $N_i > m\sqrt{N_i^{\text{bkg}}}$  for at least three adjacent bins. Here  $N_i$  is the number of photons observed in that energy bin,  $N_i^{\text{bkg}}$  is the expected background count (computed either with the “low” or the “high” background model), and  $m$  is the significance level in units of  $\text{signal}/\sqrt{\text{bkgrnd}}$ . In what follows we will demand  $m = 2$ .

3. If the above two conditions are satisfied by models  $A$  and  $B$  then we will say that the two potential signals are detectable. We will further say that they are distinguishable if the condition  $|N_i^A - N_i^B| > n\sqrt{N_i^A + N_i^B + 2N_i^{\text{bkg}}}$  holds for at least three adjacent bins, simultaneously. Results will be given for significance levels  $n = 3$  and  $n = 5$ .

To get a sense of the signals which arise from the degenerate pairs we consider the total integrated flux from 1 to 200 GeV. First we use the NFW profile and do not rescale the local halo density by  $r_\chi$  with the total gamma ray flux shown in Figure 7.5. Also shown in the figure are the various backgrounds integrated over the range 1 to 200 GeV. In the case of the NFW profile if one includes the rescaling then the typical signals are on the order of  $10^{-11}$  photons/( $\text{cm}^2 \times \text{second}$ ) and are not easily visible above the backgrounds. In Figure 7.6 we show the total flux of the degenerate pairs using the NFW+AC halo profile and now the models are rescaled by  $r_\chi$  if necessary. Using the more favorable profile results in more models which can potentially be seen above background.

Using the distinguishability conditions we can now determine how well the models can be separated as Fermi/GLAST accumulates data, with the exposure in units of  $\text{m}^2 \times \text{years}$ . In Figure 7.7 we show how well the models can be separated with the NFW+AC profile using the low and high backgrounds as well as rescaling and not rescaling the data. Keep in mind that an exposure of  $1 \text{ m}^2 \times \text{year}$  does not translate into 1 year of data acquisition at Fermi/GLAST since, for example, the telescope does not point in the direction of the galactic center at all times. The solid lines use the low background estimation, while the dashed lines use the high background estimation. The upper curves have not been rescaled by  $r_\chi$  while the lower curves have been rescaled. The more conservative assumptions of rescaling with the

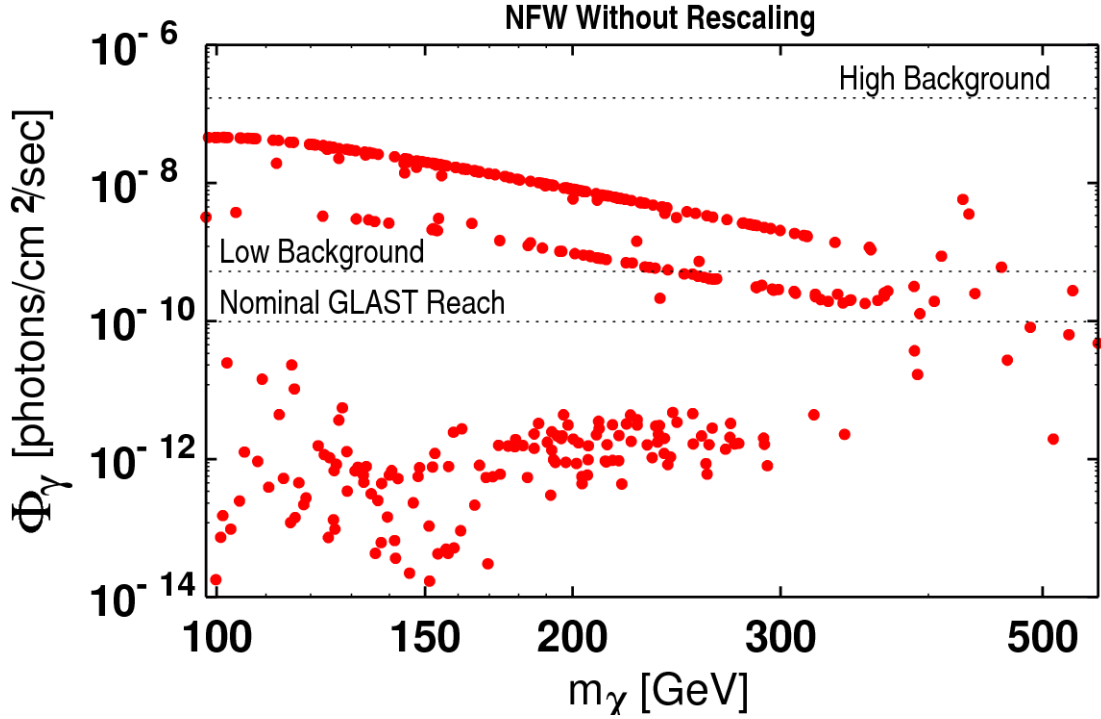


Figure 7.5: **Integrated photon flux for NFW profile.** The differential photon flux is integrated over the energy range  $1 \text{ GeV} \leq E_\gamma \leq 200 \text{ GeV}$  for the NFW profile. In this plot none of the rates have been rescaled by  $r_\chi$ . The flux from background sources are indicated by the horizontal dotted lines for our “low” and “high” background models. Also shown is the nominal sensitivity threshold claimed by the Fermi/GLAST collaboration.

high background result in only about 20% of the models being distinguished in  $5 \text{ m}^2 \times \text{years}$  of exposure. If we consider the rescaling and only the low backgrounds then about 40% of the models can be distinguished in  $5 \text{ m}^2 \times \text{years}$ . Relaxing the rescaling requirement results in even more models which can be distinguished. Some further results are given in Table 7.7 for various halo profiles both for rescaled and not-rescaled models. Depending on the halo profile used the results can vary quite a bit, and this brings us to the issue of just how to interpret and use a halo profile.

The results which have been considered to this point have worked under the assumption that one and only one halo profile describes the dark matter distribution in the galactic center. Depending on the profile used the value for  $\bar{J}$  can vary quite a bit (see Table 3.1) and the results clearly change with the choice of profile. Whether the halo model is made of

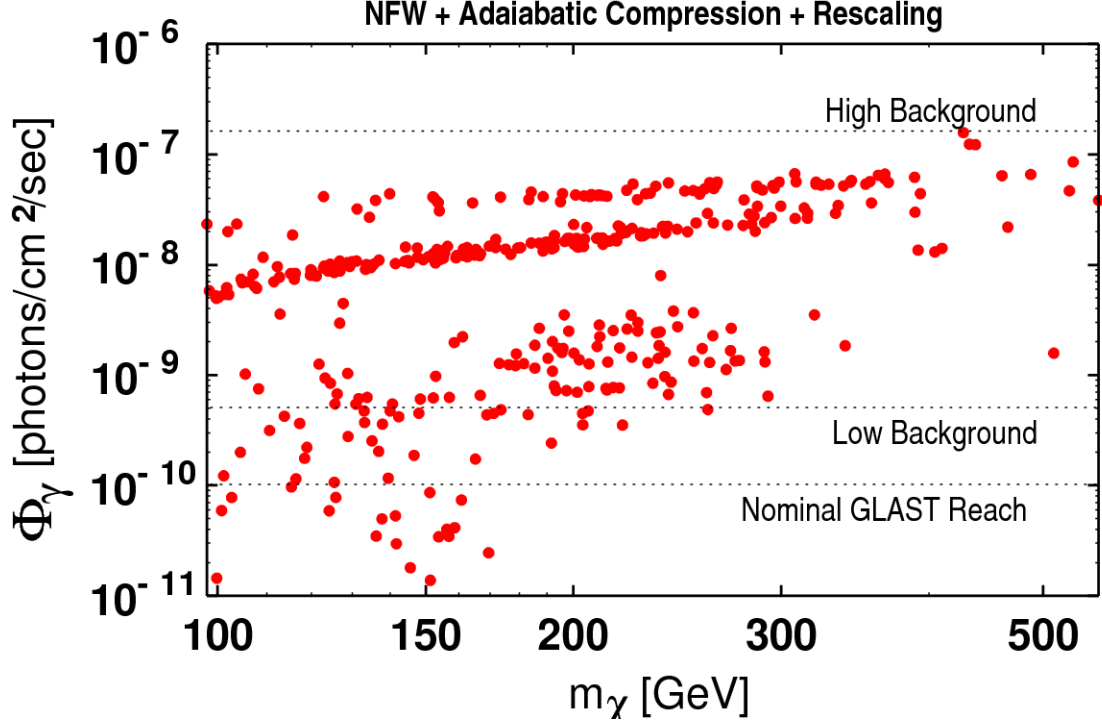


Figure 7.6: **Integrated photon flux for NFW profile + adiabatic compression.** Same as Figure 7.5 but with the addition of adiabatic compression. Here we have rescaled the annihilation rate by the factor  $r_\chi$ .

one of a set of discrete options is not entirely clear either. If one treats the value of  $\bar{J}$  as an undetermined free parameter we can then ask how well it needs to be determined in order to distinguish models. In other words we consider an error on the halo profile by using

$$(\delta\bar{J})_{\text{theory}} = \epsilon \times \bar{J}(\Delta\Omega), \quad (7.13)$$

in a similar manner to the uncertainties in  $\sigma_{\chi p}^{\text{SI}}$  as discussed in the previous section. Using the NFW+AC profile we computed the total gamma ray flux from 1 to 200 GeV with no rescaling and considered the total number of photons collected after  $3 \text{ m}^2 \times \text{years}$ . Then using a  $3\sigma$  separation we looked at how many models could be distinguished using various values of  $\epsilon$ . Using  $\epsilon = 5\%$ , 152, 102 and 22 model pairs of 276 total can be distinguished for the cases of no, low and high backgrounds, respectively (for comparison look at the corresponding

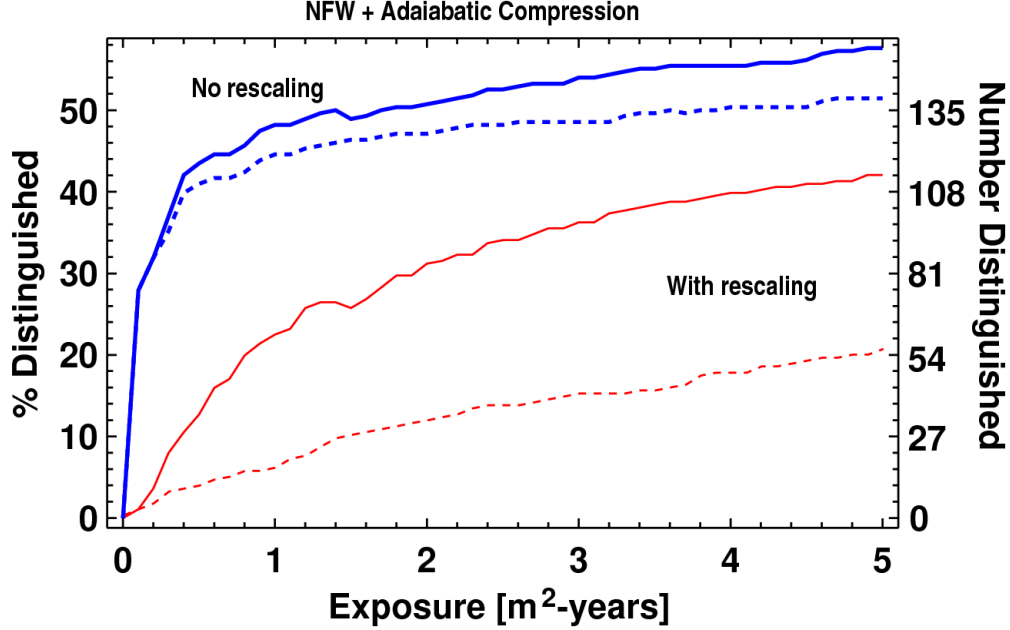


Figure 7.7: **Distinguishability analysis at Fermi/GLAST.** The lower two curves rescale the local halo density by the factor  $r_\chi$  while the upper two curves have no rescaling. The solid lines give the number of distinguished pairs using the “low” background estimate, while dashed lines are for the “high” background estimate.

column in Table 7.7). Distinguishing models becomes steadily more difficult as  $\epsilon$  increases, for example  $\epsilon \simeq 32\%$  (low background) and  $\epsilon \simeq 26\%$  (high background) results in no models being distinguishable under the assumptions here. Understanding the halo profile to the 5 – 10% level will be necessary in order to utilize Fermi/GLAST to resolve any degenerate models.

## 7.5 Summary

Supersymmetry is a leading candidate for physics beyond the Standard Model and is likely to be discovered at the LHC. Based on the results of [175] it is quite probable that more than one candidate SUSY model will give a good fit to the ensemble of measurements which will be made. If more than one model is a good fit to the data then orthogonal information from other experimental arenas will be needed to break the degeneracies. Assuming that

	NFW not rescaled		NFW adiab. comp. rescaled		NFW adiab. comp. not rescaled		Moore adiab. comp. rescaled		
	low	high	low	high	low	high	low	high	
Background:	$3\sigma$	4	0	98	29	148	133	220	165
1 m <sup>2</sup> yr	$3\sigma$	22	0	135	49	160	145	232	186
	$5\sigma$	0	0	60	14	131	122	196	151
3 m <sup>2</sup> yr	$3\sigma$	35	0	147	62	167	147	207	194
	$5\sigma$	9	0	95	33	144	134	185	173
5 m <sup>2</sup> yr	$3\sigma$	13	0	111	42	154	139	194	183
	$5\sigma$								

Table 7.7: **Summary of integrated gamma ray fluxes.** Listed are the number of pairs distinguishable at the  $n = 3\sigma$  and  $5\sigma$  level for three different integrated exposures at Fermi/GLAST. The four halo models assumptions are NFW without halo rescaling, NFW plus adiabatic compression (with and without halo rescaling) and Moore et al. with halo rescaling. Both the low (or standard) background estimate along with the EGRET-normalized higher background are considered. Here the theoretical uncertainties for the halo models are neglected.

the LSP is stable and the lightest neutralino then dark matter experiments offer just such orthogonal information.

We have investigated a subset of the information from dark matter experiments which may be available in the near future. When considering the direct detection and indirect detection gamma ray experiments together one can generally do well at untangling the degenerate models. Of course this statement assumes that near perfect understanding exists of the theoretical inputs such as the nuclear matrix elements or the dark matter halo profile at the galactic center. It is our hope that these uncertainties can be overcome by the time that accurate measurements would be needed to break any potential degeneracies in the LHC data.

Assuming that the theoretical uncertainties have been overcome we now summarize the basic results. To discuss the results as a whole we also include the monochromatic gamma ray experiment results from [178] which were not discussed here. The monochromatic signals rely on atmospheric Cherenkov telescopes (ACTs) which have a much larger area and energy

range than Fermi/GLAST, but they are ground based and only take data on clear nights. For further information regarding the method of distinguishability and other details for the monochromatic signals, see [178]. Three viewpoints are used to classify the results:

**Conservative** All the rates are rescaled by  $r_\chi = \text{Min}(1, \Omega_\chi h^2/0.025)$ . For the direct detection experiments at least 100 scattering events are required with  $5\sigma$  separation between the models including a factor of  $f = 0.2$  and we assume 100 kg-years of exposure in germanium and 1 ton-year of exposure in xenon. For the photon signals we assume a NFW halo profile with adiabatic compression and signals are required to be separable by  $5\sigma$  ( $2\sigma$ ) and be above background by  $2\sigma$  ( $5\sigma$ ) for the continuous gamma ray observations (monochromatic lines). The continuous photon signals are required to have at least 100 photons with energy between 1 and 200 GeV and the “high” background is used for  $5 \text{ m}^2 \times \text{years}$  of exposure. The monochromatic photon signals are required to have at least 10 photons and the “high” background is used for the generic ACT with  $1000 \text{ m}^2 \times \text{years}$  of exposure.

**Moderate** The same as the conservative criteria, but now the background requirements are relaxed. For direct detection experiments we require 10 events and set  $f = 0$ . For the photon signals the “low” backgrounds are used and the ACT exposure is taken to be  $2500 \text{ m}^2 \times \text{years}$ .

**Optimistic** The same as the moderate criteria but now no rescaling by  $r_\chi$  is done. The germanium experiments are assumed to reach 1 ton $\times$ year of exposure, liquid xenon experiments will have 5 ton $\times$ years of exposure and the ACT experiment will have  $10000 \text{ m}^2 \times \text{years}$  of exposure.

Using these criteria the number of distinguishable pairs out of the 276 considered are tabulated in Table 7.8. Again we stress that we assume the theoretical uncertainties as in equations (7.8) and (7.13) have been brought under control.

	Conservative	Moderate	Optimistic
All Pairs			
Direct detection, xenon	48	112	224
Direct detection, germanium	4	14	147
Gamma rays, continuum	56	115	158
Gamma rays, monochromatic	23	34	36
All Pairs, All Signals	101	186	245
Physical Pairs Only	34	55	77
ILC Inseparable Only	32	62	81

Table 7.8: **Final distinguishability results.** The final number of pairs from the original set of 276 pairs which can be distinguished using all of the experimental data considered here. In the upper section of the table the total number is broken down by the experiments, note that many pairs can be distinguished by more than one set of observations. The set of 77 physical pairs were defined in Section 7.2. The set denoted “ILC Inseparable” are the 103 pairs for which neither model had a charged superpartner below 240 GeV in mass. The set of assumptions which define the Conservative, Moderate and Optimistic scenarios are described in the text.

# Chapter 8

## Conclusions

This thesis has focused on various aspects of dark matter and LHC phenomenology of non-universal gaugino masses. Non-universalities in the gaugino sector are theoretically well motivated as specific patterns can relate back to the mechanism responsible for mediating supersymmetry breaking. Obtaining ratios of the soft SUSY breaking gaugino masses at the low scale will offer important information as to the possible high scale models which may be favored.

The string-motivated scenario of deflected mirage mediation was investigated with emphasis on the neutralino sector and the resulting dark matter signals. This model is intriguing in its own right as gravity, anomaly and gauge mediated SUSY breaking contribute to the soft terms. The gaugino sector of the theory is quite rich resulting in areas which give Bino, Wino and mixed LSPs for a variety of LSP masses. This leads to a quite complex array of predictions in the dark matter arena for the model. Regions of the parameter space where the three mediation mechanisms are all operative are found in which the relic neutralino is found with a thermal abundance in agreement with recent WMAP measurements. The direct detection prospects are best for regions with mixed LSPs and may soon be probed at the XENON100 experiment. There are regions of the space too which can possibly explain the recent CDMS II data. Gamma ray signals have the best opportunities to be seen in the near future in regions where the LSP is mostly Wino. Prospects for the signals at IceCube are best for a mixed Higgsino/Wino LSP.

The recent CDMS II direct detection experiment reported the observation of two events which are consistent with neutralino scattering from nucleons. We highlighted the ability of

non-universalities in the gaugino masses to account for this signal as these types of models have the largest spin independent cross sections. These models are in agreement with earlier data from XENON10 and predict rates which ought to be clear signals at XENON100. The gamma ray signals ought to be detectable over the astrophysical backgrounds at the Fermi/GLAST experiment if one assumes a favorable dark matter halo such as the NFW + adiabatic compression. The models also have good prospects for detection at IceCube. Some basic collider implications are that the models will likely not have as good of discovery prospects using leptonic signatures at the LHC due to the compressed gaugino sector masses, while the multijet signatures give strong signal significance. If models of these types are favored as data is collected then they may offer a strong hint at the presence of non-thermal production of relic neutralinos.

A simple parametrization of gaugino mass non-universalities was investigated for two string-inspired benchmarks at the LHC. A single parameter  $\alpha$  is used to make small perturbations on the gaugino mass non-universalities in order to study the resulting LHC signatures. Specific signature lists were analyzed which were constructed to track small variations in  $\alpha$ . These targeted observables can determine non-universalities in the gaugino sector using a minimum amount of integrated luminosity. When taking the universal case as the point of reference the signature lists can reveal the presence of non-universalities of  $\alpha \gtrsim 0.2$  using 10-20  $fb^{-1}$  of LHC data for the benchmark models. If the predicted values of  $\alpha$  are used for the benchmarks then a similar statement holds when one moves more than 0.2 in  $\alpha$  away from the predicted value.

If supersymmetry is discovered at the LHC then it is likely that more than one candidate model may be able to describe the data. This scenario is called the LHC inverse problem and we investigated the utility of dark matter observables to break these possible model degeneracies. Using models pairs which were deemed degenerate we showed that a large number of model pairs can indeed be distinguished using dark matter signatures from direct detection and indirect gamma ray experiments. This relies on good knowledge of the back-

grounds as well as assuming that theoretical uncertainties associated with nuclear matrix elements and the dark matter halo can be brought under control. Often a model pair that is not distinguishable involves neutralinos which are not of the same makeup and hence the dark matter observables do quite well at revealing this fact, whereas the LHC does not.

# Chapter 9

## Appendix

### SM backgrounds

The SM backgrounds which are considered here are based off of the approach taken in the LHC Olympics and the PYTHIA input cards for the SM processes can be found here [174]. The backgrounds consist of the following production modes:  $b\bar{b}$ ,  $t\bar{t}$ , dijets, Drell-Yan, single  $W$ , single  $Z$ ,  $WW$  leptonic,  $ZZ$  leptonic and  $WZ$  leptonic. As an aid to help understand the nature of the backgrounds used in the various analysis we show the  $\cancel{E}_T$  distributions for the various SM processes. The cuts applied to the LHC data sets typically rely quite heavily on the  $\cancel{E}_T$  cut as it greatly increases the signal significance.

The backgrounds were generated at the LHC for  $\sqrt{s} = 14$  TeV using L1 triggers in PGS for  $5fb^{-1}$  of integrated luminosity. The  $WW$ ,  $ZZ$  and  $WZ$  leptonic data sets are combined into the  $XX$  leptonic backgrounds. In Figures 9.1 and 9.2 we show the normalized  $\cancel{E}_T$  distributions for the backgrounds, where an additional cut of  $\cancel{E}_T \geq 100$  GeV has been applied.

	$b\bar{b}$	$t\bar{t}$	dijets	Drell-Yan	$W$	$Z$	$WW$	$ZZ$	$WZ$
$\sigma$ [pb]	4200	540	4270	4980	3110	2590	20	0.2	2

Table 9.1: SM background cross sections.

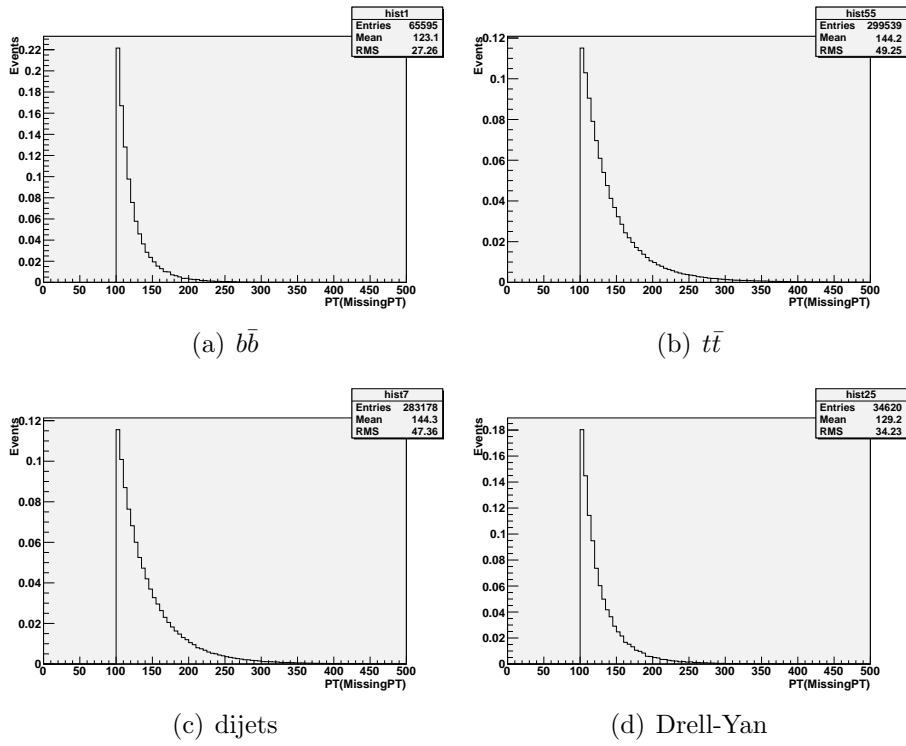
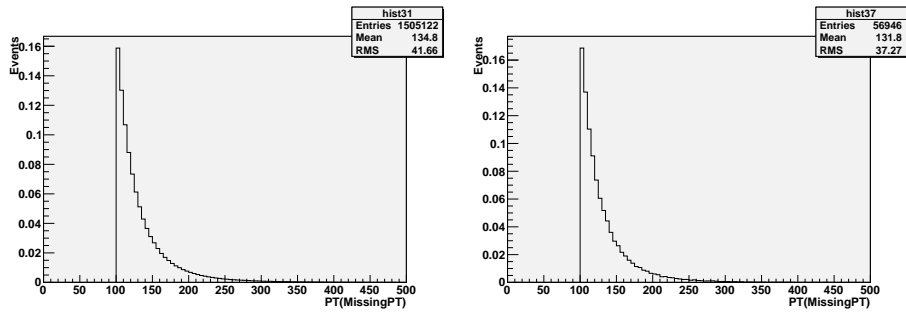
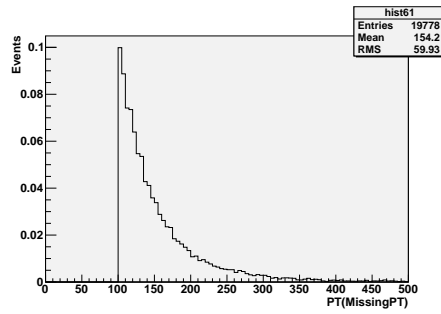


Figure 9.1: SM background  $E_T$  distributions.



(a) single  $W$

(b) single  $Z$



(c)  $XX$  leptonic

Figure 9.2: SM background  $E_T$  distributions.

# Bibliography

- [1] P. Nath et al. The Hunt for New Physics at the Large Hadron Collider. 2010.
- [2] S. L. Glashow. Partial Symmetries of Weak Interactions. *Nucl. Phys.*, 22:579–588, 1961.
- [3] Steven Weinberg. A Model of Leptons. *Phys. Rev. Lett.*, 19:1264–1266, 1967.
- [4] Abdus Salam. Weak and Electromagnetic Interactions. Originally printed in \*Svartholm: Elementary Particle Theory, Proceedings Of The Nobel Symposium Held 1968 At Lerum, Sweden\*, Stockholm 1968, 367-377.
- [5] Gerard 't Hooft. Renormalization of Massless Yang-Mills Fields. *Nucl. Phys.*, B33:173–199, 1971.
- [6] Gerard 't Hooft. Renormalizable Lagrangians for Massive Yang-Mills Fields. *Nucl. Phys.*, B35:167–188, 1971.
- [7] Gerard 't Hooft and M. J. G. Veltman. Regularization and Renormalization of Gauge Fields. *Nucl. Phys.*, B44:189–213, 1972.
- [8] D. J. Gross and Frank Wilczek. Ultraviolet Behavior of Non-Abelian Gauge Theories. *Phys. Rev. Lett.*, 30:1343–1346, 1973.
- [9] H. David Politzer. Reliable Perturbative Results for Strong Interactions? *Phys. Rev. Lett.*, 30:1346–1349, 1973.
- [10] D. J. Gross and Frank Wilczek. Asymptotically Free Gauge Theories. 1. *Phys. Rev.*, D8:3633–3652, 1973.
- [11] D. J. Gross and Frank Wilczek. Asymptotically Free Gauge Theories. 2. *Phys. Rev.*, D9:980–993, 1974.
- [12] H. David Politzer. Asymptotic Freedom: An Approach to Strong Interactions. *Phys. Rept.*, 14:129–180, 1974.
- [13] J. Wess and B. Zumino. A Lagrangian Model Invariant Under Supergauge Transformations. *Phys. Lett.*, B49:52, 1974.
- [14] Stephen P. Martin. A Supersymmetry Primer. 1997.
- [15] D. J. H. Chung et al. The soft supersymmetry-breaking Lagrangian: Theory and applications. *Phys. Rept.*, 407:1–203, 2005.
- [16] J. Wess and J. Bagger. *Supersymmetry and Supergravity*. Princeton University Press, 1992.

- [17] D. Balin and A. Love. *Supersymmetric Gauge Field Theory and String Theory*. Taylor & Francis, 1994.
- [18] M. Drees, R. Godbole, and P. Roy. *Theory and Phenomenology of Sparticles*. World Scientific, 2004.
- [19] H. Baer and X. Tata. *Weak Scale Supersymmetry*. Cambridge University Press, 2006.
- [20] J. Terning. *Modern Supersymmetry*. Oxford University Press, 2006.
- [21] P. Binétruy. *Supersymmetry: Theory, Experiment, and Cosmology*. Oxford University Press, 2006.
- [22] L. Girardello and Marcus T. Grisaru. Soft Breaking of Supersymmetry. *Nucl. Phys.*, B194:65, 1982.
- [23] Claude Amsler et al. Review of particle physics. *Phys. Lett.*, B667:1, 2008.
- [24] Pran Nath and Pavel Fileviez Perez. Proton stability in grand unified theories, in strings, and in branes. *Phys. Rept.*, 441:191–317, 2007.
- [25] Ali H. Chamseddine, Richard L. Arnowitt, and Pran Nath. Locally Supersymmetric Grand Unification. *Phys. Rev. Lett.*, 49:970, 1982.
- [26] Hans Peter Nilles. Supersymmetry, Supergravity and Particle Physics. *Phys. Rept.*, 110:1–162, 1984.
- [27] Vadim S. Kaplunovsky and Jan Louis. Model independent analysis of soft terms in effective supergravity and in string theory. *Phys. Lett.*, B306:269–275, 1993.
- [28] Lisa Randall and Raman Sundrum. Out of this world supersymmetry breaking. *Nucl. Phys.*, B557:79–118, 1999.
- [29] Gian F. Giudice, Markus A. Luty, Hitoshi Murayama, and Riccardo Rattazzi. Gaugino Mass without Singlets. *JHEP*, 12:027, 1998.
- [30] G. F. Giudice and R. Rattazzi. Theories with gauge-mediated supersymmetry breaking. *Phys. Rept.*, 322:419–499, 1999.
- [31] Stephen P. Martin and Michael T. Vaughn. Two loop renormalization group equations for soft supersymmetry breaking couplings. *Phys. Rev.*, D50:2282, 1994.
- [32] Damien M. Pierce, Jonathan A. Bagger, Konstantin T. Matchev, and Ren-jie Zhang. Precision corrections in the minimal supersymmetric standard model. *Nucl. Phys.*, B491:3–67, 1997.
- [33] Jihn E. Kim and Hans Peter Nilles. The mu Problem and the Strong CP Problem. *Phys. Lett.*, B138:150, 1984.
- [34] G. F. Giudice and A. Masiero. A Natural Solution to the mu Problem in Supergravity Theories. *Phys. Lett.*, B206:480–484, 1988.

- [35] E. J. Chun, Jihun E. Kim, and Hans Peter Nilles. A Natural solution of the mu problem with a composite axion in the hidden sector. *Nucl. Phys.*, B370:105–122, 1992.
- [36] J. A. Casas and C. Munoz. A Natural Solution to the MU Problem. *Phys. Lett.*, B306:288–294, 1993.
- [37] G. R. Dvali, G. F. Giudice, and A. Pomarol. The  $\mu$ -Problem in Theories with Gauge-Mediated Supersymmetry Breaking. *Nucl. Phys.*, B478:31–45, 1996.
- [38] Lars Bergstrom and Paolo Gondolo. Limits on direct detection of neutralino dark matter from  $b \rightarrow \bar{c} s \gamma$  decays. *Astropart. Phys.*, 5:263–278, 1996.
- [39] Stephen P. Martin and Michael T. Vaughn. Regularization dependence of running couplings in softly broken supersymmetry. *Phys. Lett.*, B318:331–337, 1993.
- [40] Manuel Drees, Mihoko M. Nojiri, D. P. Roy, and Youichi Yamada. Light Higgsino dark matter. *Phys. Rev.*, D56:276–290, 1997.
- [41] M. M. El Kheishen, A. A. Aboshousha, and A. A. Shafik. Analytic formulas for the neutralino masses and the neutralino mixing matrix. *Phys. Rev.*, D45:4345–4348, 1992.
- [42] Vernon D. Barger, M. S. Berger, and P. Ohmann. The Supersymmetric particle spectrum. *Phys. Rev.*, D49:4908–4930, 1994.
- [43] Gianfranco Bertone, Dan Hooper, and Joseph Silk. Particle dark matter: Evidence, candidates and constraints. *Phys. Rept.*, 405:279–390, 2005.
- [44] Pran Nath, Ali H. Chamseddine, and Richard L. Arnowitt. Nucleon Decay in Supergravity Unified Theories. *Phys. Rev.*, D32:2348–2358, 1985.
- [45] H. Goldberg. Constraint on the photino mass from cosmology. *Phys. Rev. Lett.*, 50:1419, 1983.
- [46] I. Hinchliffe, F. E. Paige, M. D. Shapiro, J. Soderqvist, and W. Yao. Precision SUSY measurements at CERN LHC. *Phys. Rev.*, D55:5520–5540, 1997.
- [47] David E. Morrissey, Tilman Plehn, and Tim M. P. Tait. New Physics at the LHC. 2009.
- [48] Gerard Jungman, Marc Kamionkowski, and Kim Griest. Supersymmetric dark matter. *Phys. Rept.*, 267:195–373, 1996.
- [49] Lars Bergstrom. Non-baryonic dark matter: Observational evidence and detection methods. *Rept. Prog. Phys.*, 63:793, 2000.
- [50] A. B. Lahanas. LSP as a candidate for dark matter. *Lect. Notes Phys.*, 720:35–68, 2007.
- [51] Marco Taoso, Gianfranco Bertone, and Antonio Masiero. Dark Matter Candidates: A Ten-Point Test. *JCAP*, 0803:022, 2008.

- [52] Jonathan L. Feng, Arvind Rajaraman, and Fumihiro Takayama. Superweakly-interacting massive particles. *Phys. Rev. Lett.*, 91:011302, 2003.
- [53] Toby Falk, Keith A. Olive, and Mark Srednicki. Heavy Sneutrinos as Dark Matter. *Phys. Lett.*, B339:248–251, 1994.
- [54] John R. Ellis, J. S. Hagelin, Dimitri V. Nanopoulos, Keith A. Olive, and M. Srednicki. Supersymmetric relics from the big bang. *Nucl. Phys.*, B238:453–476, 1984.
- [55] Benjamin W. Lee and Steven Weinberg. Cosmological lower bound on heavy-neutrino masses. *Phys. Rev. Lett.*, 39:165–168, 1977.
- [56] Kim Griest and David Seckel. Three exceptions in the calculation of relic abundances. *Phys. Rev.*, D43:3191–3203, 1991.
- [57] Pran Nath and Richard L. Arnowitt. Predictions in SU(5) supergravity grand unification with proton stability and relic density constraints. *Phys. Rev. Lett.*, 70:3696–3699, 1993.
- [58] P. Gondolo et al. DarkSUSY: Computing supersymmetric dark matter properties numerically. *JCAP*, 0407:008, 2004.
- [59] G. Belanger, F. Boudjema, A. Pukhov, and A. Semenov. Dark matter direct detection rate in a generic model with micrOMEGAs2.1. *Comput. Phys. Commun.*, 180:747–767, 2009.
- [60] T. Moroi, Masahiro Yamaguchi, and T. Yanagida. On the solution to the Polonyi problem with 0 (10-TeV) gravitino mass in supergravity. *Phys. Lett.*, B342:105–110, 1995.
- [61] M. Kawasaki, T. Moroi, and T. Yanagida. Constraint on the Reheating Temperature from the Decay of the Polonyi Field. *Phys. Lett.*, B370:52–58, 1996.
- [62] Takeo Moroi and Lisa Randall. Wino cold dark matter from anomaly-mediated SUSY breaking. *Nucl. Phys.*, B570:455–472, 2000.
- [63] Pierre Salati. Quintessence and the Relic Density of Neutralinos. *Phys. Lett.*, B571:121–131, 2003.
- [64] Scott Watson. Reevaluating the Cosmological Origin of Dark Matter. 2009.
- [65] R. J. Gaitskell. Direct detection of dark matter. *Ann. Rev. Nucl. Part. Sci.*, 54:315–359, 2004.
- [66] Paolo Gondolo. Phenomenological introduction to direct dark matter detection. 1996.
- [67] John R. Ellis, Keith A. Olive, and Christopher Savage. Hadronic Uncertainties in the Elastic Scattering of Supersymmetric Dark Matter. *Phys. Rev.*, D77:065026, 2008.

- [68] Vernon Barger et al. Recoil detection of the lightest neutralino in MSSM singlet extensions. *Phys. Rev.*, D75:115002, 2007.
- [69] J. Angle et al. First Results from the XENON10 Dark Matter Experiment at the Gran Sasso National Laboratory. *Phys. Rev. Lett.*, 100:021303, 2008.
- [70] Z. Ahmed et al. Results from the Final Exposure of the CDMS II Experiment. 2009.
- [71] Julio F. Navarro, Carlos S. Frenk, and Simon D. M. White. The Structure of Cold Dark Matter Halos. *Astrophys. J.*, 462:563–575, 1996.
- [72] Julio F. Navarro, Carlos S. Frenk, and Simon D. M. White. A Universal Density Profile from Hierarchical Clustering. *Astrophys. J.*, 490:493–508, 1997.
- [73] George R. Blumenthal, S. M. Faber, Ricardo Flores, and Joel R. Primack. Contraction of Dark Matter Galactic Halos Due to Baryonic Infall. *Astrophys. J.*, 301:27, 1986.
- [74] Y. Mambrini, C. Munoz, E. Nezri, and F. Prada. Adiabatic compression and indirect detection of supersymmetric dark matter. *JCAP*, 0601:010, 2006.
- [75] B. Moore et al. Dark matter substructure within galactic halos. *Astrophys. J.*, 524:L19–L22, 1999.
- [76] Torbjorn Sjostrand. PYTHIA 5.7 and JETSET 7.4: Physics and manual. 1995.
- [77] Phill Grajek, Gordon Kane, Daniel J. Phalen, Aaron Pierce, and Scott Watson. Neutralino Dark Matter from Indirect Detection Revisited. 2008.
- [78] Oscar Adriani et al. An anomalous positron abundance in cosmic rays with energies 1.5–100 GeV. *Nature*, 458:607–609, 2009.
- [79] Daniel Feldman, Zuowei Liu, Pran Nath, and Brent D. Nelson. Explaining PAMELA and WMAP data through Coannihilations in Extended SUGRA with Collider Implications. *Phys. Rev.*, D80:075001, 2009.
- [80] Francis Halzen. Astroparticle physics with high energy neutrinos: From AMANDA to IceCube. *Eur. Phys. J.*, C46:669–687, 2006.
- [81] Lisa L. Everett, Ian-Woo Kim, Peter Ouyang, and Kathryn M. Zurek. Deflected Mirage Mediation: A Framework for Generalized Supersymmetry Breaking. *Phys. Rev. Lett.*, 101:101803, 2008.
- [82] Lisa L. Everett, Ian-Woo Kim, Peter Ouyang, and Kathryn M. Zurek. Moduli Stabilization and Supersymmetry Breaking in Deflected Mirage Mediation. *JHEP*, 08:102, 2008.
- [83] Kiwoon Choi. Moduli stabilization and the pattern of sparticle spectra. *AIP Conf. Proc.*, 1078:138–143, 2009.

- [84] Kiwoon Choi, Kwang Sik Jeong, Shuntaro Nakamura, Ken-Ichi Okumura, and Masahiro Yamaguchi. Sparticle masses in deflected mirage mediation. *JHEP*, 04:107, 2009.
- [85] Michael Holmes and Brent D. Nelson. Dark Matter Prospects in Deflected Mirage Mediation. *JCAP*, 0907:019, 2009.
- [86] Kiwoon Choi, Adam Falkowski, Hans Peter Nilles, and Marek Olechowski. Soft supersymmetry breaking in KKLT flux compactification. *Nucl. Phys.*, B718:113–133, 2005.
- [87] Kiwoon Choi, Kwang Sik Jeong, and Ken-ichi Okumura. Phenomenology of mixed modulus-anomaly mediation in fluxed string compactifications and brane models. *JHEP*, 09:039, 2005.
- [88] Kiwoon Choi and Hans Peter Nilles. The gaugino code. *JHEP*, 04:006, 2007.
- [89] Shamit Kachru, Renata Kallosh, Andrei D. Linde, and Sandip P. Trivedi. De Sitter vacua in string theory. *Phys. Rev.*, D68:046005, 2003.
- [90] Luis E. Ibanez. The Fluxed MSSM. *Phys. Rev.*, D71:055005, 2005.
- [91] Luis E. Ibanez, C. Munoz, and S. Rigolin. Aspects of type I string phenomenology. *Nucl. Phys.*, B553:43–80, 1999.
- [92] Abdelhak Djouadi, Jean-Loic Kneur, and Gilbert Moultaka. SuSpect: A Fortran code for the supersymmetric and Higgs particle spectrum in the MSSM. *Comput. Phys. Commun.*, 176:426–455, 2007.
- [93] Anthony Allen Affolder et al. Search for gluinos and scalar quarks in  $p\bar{p}$  collisions at  $\sqrt{s} = 1.8$  TeV using the missing energy plus multijets signature. *Phys. Rev. Lett.*, 88:041801, 2002.
- [94] V. M. Abazov et al. Search for squarks and gluinos in events with jets and missing transverse energy using  $2.1 \text{ fb}^{-1}$  of  $p\bar{p}$  collision data at  $\sqrt{s} = 1.96$ - TeV. *Phys. Lett.*, B660:449–457, 2008.
- [95] Howard Baer, Eun-Kyung Park, Xerxes Tata, and Ting T. Wang. Collider and dark matter searches in models with mixed modulus-anomaly mediated SUSY breaking. *JHEP*, 08:041, 2006.
- [96] Howard Baer, Eun-Kyung Park, Xerxes Tata, and Ting T. Wang. Measuring Modular Weights in Mirage Unification Models at the LHC and ILC. *Phys. Lett.*, B641:447–451, 2006.
- [97] Kiwoon Choi, Kang Young Lee, Yasuhiro Shimizu, Yeong Gyun Kim, and Ken-ichi Okumura. Neutralino Dark Matter in Mirage Mediation. *JCAP*, 0612:017, 2006.
- [98] D. N. Spergel et al. Wilkinson Microwave Anisotropy Probe (WMAP) three year results: Implications for cosmology. *Astrophys. J. Suppl.*, 170:377, 2007.

- [99] Minoru Nagai and Kazunori Nakayama. Nonthermal dark matter in mirage mediation. *Phys. Rev.*, D76:123501, 2007.
- [100] Minoru Nagai and Kazunori Nakayama. Direct/indirect detection signatures of non-thermally produced dark matter. *Phys. Rev.*, D78:063540, 2008.
- [101] Graciela B. Gelmini and Paolo Gondolo. Neutralino with the right cold dark matter abundance in (almost) any supersymmetric model. *Phys. Rev.*, D74:023510, 2006.
- [102] Graciela Gelmini, Paolo Gondolo, Adrian Soldatenko, and Carlos E. Yaguna. The effect of a late decaying scalar on the neutralino relic density. *Phys. Rev.*, D74:083514, 2006.
- [103] A. B. Lahanas, N. E. Mavromatos, and Dimitri V. Nanopoulos. Smoothly evolving Supercritical-String Dark Energy relaxes Supersymmetric-Dark-Matter Constraints. *Phys. Lett.*, B649:83–90, 2007.
- [104] E. Aprile et al. The XENON Dark Matter Search Experiment. *Nucl. Phys. Proc. Suppl.*, 138:156–159, 2005.
- [105] Tripathi, M. LUX: A Large Two-Phase Liquid Xenon Detector for WIMP Search, July 2007. Talk given at SUSY2007.
- [106] Z. Ahmed et al. Search for Weakly Interacting Massive Particles with the First Five-Tower Data from the Cryogenic Dark Matter Search at the Soudan Underground Laboratory. *Phys. Rev. Lett.*, 102:011301, 2009.
- [107] D. S. Akerib et al. The SuperCDMS proposal for dark matter detection. *Nucl. Instrum. Meth.*, A559:411–413, 2006.
- [108] Aldo Morselli, Andrea Lionetto, Alessandro Cesarini, Francesco Fucito, and Piero Ullio. Search for Dark Matter with GLAST. *Nucl. Phys. Proc. Suppl.*, 113:213–220, 2002.
- [109] Lars Bergstrom, Piero Ullio, and James H. Buckley. Observability of gamma rays from dark matter neutralino annihilations in the Milky Way halo. *Astropart. Phys.*, 9:137–162, 1998.
- [110] Dan Hooper and Lian-Tao Wang. Direct and indirect detection of neutralino dark matter in selected supersymmetry breaking scenarios. *Phys. Rev.*, D69:035001, 2004.
- [111] <http://icrhp9.icrr.u-tokyo.ac.jp/index.html>.
- [112] <http://www.mpi-hd.mpg.de/hfm/HESS/HESS.html>.
- [113] <http://wwwmagic.mppmu.mpg.de/>.
- [114] <http://veritas.sao.arizona.edu/>.
- [115] M. C. Gonzalez-Garcia, F. Halzen, and M. Maltoni. Physics reach of high-energy and high-statistics Icecube atmospheric neutrino data. *Phys. Rev.*, D71:093010, 2005.

- [116] Francis Halzen and Dan Hooper. Prospects for detecting dark matter with neutrino telescopes in light of recent results from direct detection experiments. *Phys. Rev.*, D73:123507, 2006.
- [117] Vernon Barger, Wai-Yee Keung, Gabe Shaughnessy, and Adam Tregre. High energy neutrinos from neutralino annihilations in the Sun. *Phys. Rev.*, D76:095008, 2007.
- [118] R. Abbasi et al. Limits on a muon flux from neutralino annihilations in the Sun with the IceCube 22-string detector. *Phys. Rev. Lett.*, 102:201302, 2009.
- [119] S. W. Barwick et al. Cosmic ray positrons at high-energies: A New measurement. *Phys. Rev. Lett.*, 75:390–393, 1995.
- [120] S. W. Barwick et al. Measurements of the cosmic-ray positron fraction from 1- GeV to 50-GeV. *Astrophys. J.*, 482:L191–L194, 1997.
- [121] Phill Grajek, Gordon Kane, Dan Phalen, Aaron Pierce, and Scott Watson. Is the PAMELA Positron Excess Winos? *Phys. Rev.*, D79:043506, 2009.
- [122] J. Chang et al. An excess of cosmic ray electrons at energies of 300.800 GeV. *Nature*, 456:362–365, 2008.
- [123] Marco Cirelli, Mario Kadastik, Martti Raidal, and Alessandro Strumia. Model-independent implications of the  $e^+$ ,  $e^-$ , anti-proton cosmic ray spectra on properties of Dark Matter. *Nucl. Phys.*, B813:1–21, 2009.
- [124] F. Donato, D. Maurin, P. Brun, T. Delahaye, and P. Salati. Constraints on WIMP Dark Matter from the High Energy PAMELA  $\bar{p}/p$  data. *Phys. Rev. Lett.*, 102:071301, 2009.
- [125] Dan Hooper, Albert Stebbins, and Kathryn M. Zurek. Excesses in cosmic ray positron and electron spectra from a nearby clump of neutralino dark matter. *Phys. Rev.*, D79:103513, 2009.
- [126] O. Adriani et al. A new measurement of the antiproton-to-proton flux ratio up to 100 GeV in the cosmic radiation. *Phys. Rev. Lett.*, 102:051101, 2009.
- [127] David Maurin and Richard Taillet. Spatial Origin of Galactic Cosmic Rays in Diffusion Models: II- Exotic Primary Cosmic Rays. *Astron. Astrophys.*, 404:949–958, 2003.
- [128] Marco Cirelli, Roberto Franceschini, and Alessandro Strumia. Minimal Dark Matter predictions for galactic positrons, anti-protons, photons. *Nucl. Phys.*, B800:204–220, 2008.
- [129] C. J. Hailey et al. Accelerator Testing of the General Antiparticle Spectrometer, a Novel Approach to Indirect Dark Matter Detection. *JCAP*, 0601:007, 2006.
- [130] M. Kadastik, K. Kannike, A. Racioppi, and M. Raidal. Implications of the CDMS result on Dark Matter and LHC physics. 2009.

- [131] A. Bottino, F. Donato, N. Fornengo, and S. Scopel. Relic neutralinos and the two dark matter candidate events of the CDMS II experiment. 2009.
- [132] Daniel Feldman, Zuowei Liu, and Pran Nath. Connecting the Direct Detection of Dark Matter with Observation of Sparticles at the LHC. 2009.
- [133] Masahiro Ibe and Tsutomu T. Yanagida. Neutralino Dark Matter in Gauge Mediation in Light of CDMS-II. 2009.
- [134] Michael Holmes and Brent D. Nelson. Non-Universal Gaugino Masses, CDMS, and the LHC. 2009.
- [135] John R. Ellis, Keith A. Olive, Yudi Santoso, and Vassilis C. Spanos. Update on the direct detection of supersymmetric dark matter. *Phys. Rev.*, D71:095007, 2005.
- [136] John R. Ellis, Jonathan L. Feng, Andrew Ferstl, Konstantin T. Matchev, and Keith A. Olive. Prospects for detecting supersymmetric dark matter at post-LEP benchmark points. *Eur. Phys. J.*, C24:311–322, 2002.
- [137] Andreas Birkedal-Hansen and Brent D. Nelson. Relic neutralino densities and detection rates with nonuniversal gaugino masses. *Phys. Rev.*, D67:095006, 2003.
- [138] Utpal Chattopadhyay and D. P. Roy. Higgsino dark matter in a SUGRA model with nonuniversal gaugino masses. *Phys. Rev.*, D68:033010, 2003.
- [139] Howard Baer, Azar Mustafayev, Eun-Kyung Park, Stefano Profumo, and Xerxes Tata. Mixed higgsino dark matter from a reduced SU(3) gaugino mass: Consequences for dark matter and collider searches. *JHEP*, 04:041, 2006.
- [140] Howard Baer, Azar Mustafayev, Heaya Summy, and Xerxes Tata. Mixed Higgsino Dark Matter from a Large SU(2) Gaugino Mass. *JHEP*, 10:088, 2007.
- [141] Kyu Jung Bae, Radovan Dermisek, Hyung Do Kim, and Ian-Woo Kim. Mixed Bino-Wino-Higgsino Dark Matter in Gauge Messenger Models. *JCAP*, 0708:014, 2007.
- [142] Utpal Chattopadhyay, Debottam Das, and D. P. Roy. Mixed Neutralino Dark Matter in Nonuniversal Gaugino Mass Models. *Phys. Rev.*, D79:095013, 2009.
- [143] A. Brignole, Luis E. Ibanez, and C. Munoz. Towards a theory of soft terms for the supersymmetric Standard Model. *Nucl. Phys.*, B422:125–171, 1994.
- [144] Achille Corsetti and Pran Nath. Gaugino Mass Nonuniversality and Dark Matter in SUGRA, Strings and D Brane Models. *Phys. Rev.*, D64:125010, 2001.
- [145] Andreas Birkedal-Hansen and Brent D. Nelson. The role of Wino content in neutralino dark matter. *Phys. Rev.*, D64:015008, 2001.
- [146] Gordon L. Kane and S. F. King. Naturalness implications of LEP results. *Phys. Lett.*, B451:113–122, 1999.

- [147] G. L. Kane, Joseph D. Lykken, Brent D. Nelson, and Lian-Tao Wang. Re-examination of electroweak symmetry breaking in supersymmetry and implications for light superpartners. *Phys. Lett.*, B551:146–160, 2003.
- [148] D. Horton and G. G. Ross. Naturalness and Focus Points with Non-Universal Gaugino Masses. *Nucl. Phys.*, B830:221–247, 2010.
- [149] Shehu S. AbdusSalam, Benjamin C. Allanach, Fernando Quevedo, Farhan Feroz, and Mike Hobson. Fitting the Phenomenological MSSM. 2009.
- [150] E. Barberio et al. Averages of  $b$ -hadron and  $c$ -hadron Properties at the End of 2007. 2008.
- [151] Abdelhak Djouadi, Manuel Drees, and Jean-Loic Kneur. Updated constraints on the minimal supergravity model. *JHEP*, 03:033, 2006.
- [152] T. Aaltonen et al. Search for  $B_s^0 \rightarrow \mu^+\mu^-$  and  $B_d^0 \rightarrow \mu^+\mu^-$  decays with  $2fb^{-1}$  of  $p\bar{p}$  collisions. *Phys. Rev. Lett.*, 100:101802, 2008.
- [153] D. Toussaint and W. Freeman. The strange quark condensate in the nucleon in 2+1 flavor QCD. *Phys. Rev. Lett.*, 103:122002, 2009.
- [154] Lars Bergstrom and Piero Ullio. Full one-loop calculation of neutralino annihilation into two photons. *Nucl. Phys.*, B504:27–44, 1997.
- [155] Zvi Bern, Paolo Gondolo, and Maxim Perelstein. Neutralino annihilation into two photons. *Phys. Lett.*, B411:86–96, 1997.
- [156] Piero Ullio and Lars Bergstrom. Neutralino annihilation into a photon and a Z boson. *Phys. Rev.*, D57:1962–1971, 1998.
- [157] Piero Ullio. Indirect detection of neutralino dark matter candidates in anomaly-mediated supersymmetry breaking scenarios. *JHEP*, 06:053, 2001.
- [158] Torbjorn Sjostrand, Stephen Mrenna, and Peter Z. Skands. PYTHIA 6.4 Physics and Manual. *JHEP*, 05:026, 2006.
- [159] John Conway. Pgs 4. <http://www.physics.ucdavis.edu/~conway/research/software/pgs/pgs4-general.htm>.
- [160] A. Djouadi, M. M. Muhlleitner, and M. Spira. Decays of Supersymmetric Particles: the program SUSY-HIT (SUSpect-SdecaY-Hdecay-InTerface). *Acta Phys. Polon.*, B38:635–644, 2007.
- [161] G. L. Bayatian et al. CMS technical design report, volume II: Physics performance. *J. Phys.*, G34:995–1579, 2007.
- [162] Howard Baer, Chih-hao Chen, Frank Paige, and Xerxes Tata. Signals for minimal supergravity at the CERN large hadron collider: Multi - jet plus missing energy channel. *Phys. Rev.*, D52:2746–2759, 1995.

- [163] Howard Baer, Chih-hao Chen, Frank Paige, and Xerxes Tata. Signals for Minimal Supergravity at the CERN Large Hadron Collider II: Multilepton Channels. *Phys. Rev.*, D53:6241–6264, 1996.
- [164] Baris Altunkaynak, Phillip Grajek, Michael Holmes, Gordon Kane, and Brent D. Nelson. Studying Gaugino Mass Unification at the LHC. *JHEP*, 04:114, 2009.
- [165] Mariana Grana. Flux compactifications in string theory: A comprehensive review. *Phys. Rept.*, 423:91–158, 2006.
- [166] Mary K. Gaillard and Brent D. Nelson. Kaehler stabilized, modular invariant heterotic string models. *Int. J. Mod. Phys.*, A22:1451, 2007.
- [167] Emanuel Katz, Yael Shadmi, and Yuri Shirman. Heavy thresholds, slepton masses and the mu term in anomaly mediated supersymmetry breaking. *JHEP*, 08:015, 1999.
- [168] Riccardo Rattazzi, Alessandro Strumia, and James D. Wells. Phenomenology of deflected anomaly mediation. *Nucl. Phys.*, B576:3–28, 2000.
- [169] Mary K. Gaillard, Brent D. Nelson, and Yi-Yen Wu. Gaugino masses in modular invariant supergravity. *Phys. Lett.*, B459:549–556, 1999.
- [170] Jonathan A. Bagger, Takeo Moroi, and Erich Poppitz. Anomaly mediation in supergravity theories. *JHEP*, 04:009, 2000.
- [171] Pierre Binetruiy, Mary K. Gaillard, and Yi-Yen Wu. Dilaton Stabilization in the Context of Dynamical Supersymmetry Breaking through Gaugino Condensation. *Nucl. Phys.*, B481:109–128, 1996.
- [172] Pierre Binetruiy, Mary K. Gaillard, and Yi-Yen Wu. Modular invariant formulation of multi-gaugino and matter condensation. *Nucl. Phys.*, B493:27–55, 1997.
- [173] G. L. Kane et al. Theory-motivated benchmark models and superpartners at the Tevatron. *Phys. Rev.*, D67:045008, 2003.
- [174] <http://v1.jthaler.net/olympicswiki/doku.php>.
- [175] Nima Arkani-Hamed, Gordon L. Kane, Jesse Thaler, and Lian-Tao Wang. Supersymmetry and the LHC inverse problem. *JHEP*, 08:070, 2006.
- [176] Carola F. Berger, James S. Gainer, JoAnne L. Hewett, Ben Lillie, and Thomas G. Rizzo. General Features of Supersymmetric Signals at the ILC: Solving the LHC Inverse Problem. *Phys. Rev.*, D80:095018, 2009.
- [177] C. F. Berger, J. S. Gainer, J. L. Hewett, T. G. Rizzo, and B. Lillie. The LHC Inverse Problem, Supersymmetry, and the ILC. *Phys. Lett.*, B677:48–53, 2009.
- [178] Baris Altunkaynak, Michael Holmes, and Brent D. Nelson. Solving the LHC Inverse Problem with Dark Matter Observations. *JHEP*, 10:013, 2008.

- [179] G. J. Alner et al. First limits on WIMP nuclear recoil signals in ZEPLIN-II: A two phase xenon detector for dark matter detection. *Astropart. Phys.*, 28:287–302, 2007.
- [180] Veronique Sanglard et al. Final results of the EDELWEISS-I dark matter search with cryogenic heat-and-ionization Ge detectors. *Phys. Rev.*, D71:122002, 2005.
- [181] Henrique M. Araujo et al. The ZEPLIN-III dark matter detector: Performance study using an end-to-end simulation tool. *Astropart. Phys.*, 26:140–153, 2006.
- [182] <http://dmttools.berkeley.edu/limitplots/>.
- [183] Andrew W. Strong, Igor V. Moskalenko, and Vladimir S. Ptuskin. Cosmic-ray propagation and interactions in the Galaxy. *Ann. Rev. Nucl. Part. Sci.*, 57:285–327, 2007.
- [184] Gabrijela Zaharijas and Dan Hooper. Challenges in detecting gamma-rays from dark matter annihilations in the galactic center. *Phys. Rev.*, D73:103501, 2006.
- [185] Edward A. Baltz, James E. Taylor, and Lawrence L. Wai. Can Astrophysical Gamma Ray Sources Mimic Dark Matter Annihilation in Galactic Satellites? *Astrophys. J. Lett.*, 659:L125–L128, 2007.
- [186] Leszek Roszkowski, Roberto Ruiz de Austri, Joe Silk, and Roberto Trotta. On prospects for dark matter indirect detection in the Constrained MSSM. *Phys. Lett.*, B671:10–14, 2009.
- [187] H. A. Mayer-Hasselwander et al. High-energy gamma ray emission from the galactic center. *Astron. Astrophys.*, 335:161–172, 1998.
- [188] F. Aharonian et al. Very high energy gamma rays from the direction of Sagittarius A\*. *Astron. Astrophys.*, 425:L13–L17, 2004.
- [189] K. Kosack et al. TeV Gamma-Ray Observations of the Galactic Center. *Astrophys. J.*, 608:L97–L100, 2004.
- [190] Ken’ichi Tsuchiya et al. Detection of sub-TeV gamma-rays from the galactic center direction by CANGAROO-II. *Astrophys. J.*, 606:L115–L118, 2004.
- [191] J. Albert et al. Observation of Gamma Rays from the Galactic Center with the MAGIC Telescope. *Astrophys. J.*, 638:L101–L104, 2006.
- [192] Dan Hooper and Brenda L. Dingus. Limits on supersymmetric dark matter from EGRET observations of the galactic center region. *Phys. Rev.*, D70:113007, 2004.
- [193] Felix Aharonian and Andrii Neronov. High energy gamma rays from the massive black hole in the galactic center. *Astrophys. J.*, 619:306–313, 2005.
- [194] Scott Dodelson, Dan Hooper, and Pasquale D. Serpico. Extracting the Gamma Ray Signal from Dark Matter Annihilation in the Galactic Center Region. *Phys. Rev.*, D77:063512, 2008.